United Arab Emirates University
Scholarworks@UAEU

Theses | Electronic Theses and Dissertations

2004

Preparation and characterization of thermally stabilized Ceria and Ceria containing materials

Leena Ali Rashid Al-Kaabi

Follow this and additional works at: https://scholarworks.uaeu.ac.ae/all_theses

Part of the Materials Science and Engineering Commons

Recommended Citation

Al-Kaabi, Leena Ali Rashid, "Preparation and characterization of thermally stabilized Ceria and Ceria containing materials" (2004). *Theses*. 357.
https://scholarworks.uaeu.ac.ae/all_theses/357

This Thesis is brought to you for free and open access by the Electronic Theses and Dissertations at Scholarworks@UAEU. It has been accepted for inclusion in Theses by an authorized administrator of Scholarworks@UAEU. For more information, please contact fadl.musa@uaeu.ac.ae.

United Arab Emirates University
Deanship of Graduate Studies
M.Sc. Program in Material Sciences and Engineering

"Preparation and Characterization of Thermally Stabilized Ceria and Ceria Containing Materials"

By

Leena Ali Rashid Al-Kaabi

A thesis
Submitted to
United Arab Emirates University
In partial fulfillment of the requirements
For the Degree of M.Sc. in Material Sciences and Engineering

Supervisors

Kamal.M.S.Khalil
Assistant Professor
Department of Chemistry
Faculty of Science
UAEU

Brian Murphy
Assistant Professor
Department of Chemistry
Faculty of Science
UAEU

2004

United Arab Emirates University

Deanship of Graduate Studies

M.Sc. Program in Material Sciences and Engineering

CERTIFICATE OF APPROVAL

M.Sc. THESIS

This is to certify that the M.Sc. thesis of

Leena Ali Rashid Al-Kaabi

Has been approved by the Examining Committee for the thesis requirement for the Degree of M.Sc. in Material Sciences and Engineering

In the 1st semester 2004 graduation.

Thesis Committee:	Date	Signature
1-		
2-		
3-		
Dean of Graduate Studies		

UAEU Library

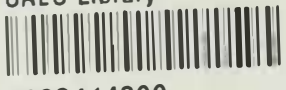

1000414099

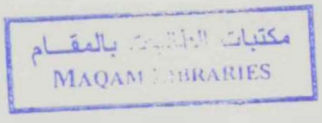

Dedication

.

.

.

.

.

.

To the one who loved his dream and believed in it bringing reality into submission to him…

.

.

.

.

.

.

Our precious father … Zayed

Acknowledgments

Thank Allah Who granted me success and gave me the energy and patience to accomplish this task, thanks be unto Allah always and forever.

To begin with, I offer my deepest gratitude to Dr. Kamal. M. S. Khalil, my graduate supervisor who did not spare any effort in giving me all the knowledge or help I needed and was a model to follow in faithfulness and creativity. I would like to thank Dr. Brian Murphy for his help and effort in bringing this thesis to completion.

My deep thank to the United Arab Emirates University, Deanship of Graduate Studies and Dr.Ahmed Al-Shamsi the Chairman of the Chemistry Department. Also, I want to thank everyone in the Department of Chemistry, those who offered help or encouraging words especially Dr. Rashed Al Saeed and Dr. Mohamed Khattab. My gratitude goes to all my instructors during both the Bachelors and Masters phases wherever they may be.

In addition, I offer my deep gratitude to Mr. Jamal, Mr. Esam and Dr. Rao at the Central Laboratories Unit and Dr. Ayman (Geology), Mr. Omar Al Basheer (Geology) and Mr. Burhan (Chemistry).

All my affection and gratitude to my beloved parents, who encouraged me from my youth to seek, know and learn more.

My dear sister Sheikha, you were always beside me and remain not withholding from me time or effort, I ask Allah to preserve you and make you joyful always.

Aisha Al-Nayli, the companion of my way and dreams, my friend in all circumstances and phases that brought us closer... My dear we grew and our dreams and ambitions grew with us... To you belongs my sincerest love.

Nadya Al-Kalbani I remember very well that day when you and I were dreaming and decided to fulfill the dream and transform it to reality, now the dream is almost reality. My dear... My prayers for you are for eternal success.

Zahra Al-Badi, I will not forget the lovely times when you refused to leave me by myself in the laboratory; my deepest gratitude.

Moza Al Zuabi my dear... All gratitude

Gratitude still has posterity for there are friends who give you without expecting anything in return and accept you as you are in your sanity and insanity... Maryam Al-Kayoumi and Sheikha Al-Neyadi, I am at a loss for words to thank you.

Lovingly,

Leena

Abstract

Ceria, CeO_2, is one of the most important catalytic materials that can play multiple roles owing to its ability to release and uptake oxygen under catalytic reaction conditions with the preservation of its fluorite structure. Textural and thermal stability is a critical issue in determining the promoting and metal supporting functions of CeO_2 in its catalytic applications in the three way catalysis. Therefore, significant efforts have been made by industry on finding ways to improve the thermal stability of ceria both by modification of the synthesis of CeO_2 and by looking at possible stabilizers.

In the first part, of this work thermally stable ceria aggregates were obtained via a two-step sol gel process of cerium isopropoxide dispersed in isopropanol by ultrasonic radiation. The first step involved a hydrolysis reaction. In the second step, the resultant dispersions were mixed under stirring with neutral or basic water isopropanol solutions. The ceria powders obtained via neutral and basic media were shown to be composed of aggregates of fine particles. However, it was found that the type of media affected both particle texture and morphology. Specific surface areas of 33.1 and 44.2 m^2g^{-1} respectively, were obtained for the neutral and basic materials, which calcined at 650°C for 3 h. Moreover, the oxidative nature of ceria was found to help in the removal of the organic impurities while the hydroxylated surface of ceria facilitated the formation of thermally stable agglomerates.

In the second part of this work, Ceria supported on silica, ceria/silica, materials of 10 and 20% (w/w) were prepared by calcinations, at 650°C for 3 h, of the xerogels obtained by the mixing of the corresponding amount of a ceria precursor with freshly prepared sols of spherical silica particles (Stober particles) in their mother liquors. Two different ceria precursors were examined in this investigation. The first was a gel produced by prehydrolysis of cerium(IV)-tetra isopropoxide in isopropanol media, and

the second was an aqueous solution of ceric(IV) ammoniumnitrate. Different textural and morphological characteristics that developed by calcination, were investigated by TGA, FTIR, XRD, SEM and analyses of N_2 adsorption isotherms. The results indicated better ceria dispersion and formation of mesoporous textural composites materials produced by the second precursor, ceric(IV) ammonium nitrate, than the first precursor, prehydrolysed cerium(IV)-tetraisopropoxide.

The results show that properties of composite materials are largely related to the preparation method and the precursor type. Moreover, mixing media affect both nucleation and the growth of ceria particles and their protection against sintering upon calcinations at the test temperature.

TABLE OF CONTENTS

LISTS OF TABLES

CHAPTER 1:-

CHAPTER 3:-

CHAPTER 4

LIST OF FIGURES

CHAPTER 1:-

CHAPTER 2.

CHAPTER 3:-

CHAPTER 4:-

1.2.2. The higher oxides of cerium ($CeO_{1.714}$-CeO_2): -

Ceria can be reduced by removing O^{2-} ions from the CeO_2 lattice, which generates an anion vacant site according to the following equation:

$$4Ce^{4+} + O^{2-} \rightarrow 4Ce^{4+} + 2e^- / \square + 0.5O_2 \rightarrow 2Ce^{4+} + 2Ce^{3+} + \square + 0.5O_2 \qquad \text{Eq(1.1)}$$

where $\square$ represents an anion vacant site which originated from the removal of O^{2-} from the lattice, which in this case corresponds to an oxygen tetrahedral site (Ce_4O). By the reduction of two cerium cations from the +4 oxidation state to the +3 oxidation state the overall electrostatic balance is maintained. CeO_2 is reduced at elevated temperatures and low oxygen pressures to form a seeming continuum of oxygen deficient non-stoichiometric oxides, which on cooling form into highly ordered fluorite-related superstructures, often with complex stoichiometries. It has been found in the literature that this continuum exists above 685°C in a range of CeO_x composition from $1.714 < x < 2$[7,21,22]. This is termed the α-phase, which is a disordered non-stoichiometric fluorite related phase which is meta stable at high temperatures. The high temperature X-ray diffraction pattern of this phase does not show superstructures and the lattice parameter a of the cubic phase has been shown to increase as x decreases[23,24].

At lower temperature, the α-phase itself can transform through a disorder-order process generating into a series of ordered, fluorite related phases. These phases have the general formula Ce_nO_{2n-2m}. Such mixed valent compounds have compositions ranging between $CeO_{1.714}$ (Ce_7O_{12}, $n = 7$, $m = 1$) and CeO_2. The variation of x at low temperature can be attributed to the co-existence of two phases with different stoichiometries (n, n+1). In comparison, pure Ce_nO_{2n-2m}, exists only in a much narrower range with the dominant phases between CeO_2 and $CeO_{1.714}$, as shown is Table 1.1. However, there are many anion deficient structures whose exact structures remain unexplained. This is due to two main factors:

(i) it is very difficult to obtain single crystals suitable for X-ray diffraction for some of the oxides.

(ii) powder XRD techniques are limited due to the somewhat poor X-ray scattering factor of oxygen, which means that the details of the oxygen sublattice structure may be inaccessible. Both problems may be overcome in principle by the use of the structural technique of neutron diffraction.

For this reason, the exact nature of the oxygen sublattice structure continues to be a problem. In neutron diffraction, the coherent neutron scattering amplitudes of cerium and oxygen are similar. In addition, the profile refinement technique has enabled the structural refinement of the powder diffraction profiles [25,26].

1.2.3. The phase diagram of the Ce-O system:-

The phase diagram of Ce-O_x, shows all the phases of the Ce-O system, with respect to temperature, Figure 1.2. At least three CeO_x phases in the region of the higher oxide are observed[7,22,25] :

(i) the β-phase with composition in the range $1.805 < x < 1.812$.

(ii) the γ-phase with composition in the range $1.775 < x < 1.785$.

(iii) the δ-phase with composition in the range $1.710 < x < 1.720$.

In addition Ce_7O_{12}, Ce_9O_{16}, $Ce_{10}O_{18}$, $Ce_{11}O_{20}$ composition phases have been reported in the literature and the crystal structure of Ce_7O_{12} has been determined [25,28]. The latter structure is basically a rhombohedral distortion of the fluorite lattice caused by ordering of oxygen vacancies along one direction. The phase diagram for $CeO_{1.714}$-$CeO_{1.5}$ is dominated at high temperature by the presence of the δ-phase. This is an non-stoichiometric ($Ce_2O_{3+\delta}$) phase which has a body centered cubic type C rare-earth oxide structure. A small (σ-α) miscibility separation between the σ and α phases is observed.

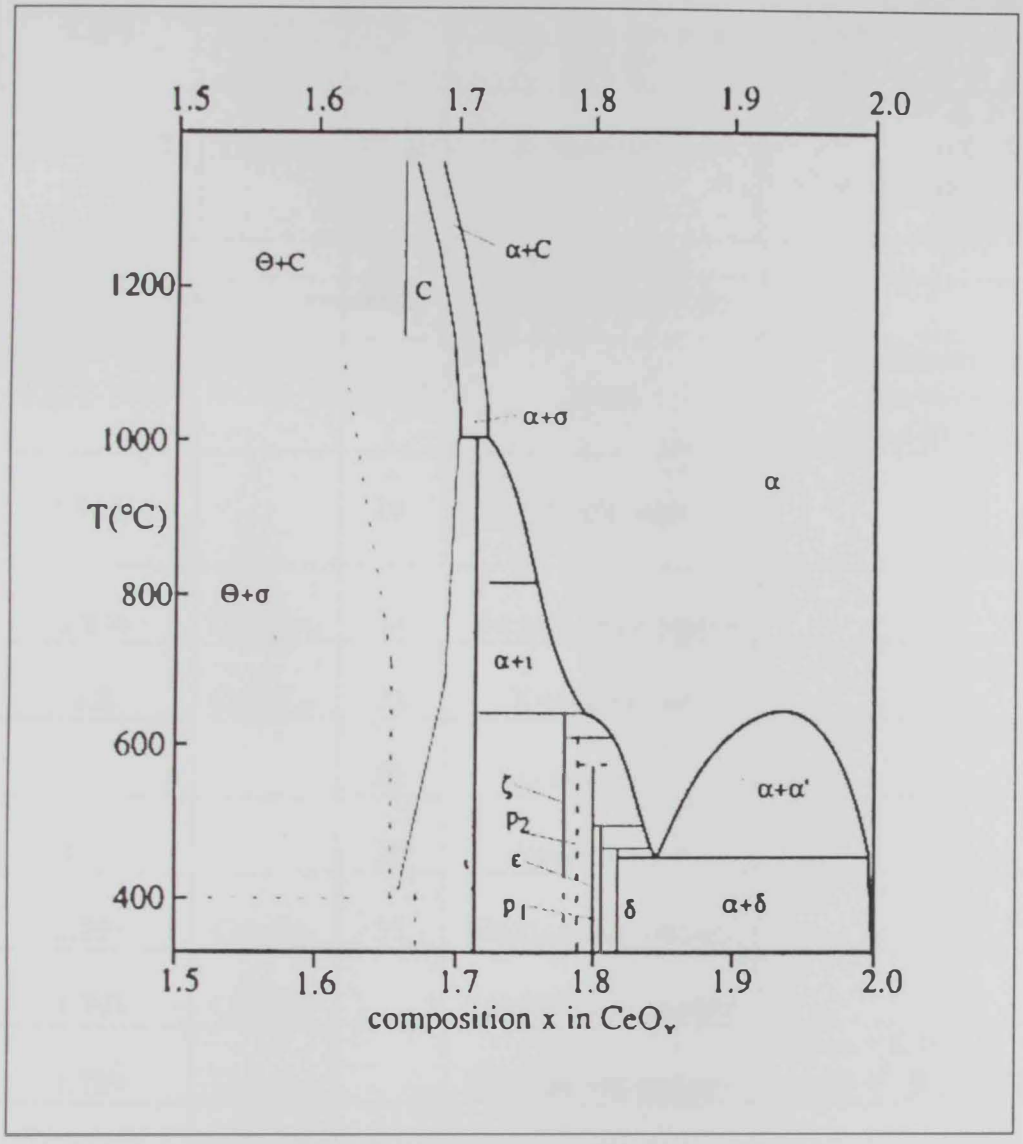

Figure 1.2 Phase diagram of CeO_2[7,29,30,31].

Table 1.1 Some components of the CeO_{2-x} phases

Phase	X in CeO_x	Comp.[a]	Ref	Source	Notes
B	1.833	Ce_6O_{11}	9	Xray diffraction at 855°C	Space group $P2_1/n$ a = 6.781 Å , b = 11.893 Å , c = 15.823 Å , β = 125.04°
Δ	1.817-1.818	$Ce_{11}O_{20}$	25,26	X-ray/neutron	a = 6.757 Å, b = 10.260 Å , c = 6.732 Å, α = 90.04° , β = 99.80°, γ = 96.22°
			29	Specific heat	
			33,35	Electron microscopy	
(β)[b]	1.812-1805		23,27	X-ray	Rhombohedral cell, (pseudohexagonal) a = 3.810 Å, c = 9.538 Å
	1.808		29	Specific heat	
δ`	1.806	$Ce_{62}O_{112}$	34	Eectron microscopy	
E	1.8	$Ce_{10}O_{18}$	25	X-ray/neutron	
			29	Specific heat	
P_2	1.79		29	Specific heat	
M39	1.795	$Ce_{39}O_{70}$	35	Electron microscopy	
M29	1.793	$Ce_{29}O_{52}$		Electron microscopy	
	1.789	$Ce_{19}O_{34}$		Electron microscopy	$a = c$ = 6.750 Å , b = 8.400 Å α = 99.4° β = 99.21°° γ = 75.00°
M13	1.769	$Ce_{13}O_{23}$		Electron microscopy	
(γ)ξ	1.775-1.785	Ce_9O_{16}	27	X-ray	Rhombohedral cell (pseudohexagonal) a = 3.910 Å
			25	X-ray/ neutron	
(δ)t	1.714	Ce_9O_{16}	26,28	X-ray/neutron	Rhombohedral cell (pseudohexagonal) a = 6.785 Å, α = 99.42°
			29	Specific heat	
			34	Electron microscopy	
	1.72-1.710		27	X-ray	Rhombohedral cell (pseudohexagonal) a = 3.912 Å , c = 9.657 Å

1.3. Defect structure in cerium oxide:-

Intrinsic defects may be present because of thermal disorder or can be created by the reaction between the solid and the surrounding atmosphere. Extrinsic defects are formed by impurities or by the introduction of aliovalent dopants. Defects in ceria can be intrinsic or extrinsic. There are three possible thermally generated intrinsic disorder reactions in ceria that do not involve exchange with the gas phase. These defects are of the Schottky Eq(1.2) and Frankel Eq(1.3), Eq(1.4) types[36].

-Schottky defect: when an atom leaves its original site and migrates to the surface of the crystal;

-Frankel defect: when an atom transfers from an original lattice site and resides at an interstitial position, a position not normally occupied by the atom.

These types of defect can be represented using the Kroger - Vink defect notation:

$$Ce_{Ce} + 2\,O_o \leftrightarrow V''''_{Ce} + 2\,V_{\ddot{o}} + CeO_2 \qquad \Delta E = 3.53 \text{ eV} \quad \text{Eq(1.2)}$$

$$Ce_{Ce} \leftrightarrow Ce_i^{\cdot\cdot\cdot\cdot} + V''''_{Ce} \qquad \Delta E = 11.11 \text{ eV} \quad \text{Eq(1.3)}$$

$$O_o \leftrightarrow O_i'' + V_{\ddot{o}} \qquad \Delta E = 3.2 \text{ eV} \quad \text{Eq(1.4)}$$

These lead to the formation of pairs of oxygen vacancies and oxygen interstitial positions. In the case of exposure to a reducing gaseous atmosphere, this leads to a high concentration of such defects. Upon reduction, ceria has an excess of metal compared to its anion content; its cation/anion ratio is greater than 0.5. There are two principle ways to accommodate this variation in composition. In the first case, oxygen vacancies are assumed to compensate the holes formed on reduction of Ce^{4+} to Ce^{3+}. When oxygen is removed, the crystal will end up with an overall positive charge and two electrons for each oxygen ion moved are needed to be introduced in order to keep the crystal neutral.

These electrons are associated with two cerium atoms that will change the charge from +4 to +3. The effective charge of the anion vacancies is positive, thus they effectively neutralize the negatively charged holes. The process illustrated in Figure 1.3 a is generally represented as:

$$CeO_2 \rightarrow CeO_{2-x} + x/2O_{2(g)} \qquad (x < 0.5) \qquad \text{Eq(1.5)}$$

Or the following defect reaction can be written:

$$CeO_2 \leftrightarrow 2xCe'_{Ce} + (1-2x)Ce_{ce} + xV_{\ddot{o}} + (2-x)O_o + 0.5xO_{2(g)} \qquad \text{Eq(1.6)}$$

The reaction implies that as x moles of atomic oxygen are removed from the lattice, the corresponding quantity of O^{-2} sites are occupied by the oxygen vacancies, leaving $2-x$ moles of O^{-2} anions in their original positions. On the cation side, $2x$ moles of Ce^{3+} are formed (Ce'_{ce}), leaving $1-2x$ moles of Ce^{+4}. Cation interstitials provide an alternative way to create positively charged defects. These interstitial may be formed by transfer of cerium cations located on the surface to an interstitials position and by the removal of two anions to the gas phase for each cerium interstitial formed[37]. The process can be represented simply in the following equation:

$$(1+x)\,CeO_2 \leftrightarrow Ce_{(1+x)}\,O_2 + xO_{2(g)} \qquad (x < 0.33) \qquad \text{Eq(1.7)}$$

which does not however show where the electrons are localized. Several possibilities exist and these are highlighted more satisfactory in the following defect reactions which

show the formation of either triply, $Ce_i^{\cdots}$ (Eq 1.8), or quadruply, $Ce^{\cdots\cdot}$ (Eq 1.9), ionized cerium interstitials:

$$(1+x)\,CeO_2 \leftrightarrow x\,Ce_i^{\cdots} + 3x\,Ce'_{Ce} + (1-3x)Ce_{Ce} + 2O_o + xO_{2(g)} \quad \text{Eq(1.8)}$$

$$(1+x)\,CeO_2 \leftrightarrow x\,Ce_i^{\cdots\cdot} + 4x\,Ce'_{Ce} + (1-4x)Ce_{Ce} + 2O_o + xO_{2(g)} \quad \text{Eq(1.9)}$$

This situation is illustrated in Figure 1.3 b, where one cerium(IV) cation is present in an interstitial position with four neighbouring Ce^{3+} ions. Identification of the nature of the defects in CeO_2 is a goal that has eluded researchers for several years. The dependence of conductivity data on oxygen pressure was interpreted using models that involved both oxygen vacancies[37] and cerium interstitials[38] as predominant defects.

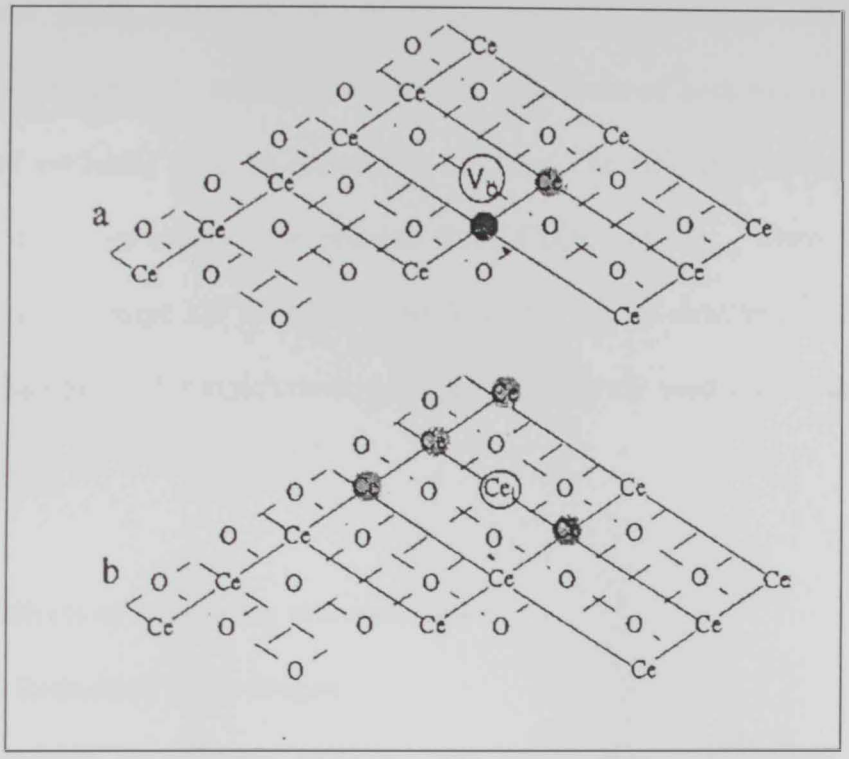

Figure 1.3 The schematic representation of a) an oxygen vacancy (V_o) and b) quadruply ionized cerium interstitial (Ce_i) in an idealized reduced CeO_2 surface. The Ce^{3+} cations are shaded.

1.4. Textural and thermal stability of ceria materials:-

It is clear, that the main role of ceria in its catalytic applications is to provide an oxygen buffering capacity. In automotive catalysis, conditions of both rich or poor air/fuel ratio are used cyclically so as to collect CO and No_x. The efficiency of ceria in this regard is superb due to its ability to be reduced from, CeO_2, to CeO_{2-x}, where $0 < x < 0.25$ upon heating in the range $327 > T > 873°C$, while preserving its structure[39]. However, in fact a small fraction of this stoichiometry range is effectively used during the actual operation of the catalysts, $0 < x < 0.02$ [40].

1.4.1. Effects of a reducing atmosphere:-

1.4.1.1. Reduction by hydrogen:-

The reduction of ceria by hydrogen has been extensively investigated by several authors[41,42-46], and recently reviews [39,40,47] by Rocchini *et al* [40], have summarized the principle findings of many such studies. Some of these principle findings are as follows:

(i) ceria is reduced by hydrogen at temperatures higher than 327°C and reduction is strongly affected by texture;

(ii) irreversible and reversible reduction occur depending on several variables such as pretreatments, precursor salts, presence of noble metals, *etc*;

(iii) the presence of noble metals dramatically enhance the redox behavior;

(iv) the incorporation of transition-metal elements, especially Zr metal, into the CeO_2 lattice influence the reduction under hydrogen by promoting the reduction of the bulk at a lower temperature;

(v) the effect of preparation methods, pretreatments and even metal precursors (nitrates, chlorides, *etc.*) can strongly modify the redox behavior.

These findings show how the reduction process and its reversibility can be affected by structural and textural considerations as well as the type of precursor. Reduction also affects the texture of ceria as discussed by Perrichon *et al.* [48]; in a reducing atmosphere involving hydrogen, the surface area drops strongly between 397 and 597°C. The BET area is only 14 m^2g^{-1} at this temperature. The microporous volume decreases from 397°C and no microporosity is detected for $T > 597$°C. Two processes are successively involved as discussed by Bernal *et al.*[46] :-

(i) a dissociative chemisorption of hydrogen;

(ii) a process leading to the creation of oxygen vacancies.

The first process can be seen at room temperature once the metal is present on the surface of the ceria[49,50]. Since the reduction process is partially reversible, for bare ceria, the chemisorption process is activated. At room temperature, no Ce^{3+} forms and the reduction is observed only above 197°C, *i.e.* at a temperature where water is desorbed. For the second process, the formation of oxygen vacancies, it has been shown that for temperatures between 347-397°C, the elimination of the oxygen ions is limited to the surface layer; however, for higher temperatures, the reduction is observed in the bulk[45].

Thus, for hydrogen, the elimination of the lattice oxygen ions occurs at $T > 397$°C. These vacancies generated by the reduction favor the disorganization of the lattice through a higher mobility of the ionic species and hence accelerate the sintering of the solid. This model, the migration of oxygen vacancies, has precisely been suggested for ceria[51]. However, for the non-reducing gas, much higher temperatures and a very low oxygen pressure are needed in order to decompose CeO_2 partially and therefore generate oxygen vacancies[7,52]. This therefore would explain the higher resistance to sintering in such circumstances.

1.4.1.2. Reduction by carbon monoxide:-

According to Perrichon *et al* [48], for carbon monoxide the surface area drops strongly between 627 and 727°C. The BET surface area is only 10 m^2/g at 827°C. The microporous volume decreases from 547°C and no microporosity is detected for $T >$ 847°C. At 397°C, the percentage reduction under carbon monoxide is similar to that obtained with hydrogen, *i.e.* the reduction remains limited to the surface[48], whereas bulk reduction was found to be more difficult and needs higher temperatures[53]. This can explained by the formation of polydentate carbonate species which can prevent the elimination of the lattice oxygen. The higher stability compared to hydroxyls is due to the basic nature of ceria. Therefore, if these carbonates are not desorbed, the bulk reduction is inhibited because the elimination process of the reduction product does not occur, since the thermal stability under carbon monoxide is higher than hydrogen. The loss of surface area occurs at 597-697°C just at the temperature where the carbonate species could be eliminated. So, it can be inferred that the carbonate ions present in CeO_2 have a stabilizing role on the texture[48].

1.4.2. Effects of doping or mixing with other oxide phases:-

As a support, ceria can be considered as poorly thermostable[41,54-57], *e.g.* at a calcination temperature of 850°C for dispersed ceria (treated initially at a temperature of 400°C with a SA = 115 m^2/g), the surface area of the sample, S_{BET}, is very low with a value of 5 m^2/g [41]. This can be correlated to changes in the pore structure, as well as crystallite growth. The latter can be thought of as pre-sintering, followed by sintering itself between the crystallites[58]. These changes are typical for the majority of oxides. As stated previously in section 1.2, anionic vacancies play a key role in both transport properties and sintering [51, 58, 59]. Under a reducing atmosphere, thermally treated ceria can generate

intrinsic defects (anionic vacancies). These vacancies do not effect or decrease the textural stability of ceria [60,61].

The doping of ceria with metal oxides, M_xO_y, where M < IV valent cations, has little effect on the thermal stability of the material since the fluorite lattice structure is conserved, but does modify the amount and ordering of the oxygen vacancies that are created by dissolving the low-valent cation in the lattice [62]. However, lattice parameters may be changed if the dopant cation radius is different from that of Ce^{4+}. The formation of solid solutions, and or new compounds have been reported in the literature[62].

Matsumoto and co-workers [63] were the first to report the effect of modification of CeO_2 with a small amount of other oxides. They found that addition of La or Zr was very effective in inhibiting the sintering of CeO_2. In particular, the formation of Ce-Zr mixed oxides was found to be very effective in the inhibition of sintering.

Recently, the reaction of cerium salts of cationic surfactant were reported in the literature as a new synthesis of mesoporous high surface area ceria[64-67]. The cationic surfactant incorporates into the hydrous oxide and lowers the surface tension of the obtained ceria and ceria-zirconia enhanced textual and thermal resistance features. After calcination at 900°C, the surface areas of CeO_2 and $Ce_{0.8}Zr_{0.2}O_2$ were found to be 40 and 56 m^2/g, respectively [68].

1.4.2.1. Ceria/silica and ceria/alumina:-

It has been reported through many patents that with the addition of silica, aluminum or zirconium cations, there is a significant improvement in the overall stability of the surface area of ceria at high temperatures [69]. Interestingly, detailed studies on the exact behavior of ceria at such high temperatures are not common in the literature, nor has the role of dopants on its structural stability been reported widely [51]. When ceria is supported or

mixed with alumina, it is thought to resist extensive sintering, which takes places as a result of the high temperatures in the monolith converter.

Cerium oxide has been used as a textural and structural promoter for supported metal or metal oxide catalyst or as a catalyst. The structural promotion effect was explained by the capability of cerium to form crystalline oxides with lattice defects which may act as catalytic active sites[70]. In addition, the texture promotion effect result from the high thermal and mechanical resistance which CeO_2 confers to catalysts. For these reasons, ceria and ceria promoted Al_2O_3 or SiO_2 are an important component in solid oxide fuel cell applications, automotive, emission control (oxidation) catalysts and CO oxidation [70,71].

Industrial research has spent significant efforts on finding the solution to improve the thermal stability both by modification of the CeO_2 synthesis and by looking for different types of promoters and stabilizers [72]. Several studies have been carried out on the CeO_2-SiO_2 system. Ceria-promoted Rh, Pd or Pt supported on SiO_2 catalysts were found to be more active than the unpromoted catalysts [70]. CeO_2 supported on SiO_2 has a strong effect on the microstructure of Rh and a slight increase was found in its catalytic activity in the hydrogenolysis of ethane[73,74]. In CO oxidation, Rh was found to act as a site for CO adsorption and ceria providing lattice oxygen necessary for the formation of carbon dioxide. The CeO_2/SiO_2 structure showed significant changes only after exposure at temperatures higher than 600°C, either under O_2 or under H_2[73-75].

Cracium[70] has investigated the preparation and characterization of CeO_2 supported on high surface area SiO_2 catalysts prepared by two different methods (i) incipient wetness using Ce(IV) ammonium nitrate, aqueous solution, and (ii) by grafting using Ce(IV) methoxyethoxide alcoholic solution. After calcinations at 500°C, it was found that larger CeO_2 crystallites on silica were produced by the first method, whereas

mostly amorphous particles were produced by the second method. Moreover, the CeO_2 particle size indicated a better ceria dispersion on the SiO_2 support for the second method than for the first[70, 71]. The BET measurement indicates a decrease in the surface area for the SiO_2 support from 300 m^2/g at 500 °C to 210 m^2/g after calcinations at 800°C. This was explained by the collapse of the silica porous structure at an elevated temperature[70].

Rocchini *et. at*[76], have shown that the reduction properties of CeO_2 are strongly dependent on the amount of silicon. It is recognized that treatment under H_2 strongly affects the reduction properties of M/CeO_2 catalysts, which is indicated by the loss of low-temperature reduction features of ceria. This is a consequence of the blocking of the spillover phenomena and of partial encapsulation of the metal in the sintered support[40]. Rocchini *et. al* [40, 76] found that under some specific conditions, silica, resulting in an enhancement of the ceria reduction properties was due to the formation of a new phase/compound whose arrangement induces stabilization of small ceria crystallites. Structural evidences for the formation of $Ce_{9.33}(SiO_4)O_2$ under reducing conditions were obtained[76]. It has been understood that the formation of this phase enables the limitations imposed by thermodynamics in the reduction of ceria to be overcome and almost 80% of cerium formally shifts to the Ce^{3+} oxidation state in the form of cerium silicate. On reoxidation, this phase decomposes giving amorphous silica and small ceria crystallites, which are much more reactive toward reduction and oxidation. Figure 1.4 gives a summary of the transformation that occurs with silica-doped ceria in comparison to pure CeO_2. It should be noted that the formation of a Ce-Si-O phase enables participation of the bulk oxygen anions in the redox process[76,77].

Trovarelli *et. al* [77] showed that by increasing the amount of silica an increase in the surface area is observed. The surface area drop at high temperature is delayed by more than 200°C compared to pure ceria[77]. Therefore, it is clear that the presence of silica

strongly modifies the textural properties of ceria/silica, since silica does not form a solid solution with ceria and the material consists mainly of large separate domains of the two oxides [77].

Martinez-Arias *et. al* [78], have prepared several alumina supported ceria samples with varying contents (1 – 39 wt %). They have found that two types of ceria entities were observed: aggregated crystalline ceria species (3D-Ce) and dispersed ceria species in the form of two-dimensional patches (2D-Ce). It was concluded that the relative amount of each of these species did not show a linear relationship with the cerium loading: as the cerium content was increased, a trend towards the formation of 3*d*-Ce, to the detriment of 2*d*-Ce, was observed. The ceria entities that could be present in alumina-supported ceria systems were classified according to their different dispersion degrees, approximately as:

(i) dispersed ceria entities, which could in principle include isolated cerium ions, clusters thereof and/or more or less thick CeO_{2-x} patches (or 2D-Ce entities) and

(ii) nondispersed ceria species (*i.e.* ceria aggregates or 3*d*-Ce entities).

Generally[78], it is difficult to characterize these entities and the difficulty increases with the degree of dispersion. Therefore, aggregated ceria entities in a supported ceria system have been more or less characterized, but with the limitation imposed by each characterization technique. However, dispersed ceria entities, have generally been characterized only in an indirect way by considering the lack or insufficient intensity of features due to aggregated ceria entities in ceria-containing samples.

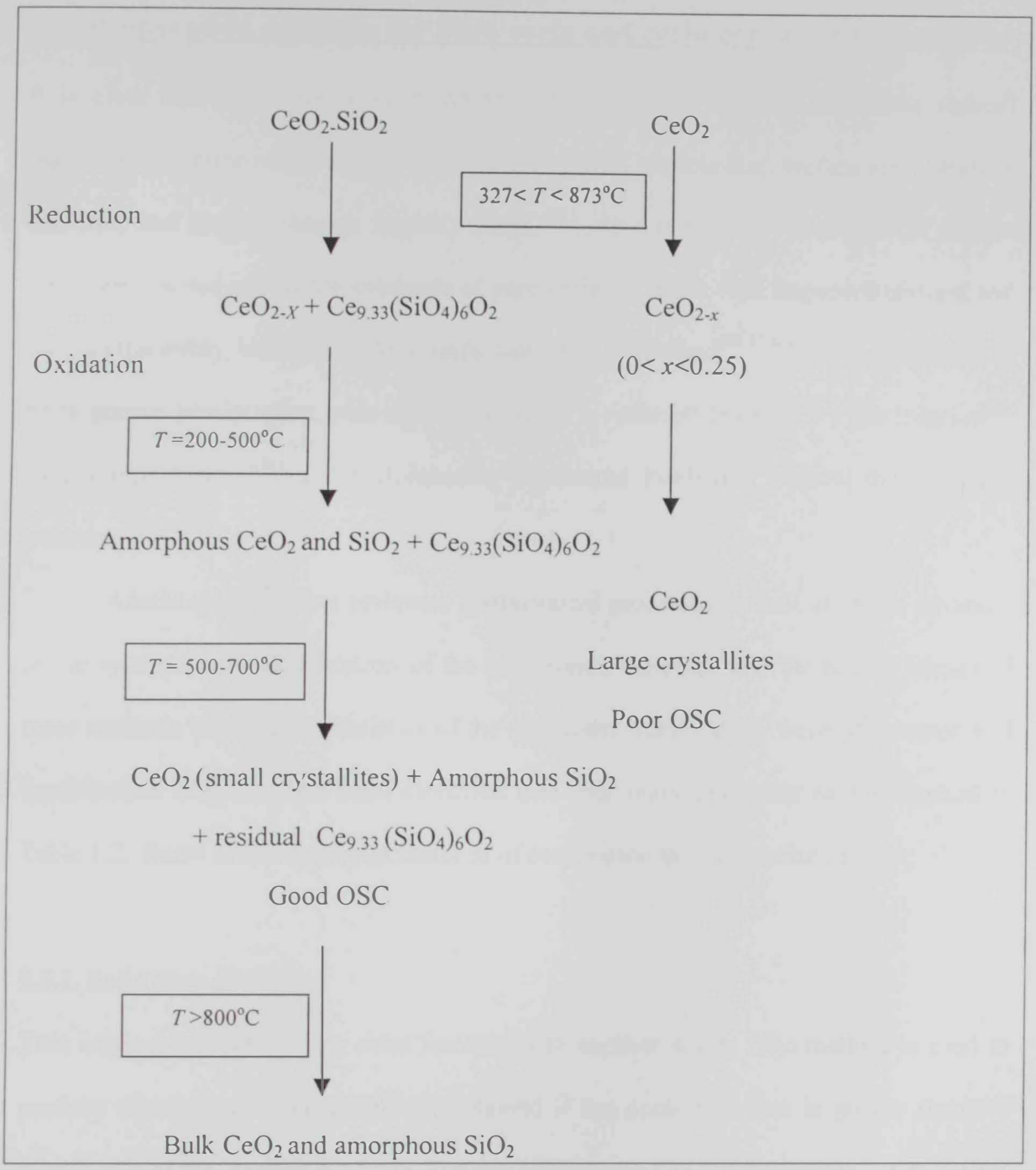

Figure 1.4 Thermal stabilization of ceria with silicon compounds (mechanism).

The scheme summarizes the transformation, which occurs with silica-doped ceria [76,77].

1.5. Preparation methods for pure ceria and ceria containing materials:-

It is clear that the methods of preparation of pure ceria and its containing (based) materials determine properties such as phase structure, particle size, surface area, catalytic activities and oxygen storage capacity (OSC)[79]. As a result, a vast number of studies have been carried out on the synthesis of pure ceria materials with improved textural and thermal durability, which include: a surfactant-assisted method[66,71,80], a coupling route of homogenous precipitation with micro-emulsion[81], reversed micelles[82], precipitation[83] by a mimic method[84] and high-intensity ultrasound irradiation without thermal post-treatment[85].

Adachi *et. al*[79] have reviewed conventional processes as well as recent advances in the synthesis and modification of the ceria based materials and the related impact of these methods on the characteristics of the materials. Accordingly, these preparation and modification methods have been classified into four main categories as summarized in Table 1.2. Some of the important methods of preparation are summarized below:

1.5.1. Solid state method:-

This method depends on the solid reacting with another solid. The method is used to produce ultrafine particles which are obtained if the nucleation rate is greater than the growth rate of the reaction products. For this method there are four main advantages: (i) it gives more uniform and less agglomerated products than those by other methods; (ii) the method is simple, cheaper and convenient and involves fewer solvents and reduces contamination; (iii) the method gives high yields of products[86]. CeO_2 ultrafine particles are prepared by solid-state reactions at room temperature. These particles were found to have very fine particles (~3 nm) with a fluorite type structure (a = 5.42 Å).

BET measurements have shown that the surface area of the particles was 96.2 m^2/g. The use of two different precursors $(NH_4)_2Ce(NO_3)_6$ and $Ce(NO_3).6H_2O$ with NaOH was found to affect the size of the CeO_2 particles[87]. CeO_2 particles are stable for calcinations at temperatures below 550°C. This can be explained according to the formation of $NaNO_3$ as a by product, which coats the newly formed CeO_2 species, preventing them from growing further and thus producing fine panicles of CeO_2. In addition, $NaNO_3$ helps to separate the CeO_2 panicles to prevent them from further agglomeration[88].

1.5.2. Flux method:-

The flux method has been used to produce single crystals of a number of compounds at relatively low temperatures: oxides, sulfides *ect.*, which would otherwise require temperature in excess of 1100°C for conventional solid-state synthesis. This method consists of adding the required precursors ratio to a molten salt mixture often close to a eutectic stoichiometry. Molten salt mixtures either serve the role of a solvent to accelerate the kinetics by enhancing diffusion, since coefficients in the liquid state are lower than those in the solid state, or enter into the reaction with the oxide additives. The flux method has been reported for the preparation of cerium(IV) oxide (CeO_2) powders, with the addition of cerium ammonium nitrate, $[(NH_4)_2Ce(NO_3)_6]$, to an eutectic mixture of molten salts, followed by washing and drying. To evaluate the effect of the molten salts on the powders, three different fluxes were used: KOH/NaOH, $NaNO_3/KNO_3$, and LiCl/KCl eutectic mixtures. Very fine size distribution particles, with a very narrow dimensional range of 10-20 nm were obtained[89].

Table 1.2 List of the categories of the different preparation and modification methods of ceria-based materials, classified by Adachi *et. al*[79].

Category	Methods
Solid to solid synthesis	Ceramic method Mechanical millining
Solid to liquid synthesis	Precursor method Precipitation and coprecipitation method Hydrothermal and solvothermal synthesis Sol-gel method Surface-assisted method Emulsion and micro-emulsion method Flux method Electrochemical method Spray pyrolysis Impregnation method
Gas to solid synthesis	Gas condensation or sputtering Chemical vapor deposition
Modification of bulk and surface	Effect of dopants Structural modification by redox aging Surface modifications

1.5.3. Precipitation and Co-precipitation methods:-

This method is used to prepare fine particle solid materials from soluble precursor solutions. Ceria can be prepared from Ce(III) and/or a Ce(IV) salt solution, $Ce(NO)_3$, $CeCl_3$ or $(NH_4)_2[Ce(NO_3)_6]$, in low concentration. Precipitation can be induced by the addition of a cerium cation solution to the precipitant. However, this approach has little control on the particle size and morphology because of the rapid change of the solution concentration and the discontinuous nature of the formation of the precipitate. Homogenous precipitation can be used to improve the method where, for example urea is slowly decomposed to yield ammonia by the heating of the solution containing the cerium cation and urea. As a result ammonia will be produced slowly and uniformly throughout the course of the precipitation [79].

Co-precipitation is used to prepare mixed oxides. Salts of different metals are dissolved in water, and then precipitated. However, a difference in solubility constants between several precipitating phases can affect the precipitation kinetics, and therefore homogenous precipitation results in the homogenous mixture of fine particles rather than an atomic level mixture[79]. Many ceria-based mixed oxides have been prepared such as the preparation of mixed oxide catalysts of the general formula $Ce_{1-x}La_xO_{2-x/2}$ by co-precipitation from nitrates $Ce(NO_3)_3{\cdot}6H_2O$, $La(NO_3)_3{\cdot}6H_2O$ with ammonium bicarbonate[90], the calcium doping ceria and carbonate composite materials by oxalate co-precipitation[91] and CeO_2-ZrO_2 materials[92,93] *etc.*

1.5.4. Sol-gel method:

The sol-gel process involves the manufacture of an inorganic matrix through the formation of a colloidal suspension, *sol* and the gelation of the sol to form a wet *gel*, which, after drying forms xerogel or areogel. This method is suitable for the synthesis of ultrafine oxide materials at relatively low temperature[79].

However, the sol-gel technique based on the hydrolysis of alkoxides, a technique which has been successfully employed for the preparation of a large number of metal oxides[94 - 96], and pure metal oxides with good thermal stability[97 - 98], has seldom been reported for the preparation of pure ceria material, probably due to its limited solubility in an alcoholic medium.

In general the process involves the following steps:

1. Hydrolysis reaction

Metal alkoxides are popular precursors because of their ability to hydrolyze readily.

$$M(OR)_4 + H_2O \longrightarrow HO\text{-}M\text{-}(OR)_3 + ROH \qquad \text{Eq(1.10)}$$

This process is influenced by the amount of water, by the presence of acid or base catalyst, and solvent.

2. Condensation reaction

The partially hydrolyzed species can link together in a condensation reaction such as:-

$$(OR)_3M\text{-}OH + HO\text{-}M(OR)_3 \longrightarrow (OR)_3M\text{-}O\text{-}M(OR)_3 + H_2O \qquad \text{Eq(1.11)}$$

or

$$(OR)_3M\text{-}OR + HO\text{-}M(OR)_3 \longrightarrow (OR)_3M\text{-}O\text{-}M(OR)_3 + ROH \qquad \text{Eq(1.12)}$$

3. Sol formation

Sol formation occurs when the solution of monomer is allowed to condensate into cross-linked polymers with an average size of several nanometers.

4. Gel formation

Gel can be formed from particulate sols when attractive forces cause them to stick together in such a way as to form a network. A sol, or a solution can be transferred into a colloidal (or polymeric) gel by going through what is termed a gel-point[99], giving rise to a network which entraps the remaining solution. Another intermediate form between the gel and the precipitate is called a gelatinous precipitates. This results in an initial aggregate with the formation of a 3-dimenional porous network with identical types of links.

5. Ageing

A range of processes including the formation of further cross-links associated with the shrinkage of the gel can lead to a change in the structure and properties by ageing of the formed gel.

6. Drying

Drying by evaporation under normal conditions gives rise to capillary pressure that causes shrinkage of the gel network and pore collapsing. The resultant dried gel under normal conditions is called a *xerogel*. However, if the gel is placed in autoclave and dried under supercritical conditions, there is no interface between the liquid and the vapor, and hence there is no capillary pressure and relatively little shrinkage, and the product is called an

aerogel. Most gels are amorphous, noncrystalline even after drying, but many crystallize after heating.

7. Sintering

The specific surface area of sol-gel materials decreases during thermal treatments. The process of progressive removal of porosity during thermal treatment is termed sintering. In terms of thermodynamics, sintering originates from the specific surface area of the porous material[95]. Therefore, the specific surface area should tend to decrease; a process which can proceed according to two types of pore evolution:

(i) By changing the shape of the pore but not the volume.

(ii) By eliminating the pore.

The first type produces no material densification whereas the second produces material shrink without mass loss[95].

In fact, sol-gel processing is not only considered a unique technique, but is in fact a very broad type of procedure that centralizers around a single scheme as presented in Figure 1.5.

1.5.5. Surfactant-assisted method:-

The method involves the preparation of porous materials with controlled formation of mesopores and high area surface. Surfactants are hydrocarbons chains which consist of a nonpolar part (lipophilic) and a polar part (hypohilic), and are used as templating agents. The method inhances the creation of mesopores with a regular structure[100]. The surfactants may be anionic, cationic or amphoteric. High surface area mesoporous ceria and ceria zirconia have been prepared by this method using a cationic surfactant (cetyltrimethylammonium bromide). The mean crystalline sizes of the particles

distributed have been found to be in the region of 2-5 nm for ceria and 4-18 nm for ceria-zirconia, respectively. Surface areas in excess of 200 m^2g^{-1} are obtained after calcinations at 500°C[65, 67, 101].

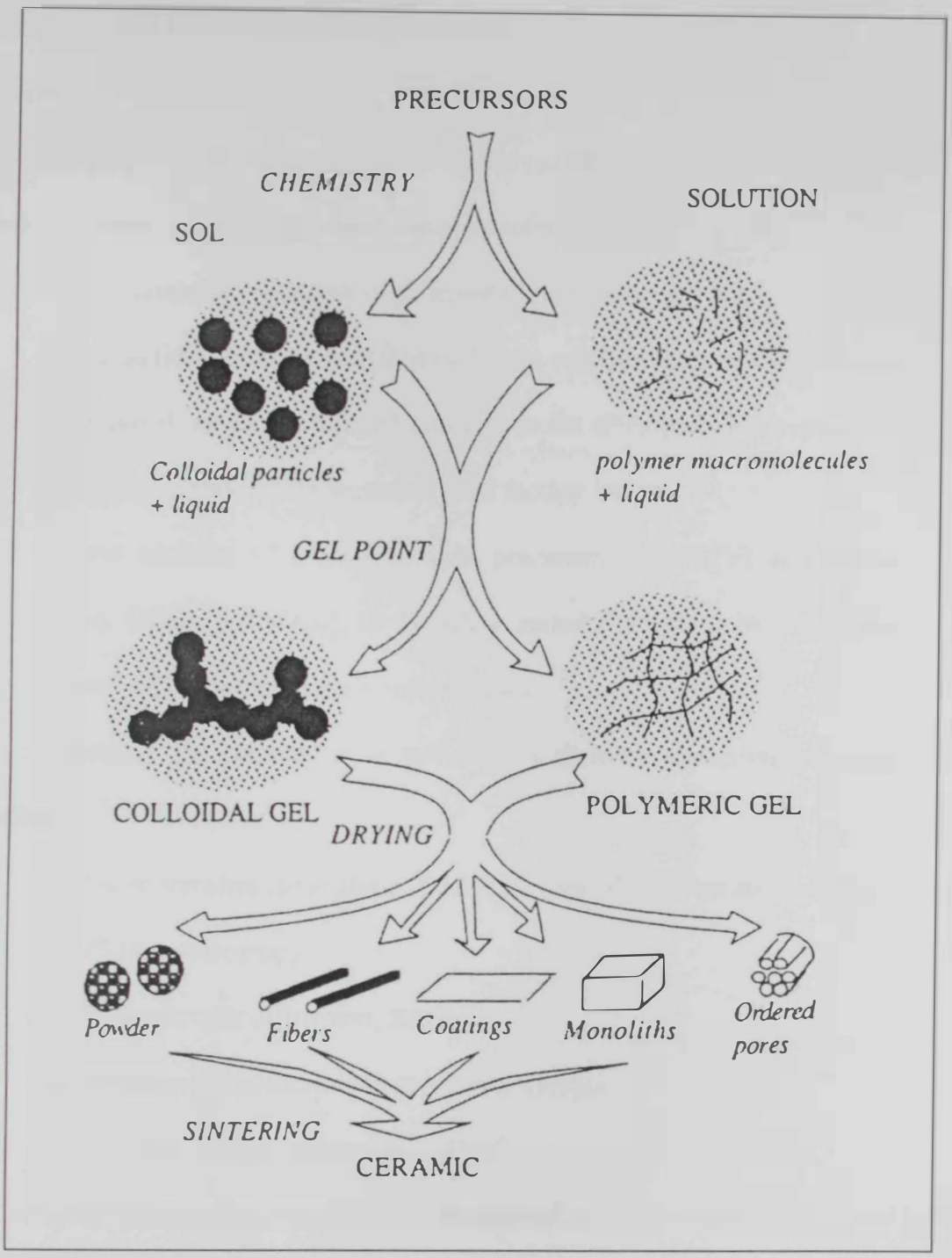

Figure 1.5 Simplified chart of sol-gel processes[95] .

1.6. Aims and objectives of this project:-

The aims and objectives of this project are as follows:

1. To prepare pure ceria materials by the hydrolysis of Ce(IV) tetra-isopropoxide in both (i) neutral and (ii) highly basic aqueous solutions.

2. To prepare ceria/silica materials of different (w/w) percentage by:

   (i) the addition of ceria gel (formed by the prehydrolysis of Ce(IV) tetra-isopropoxide in an isopropanol solution) to the silica particles prepared by the Stöber method while present in their mother liquor.

   (ii) the addition of a soluble ceria precursor, cerium(IV) ammonium nitrate, $(NH_4)_2Ce[(NO_3)_6]$, to the silica particles prepared by the Stöber method while present in their mother liquor.

3. To characterize the prepared ceria materials by different characterization techniques including:

   (i) Thermogravimetric analysis, TGA, in a flow of different atmospheres;

   (ii) FTIR spectroscopy;

   (iii) X-ray powder diffraction, XRD;

   (iv) Nitrogen gas adsorption/desorption technique.

   (v) Scanning electron microscopy, SEM.

4. To evaluate the structural and textural characteristics of the materials produced by the indicated preparation methods of preparation as possible routes for the preparation of textured ceria and ceria containing materials. The preparation – structure – properties relationship will be addressed in this work.

Chapter 2

Materials, Methods and Techniques

Chapter 2: Material, methods and technique

2.1. Parent materials:-

Cerium (IV) isopropoxide, $Ce[OCH(CH_3)_2]_4.C_3H_7OH$, *CIP*, powder, product of Alfa Aesar; Isopropanol, 99.7+%, $(CH_3)_2CHOH$ (water contents < 0.05%), product of Merck; ammonium hydroxide, NH_4OH (25% NH_3), 99.99%, product of Merck; tetraethyl orthosilicate, 98% $Si(OC_2H_5)_4$, ***TEOS***, liquid, product of Sigma-Aldrich Co., Ltd., Germany; and ethyl absolute alcohol, C_2H_5OH, analytical grade products supplied by Alfa Acer; were used as received.

2.2. Preparation methods:-

2.2.1. Preparation of pure ceria materials by the sol-gel method:-

2.2.1.1. Neutral and basic preparation:-

At room temperature, 0.01 mole of cerium(IV) isopropoxide was dispersed in 50 ml of isopropanol (containing traces of water < 0.05%) by the aid of ultrasonic radiation in a conventional small bench top ultrasonic bath for a period of 10 minutes. During this process some hydrolysis occurred due to the traces of water (< 0.05%) present in the isoproanol. Thus, a translucent stable gel like dispersant was produced. The resultant dispersion was transferred into a 600 ml beaker containing 207.0 ml of absolute alcohol and 155 ml of water for the ***neutral*** preparation (or 155 ammonia solution 25%, for the ***basic*** preparation). A white opaque sol was formed directly instantly. The solution was magnetically stirred at *ca.* 400 rpm. The sol was kept under stirring for 1 h. The resultant solution was aged for 1 week. The gelatinous precipitate thus formed was filtered off using Whatman filter paper. The collected materials were left to dry overnight at 60°C and allowed to dry further at 120°C for 24 h. The resultant materials are termed as Ceria-

N120 and Ceria-B120 for the neutral and the basic preparations respectively. Portions of the Ceria-N120 and Ceria-B120 materials were calcined in a muffle furnace at 650°C for 3 h. The calcined materials are named after their respective precursors as Ceria-N650 and Ceria-B650 for the neutral and the basic preparations.

2.2.2. Preparation of composite ceria/silica materials:-

2.2.2.1. Preparation of the pure silica material:-

Pure silica materials were prepared similar to the Stöber method[1], where 19.0 ml of TEOS was added to 207.0 ml of absolute alcohol and the hydrolysis was initialized by the addition of 155 ml of ammonia (within 1 min) with magnetic stirring (400 rpm) resulting in the formation of the Stöber silica sol. The sol was maintained under constant stirring for 1 h. The resultant solution was aged for 1 week. The gelatinous precipitate thus formed was filtered and then dried overnight at 60°C followed by further drying at 120°C for 24 h. The material thus produced was termed as uncalcined pure silica. Portions of the uncalcined material was calcined, at 650°C for 3 h. The calcined material, named after its precursor is calcined pure silica.

2.2.2.2. Preparation of 10% and 20% ceria/silica materials from cerium (IV) isopropoxide, CIP:-

Silica supported with 10 and 20% ceria was prepared as follows. A calculated amount of CIP corresponding to 10% or 20% (w/w ceria/silica) was dispersed in 50 ml of isopropanol by the aid of ultrasonic radiation in a conventional small bench top ultrasonic bath for a period of 10 min. This led to the dispersion and hydrolysis of CIP and subsequent formation of the gel. The resultant gel was transferred into a beaker containing freshly prepared Stöber silica sol produced by the method described above.

The solution was magnetically stirred at *ca.* 400 rpm. The sol was stirred for 1 h. The resultant solution was aged for 1 week, filtered off and dried as for the pure silica. The material thus produced from the cerium alkoxide precursor was termed uncalcined 10%Alk and 20%Alk ceria/silica materials respectively. Portions of the uncalcined materials obtained by the above different methods were calcined, at 650°C for 3 h. The calcined materials, named after their respective precursors are calcined 10%Alk, 20%Alk materials.

2.2.2.3. Preparation of 10% and 20% ceria/silica materials from cerium(IV)-ammonium nitrate, CAN:-

Silica supported with 10 and 20% ceria was prepared as follows. A calculated amount of CAN corresponding to 10% or 20% (w/w ceria/silica) was dispersed in 50 ml of doubly distilled water. The resultant solution was transferred into a beaker containing freshly prepared Stöber silica sol produced by the method described above. The solution was magnetically stirred at *ca.* 400 rpm. The solution was maintained at constant stirring for 1 h. The resultant solution was aged for 1 week, filtered off and dried as above. The materials thus produced from CAN as soluble inorganic precursors are termed uncalcined 10%Ing and 20%Ing ceria/silica materials respectively. Portions of the uncalcined materials obtained by the above different methods were calcined, at 650°C for 3 h. The calcined materials, named after their respective precursor are calcined 10%Ing and 20%Ing ceria/silica materials.

2.3. Experimental techniques:-

2.3.1. Thermogravimetric analysis (TGA):-

Thermogravimetric Analysis (TGA) was carried out using a Thermogravimetric Analyzer, TA Instruments GA 2950, (USA). A ceramic sample boat was used. Samples weighing 10.0 ± 0.1 mg were heated in a ceramic sample boat up to 900°C at 10°Cmin^{-1} and in a stream (40 mlmin^{-1}) of nitrogen gas or air.

2.3.2. Fourier transform infrared (FTIR) spectroscopy:-

FTIR spectra, using the KBr disc technique, for the samples were carried out using a Fourier Transform Infrared Spectrophotometer, Nicolet FT-IR Magna-IR 560 system (USA), in the range 4000-400 cm^{-1}; the number of scans used was 40 and the resolution was 4 cm^{-1}.

2.3.3. X-ray powder diffractometry:-

Powder X-ray diffraction (XRD) patterns were obtained using a Philips PW1840 diffractometer system at room temperature. Diffraction patterns were obtained with Ni-filtered Cu-$K\alpha$ radiation (λ = 0.15418 nm). The patterns obtained were matched with standard cards[2] for the purpose of phase identification. The crystallite size of the ceria powder was estimated from the Scherrer equation[3] :

$$d = 0.9\lambda / [(\beta-\beta_o)(\beta\cos\theta)] \qquad \text{Eq(2.1)}$$

where d is the crystallite size; λ is the wavelength of the incident X-ray; θ is the diffraction angle for the (111) line and β is the half-width of the peak.

2.3.4. Scanning electron microscopy (SEM):-

SEM micrographs were obtained, using a JSM-5600 model, Jeol microscope (Japan). The samples used were coated with gold before investigation.

2.3.5. Nitrogen adsorption:-

Apparatus:-

Nitrogen adsorption/desorption isotherms at 77 K were measured using a model ASAP 2010 Micromeritics Instrument Corporation, (USA). Prior to measurement, all samples were outgassed for 2 h at 150°C to 0.1 Pa. The specific surface area, S_{BET}, was calculated applying the BET method[4]. Porosity distribution in the mesopore range was generated by the BJH analysis[5] using the instrumental software. Assessments of microporosity were made from *t*-plot constructions, using the Harkins-Jura correlation[6] for *t*-thickness as a function of normalized pressure, p/p_o. *t*-Plot surface areas, S_t, were calculated from slope analysis of the *t*-plots according to the standard methods[7]. The micropore surface area, S_{mic}, area corresponding to the gas condensed in micropores, was calculated as

$S_{mic} = S_{BET} - S_t$.

2.4.Principles of characterization of porous materials by N_2 adsorption:-

The gas adsorption process on solid porous materials is a complex phenomenon involving mass, energy interaction and the phase diagram. Many theories have been have been put forward suitable for application under either specific or general conditions. There are many references in the literature for the application of this method given by IUPAC[8], Greeg and Sing[9], Webb and Orr [10] and more recently by Rouquerol's and Sing[11]. The following sections give an overview for the process and how different aspects of powdered materials (*e.g.* surface area, porosity type and pore size) can be characterized based on an N_2 adsorption isotherm.

According to IUPAC[8] *Adsorption* is the enrichment of one or more components in the interfacial layer. *Physisorption* is a general phenomenon that occurs whenever an adsorbable gas (the adsorptive) is brought into contact with the surface of a solid (the

adsorbent) at low temperature. The adsorption isotherm is the relation between the amount adsorbed and the equilibrium pressure of the gas. Since most adsorbents of high surface area are porous, its often useful to distinguish between the external surface and the internal one. The *External Surface* is usually regarded as the envelope surrounding the discrete particles or agglomerates, but is difficult to define precisely because solid surfaces are rarely smooth on the atomic scale. As a convention, the external surface is taken to include all the prominence and also the surface of those cracks which are wider than they are deep. The *Internal Surface* then comprises the walls of all cracks, pores and cavities whose areas are deeper than they are wide and which are accessible to the adsorptive. In practice, the demarcation is likely to depend on the methods of assessment and the nature of the pore size distribution.

2.4.1. Surface area:-

The surface area, S, of the adsorbent materials may be calculated from the relation

$$s = n_m \cdot N_A \cdot \delta_m \qquad \text{Eq(2.1)}$$

Where, n_m is defined as the amount of adsorbate needed to cover the surface with a close-packed array; δ_m is the area effectively occupied by an adsorbed molecule in the complete monolayer, and N_A is Avogadro's number. The specific surface area, s, refers to the unit mass of adsorbent and is given by $S = s/m$.

The Brunauer-Emmett-Teller (BET) method[4] is the most widely used procedure for the determination of the surface area of solid materials and involves the use of the BET equation:

$$\frac{p}{V_a(p_o - p)} = \frac{1}{V_m C} + \frac{C-1}{V_m C}\left(\frac{p}{p_o}\right) \qquad \text{Eq(2.2)}$$

in which V_a (at STP) is the quantity of gas adsorbed at pressure p; V_m (at STP) is the quantity of gas adsorbed when the entire surface is covered with a mono adsorbed layer;

p_o is the saturation pressure of the gas. The value of the constant C can be expressed simply as:

$$C \propto \exp \frac{q_1 - q_L}{RT} \qquad \text{Eq(2.3)}$$

where q_1 is the heat of adsorption of the first layer; qL is the heat of liquefaction of the adsorptive; R is the gas constant, and T the absolute temperature.

In principle, a plot of $p/[V_a(p_o\text{-}p)]$ versus p/p_o should yield a straight line with intercept $1/V_mC$ and slope $(C\text{-}1)/V_mC$. Then, the value of V_m and C can be obtained. Finally, the value of δ_m may be calculated from the formula below (assuming close packing at the surface):

$$\delta_m = (4)(0.866)\left[\frac{M}{4(2N_A\rho)^{1/2}}\right]^{2/3} \qquad \text{Eq(2.4)}$$

where M is the molecular weight; and ρ the density of the liquid adsorbate. The area occupied by a nitrogen molecule is generally taken as 16.2 $Å^2$ at liquid nitrogen, temperature.

The BET equation (2.2) requires a linear plot of $p/[V_a(p_o\text{-}p)]$ versus p/p_o which for most solids, using nitrogen as the adsorbate, is restricted to a limited region of the adsorption isotherm, usually in the p/p_o range of 0.05 to 0.30. This linear region is shifted to lower relative pressures for microporous materials. The S_{BET} in m^2g^{-1}, surface area of the sample can be expressed as:

$$S_{BET} = \frac{V_m N_A \delta_m}{M\, m} \qquad \text{Eq(2.5)}$$

where M (g mol^{-1}) is the molecular weight of the adsorbate and m and is the mass of the test sample. Nitrogen is the most widely used gas for surface area determinations since it exhibits intermediate values for the C constant (50-250) on most solid surfaces,

precluding either localized adsorption or behavior as a two dimensional gas, since it has been established[12, 13] that the *C* constant influences the value of the cross-sectional area of an adsorbate.

2.4.2. Adsorption isotherms:-

The surface area and porosity of an adsorbent can be understood by examining the adsorption isotherm which can be defined as the relationship between the amount adsorbed by unit mass of solid and the equilibrium pressure or relative pressure, at a known temperature.

2.4.2.1. Types of isotherms:-

Isotherms can be grouped into six classes according to the IUPAC[8] classification, see Figure 2.1. The first five types (I to V) of the classification were originally proposed by S. Brunauer, L.S. Deming, W.S. Deming and E. Teller, BDDT classification [14], sometimes referred to as the Brunauer classification.

The six major types of isotherms in the IUPAC classification still provide the basis for the various physisorption isotherms. However, more recently following refined classification involving the subdivision of types I, II, and IV has been suggested[11].

Type I isotherms:

The main feature of a reversible Type I isotherm is the sharp rise observed at low relative pressure followed by a long plateau, which is indicative of a relatively small amount of multilayer adsorption on the open surface. "Micropore filling" may take place either in pores of molecular dimensions (*i.e.* primary micropore filling) at very low p/p_o or in wider micropores (co-operative filling) over a range of higher p/p_o. The corresponding

isotherms here are designated *Types Ia* and *Ib*, respectively, as displayed in Figure 2.2. In their 'ideal' forms, both types are reversible and both have almost horizontal plateaux over a wide range of high p/p_o.

Type II isotherms:

Type II isotherms indicate the formation of an adsorbed layer whose thickness increases progressively with increasing relative pressure until p/p_o reaches 1 atm. A truly reversible Type II isotherm is normally associated with monolayer-multilayer adsorption on an open and stable external surface of a powder, which may be non-porous, macroporous or even, to a limited extent, microporous. This form of isotherm is now termed *Type IIa* (see Figure 2.2). The smooth, non-stepwise character of a Type IIa isotherm is often associated with energetic heterogeneity in the adsorbent-adsorbate interactions. A sharp point *B* (knee point) and a correspondingly high value of *C*(BET) usually indicates the formation of a well defined monolayer, while the absence of an identifiable point *B* represents the completion of the monolayer and the beginning of the formation of the multilayer.

Type IIb isotherms are obtained with aggregates of plate-like particles, which therefore possess non-rigid slit shaped pores. Because of the delayed capillary condensation it is able to proceed on the particle surface until a high p/p_o is reached. Once the condensation has occurred, the state of the adsorbate is changed and the desorption curve therefore follows a different path until the condensate becomes unstable at a critical p/p_o value.

Type III isotherms:

True Type III isotherms are confined to a few systems, in which the overall adsorbent-adsorbate interactions are weak in comparison with relatively strong adsorbate-adsorbate interactions. The monolayer density tends to be unevenly distributed on the adsorbent surface with a relatively high concentration of molecules located on the most active areas. As the pressure is raised the average monolayer concentration is increased, but before it can become close-packed over the complete surface, the monolayer coverage is overtaken by a form of co-operative multilayer adsorption in which molecules are clustered around the most favorable sites.

Type IV isotherms:

Type IV isotherms exhibit a hysteresis loop. There are two types of hysteresis loops. In the first case (a Type IVa loop), the loop is relatively narrow, the adsorption and desorption branches being almost vertical and nearly parallel; in the second case (a Type IVb loop), the loop is broad, the desorption branches are much steeper than the adsorption branch. Generally, the location of the adsorption branch of a Type IVa isotherm is governed by delayed condensation, whereas the steep desorption branch of a Type IVb isotherm depends on the network percolation effects.

The less common, completely reversible isotherm in Figure 2.2 is now designated a Type IVc isotherm. If the riser is almost vertical at a characteristic p/p_o value, reversible pore filling and emptying appear to occur in a narrow range of uniform near cylindrical pores of critical size; the reversibility being dependent on the adsorptive and the operational temperature.

Type V isotherms:

A type *V* isotherm is very similar to that of a Type III isotherm for a similar gas-solid system (*e.g.* water/carbon). It exhibits a hysteresis loop which can be associated with the mechanism of pore filling and empting. However, the sharp increase in adsorption at higher p/p_o is dependent on the pore size. For example, the ultramicropores in a molecular sieve carbon are filled with water at a much lower p/p_o than are the wider pores in a super microporous carbon.

Type VI isotherms or stepped isotherm, involve a layer by layer adsorption process. Such isotherms are given by the adsorption of simple non-polar molecules (*e.g.* argon, krypton and xenon) on uniform surfaces (*e.g.* the basal plane of graphite). The steps become less sharp as the temperature is increased. The vertical risers can be regarded as the adsorbed layer boundaries and the centers of the treads (inflection points) as the layer capacities. Useful information concerning the surface uniformity and adsorbate structure can be obtained from the relative layer capacities and the presence of sub-steps[11].

2.4.2.2. Hysteresis loops:-

Hysteresis loops, which appear in the multilayer range of physisorption isotherms, are generally associated with capillary condensation. The major different types are given in Figure 2.3 according to IUPAC classifications[8].

Type H1 is a fairly narrow loop with very steep and nearly parallel adsorption branches. It is associated with a narrow distribution of uniform pores.

Type H2 is broad with a long and almost flat plateau and a steep desorption branch. In this type, pore structures are complex and tend to be made up of interconnected networks of pores of different sizes and shapes.

Types H3 and *H4* do not terminate in a plateau at high a region p/p_o . Type *H3* loops are characterized by the aggregates of platy particles or adsorbents containing slit shaped pores.

Type H4 loops are also typified by slit shaped pores, as in activated carbons, but in this case the pore size distribution is mainly in the micropore range[11].

2.4.3. Characterization of porosity:-

Pores are classified according to their sizes[8] as:

a- Pores with a diameter exceeding 50 nm are called macropores.

b- Pores with a diameter not exceeding 2 nm are called micropores.

c- Pores with a diameter between 2-50 nm are called mesopores.

The porosity of powders and other porous solids can be characterized by gas adsorption studies. Two common techniques for describing porosity are the determination of total pore volume and pore size distribution. For the evaluation of the porosity of most solid materials, nitrogen at 77 K is the most suitable adsorbate.

2.4.3.1. Total pore volume and average pore radius:-

The total pore volume is derived from the amount of gas adsorbed at a relative pressure close to unity, by assuming that the pores are then filled with liquid adsorbate. If the solid contains no macropores the isotherm will remain nearly horizontal over a range of p/p_o approaching unity and the pore volume is well defined. However, in the presence of macropores the isotherm rises rapidly near p/p_o = I and in the limit of large macropores may exhibit an essentially vertical rise. In this case the limiting adsorption can be identified reliably with the total pore volume assuming careful temperature control of the

sample. The volume of nitrogen adsorbed (V_{ads}) can be converted to the volume of liquid nitrogen (V_{liq}) contained in the pores using the relation

$$V_{liq} = \frac{p_a V_{ads} V_m}{RT} \qquad \text{Eq(2.6)}$$

in which p_a and T represent the ambient pressure and the temperature, respectively, and V_m is the molar volume of the liquid adsorbate (34.7 cm^3mol^{-1} for nitrogen). Since pores which would not be filled below a relative pressure of 1 have a negligible contribution to the total pore volume and the surface area of the sample, the average pore size can be estimated from the pore volume. Assuming cylindrical pore geometry, the average pore radius r_p can be expressed as:

$$r_p = \frac{2V_{liq}}{S} \qquad \text{Eq(2.7)}$$

where V_{liq} is obtained from equation (2.7) and S is the BET surface area. For other pore geometries a knowledge of the shape of the hysteresis in the adsorption/desorption isotherm is required.

2.4.3.2. BJH Method for mesopore and macroporous materials:-

Many different mathematical procedures were proposed for the derivation of the pore distribution from the nitrogen adsorption isotherm. The Barrett, Joyner and Halenda, BJH[5], method is still the most popular. Assuming that the initial relative pressure (P/P_o) is close to unity, *e.g.* $p/p_o = 0.995$, all pores are filled with liquid. The method can be outlined as follows[10]:

For simplicity, imagine the isotherm as a series of steps downward of equal relative pressure, say 0.98, 0.96, 0.94, 0.92, *etc.* The amount of adsorptive lost in each step (after conversion from a gas volume at STP) represents the core volume of pores emptied in that step. The thickness of the adsorbed layer remaining on the pore walls, t, is

calculated from a thickness relationship, for example the Halsey equation[15] or the Harkins and Jura[6] equation. The latter may be used to express the statistical thickness as:

$$t = \left[\frac{13.99}{0.034 - \log_{10}\left(\frac{p_o}{p}\right)} \right]^{1/2} \qquad \text{Eq(2.8)}$$

Then from the Kelvin equation, which may be written for the process of pore filling *i.e.* adsorption as as:

$$\ln\frac{p}{p_o} = -\frac{\gamma \upsilon}{RT r_m} \qquad \text{Eq(2.9)}$$

where γ is the liquid surface tension, and υ is the molar gas volume of the condensed adsorbate. By substitution of $(r - t)$ for r_m, a value of r can be calculated. The shape of the pore also has to be specified. For cylindrical pores for example, the pore volume V_p is given by:

$$V_p = \pi r^2 L \qquad \text{Eq(2.10)}$$

The area of each pore is a constant and can be calculated from the pore volume, as follows:

$$A_p = \frac{2V_p}{r_p} \qquad \text{Eq(2.11)}$$

This is only for the first step down the isotherm. The calculation should be repeated for the next series of steps. A pore distribution of the radius will not obtained until the process is completed. Such a tedious repetitive calculation can easily be carried out computationally[10]. With the aid of an appropriate computational tool several thickness expressions and pore shapes can be examined. Other pore models include the slit shape

for plate-like materials or cavities formed by touching spheres in the case of sintered objects.

2.4.4. Assessment of microporosity by the *t*-method:-

Lippens and de Boer [7] have transformed the experimental isotherm into a *t*-plot as follows: the amount adsorbed, *n*, is replotted against *t*, the standard multilayer thickness on the reference non-porous material at the corresponding p/p_o. Any difference in shape between the experimental isotherm and the standard *t*-curve occurs as a non-linear region of the *t*-plot and/or a finite (positive or negative) intercept of the extrapolated *t*-plot (*i.e.* at $t = 0$). A specific surface area, denoted *S(t)* can be calculated by this method from the slope, $s = V_a/t$, of a linear section.

$$S_t\ (m^2g^{-1}) = s \times 15.47 \qquad \text{Eq(2.12)}$$

In the absence of micropores there is a good agreement between the *t*-method surface area S_t and the S_{BET} one, When micropores are present the *t*-plot will exhibit a positive intercept. The intercept, *i*, in the *t*-plot, when converted to a liquid volume, gives the micropore volume, V_{mic}, *i.e*:

$$V_{mic} = i \times 0.001547\ (cm^3) \qquad \text{Eq(2.12)}$$

The micropore surface area, S_{mic}, then is the difference between the BET surface area and the external surface area from the *t*-plot,*i.e*:

$$S_{mic} = S_{BET} - S_t \qquad \text{Eq(2.13)}$$

Typical *t*-plots are shown in Figure 2.4.

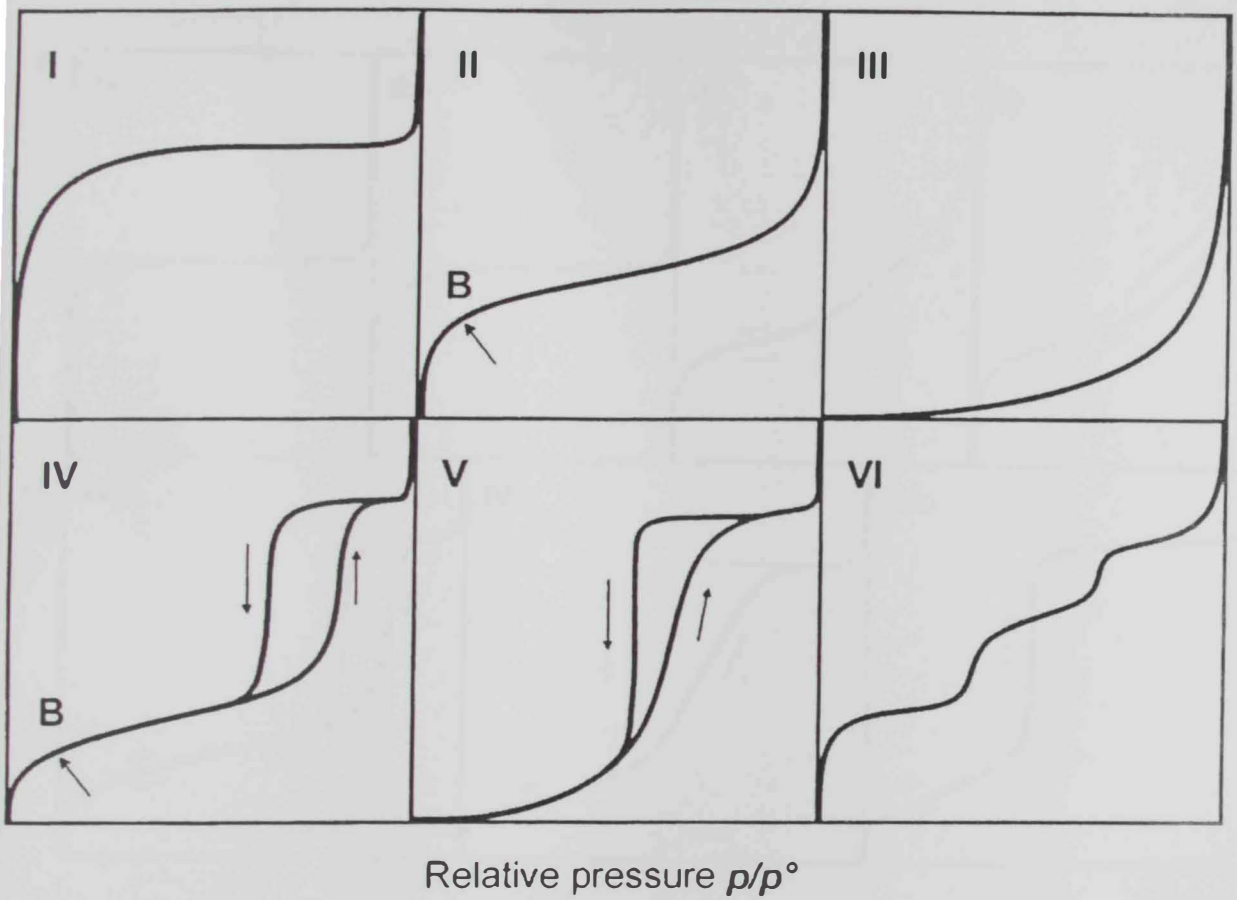

Figure 2.1 The IUPAC classification of the various types of various isotherms[8].

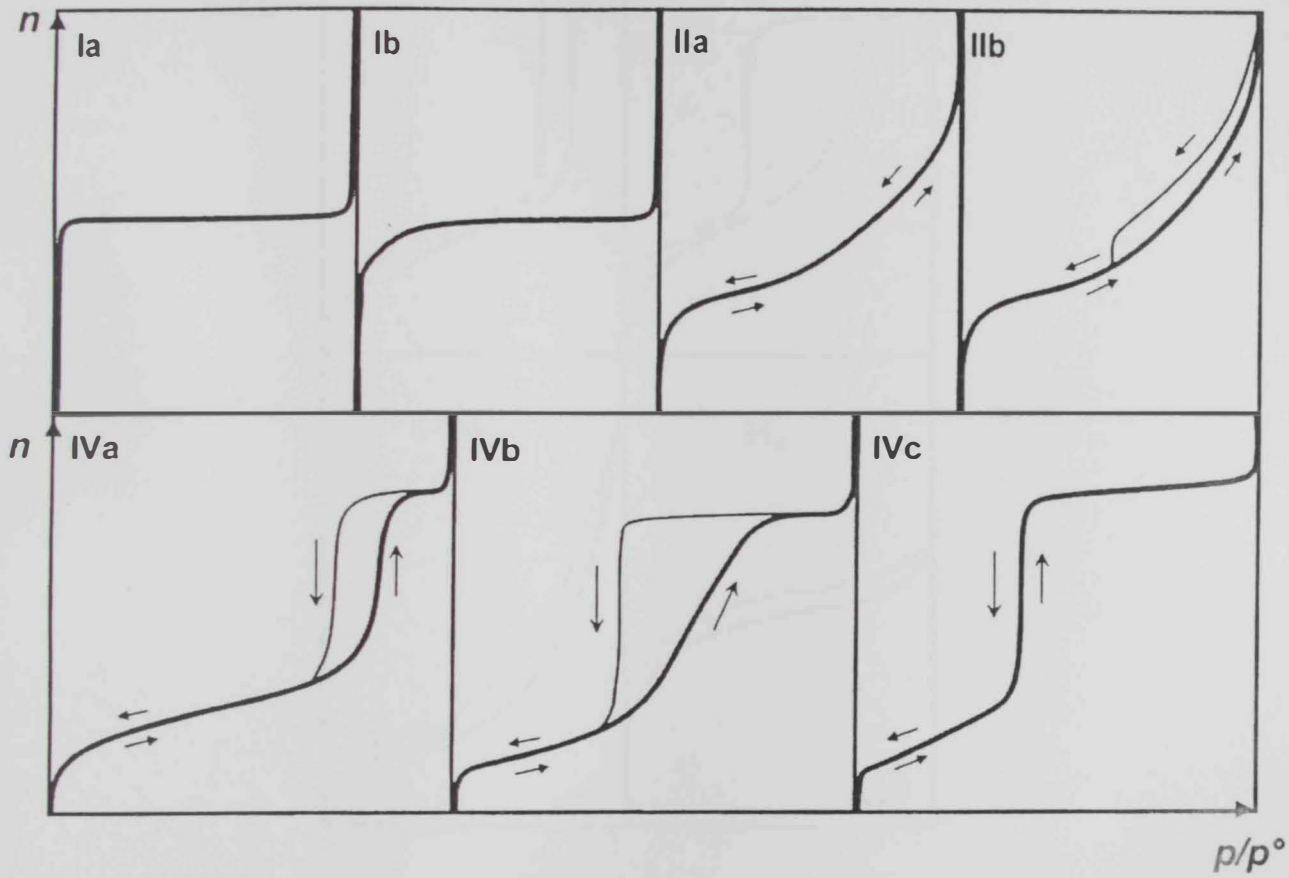

Figure 2.2 An Extended classification of the various types of isotherms[11].

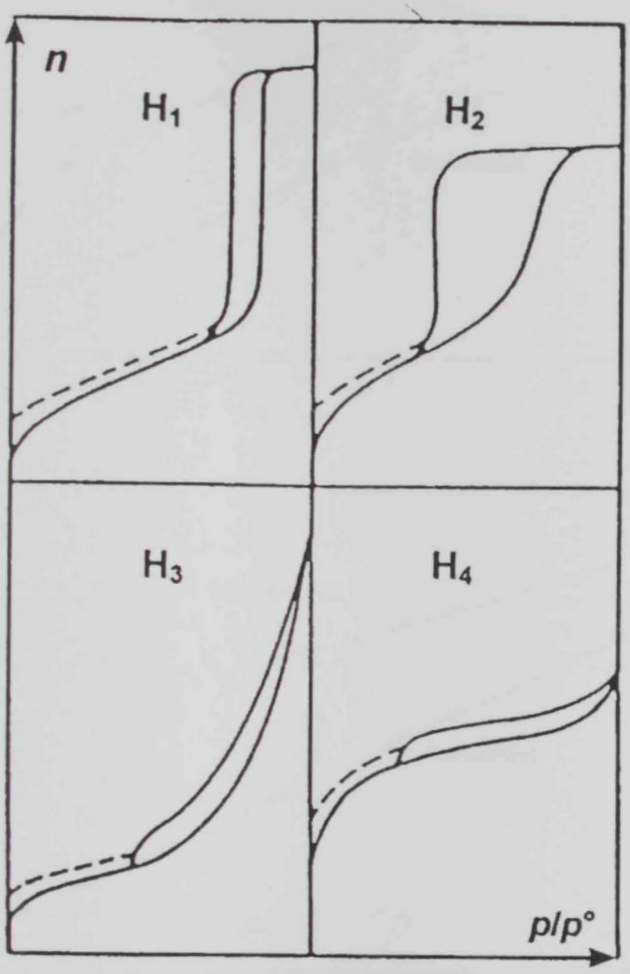

Figure 2.3 The IUPAC classification of hysteresis loops[8].

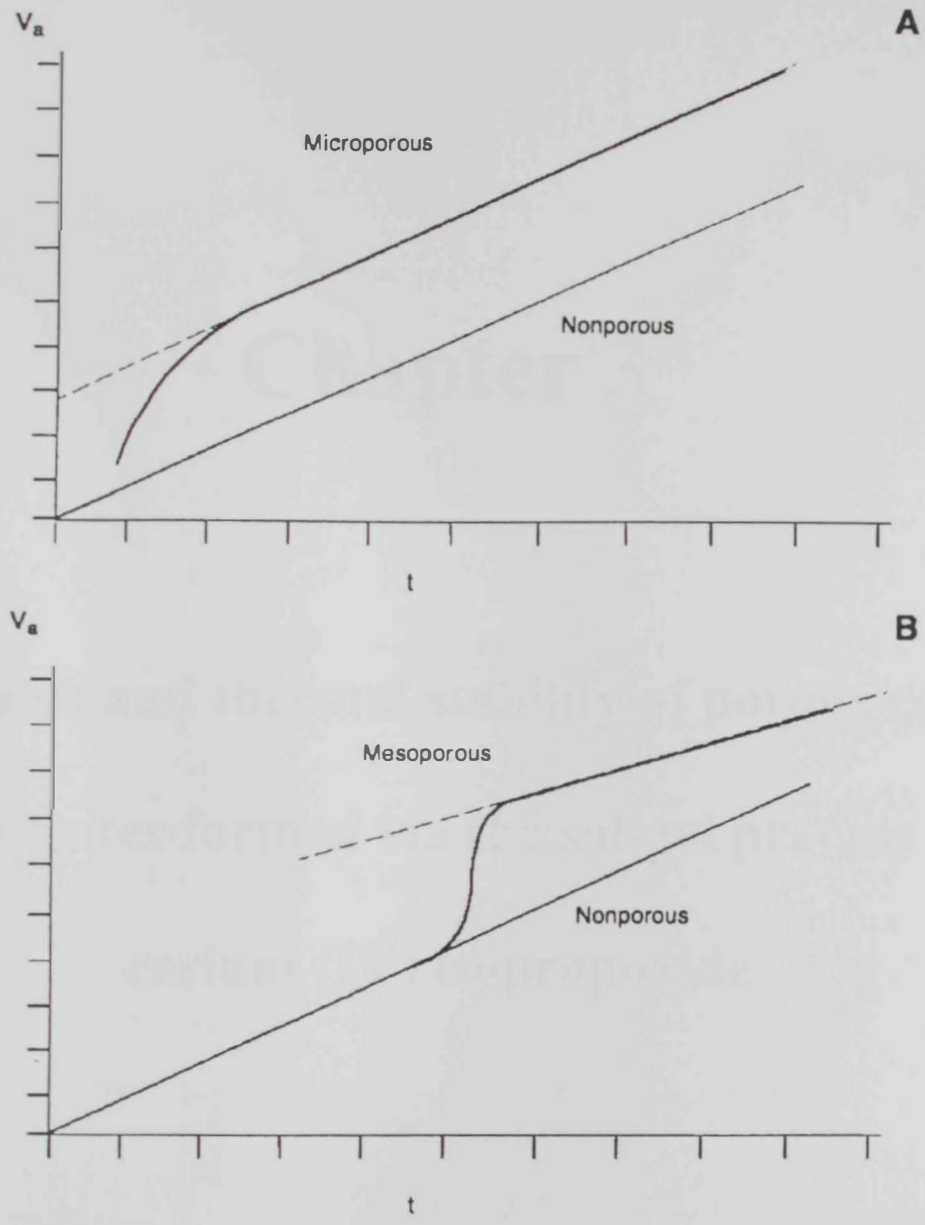

Figure 2.4 Idealized example of a *t*-plot for (A) a microporous and (B) a mesoporous solid material. Both examples show also the *t*-plot obtained for a nonporous sample[11].

Chapter 3

Textural and thermal stability of porous ceria aggregates formed via the sol-gel process of cerium (IV) isopropoxide

Chapter 3: Textural and thermal stability of porous ceria aggregates formed via the sol-gel process of cerium (IV) isopropoxide

Ceria, CeO_2, is one of the most important catalytic materials and it can play multiple roles owing to its ability to release and uptake oxygen under catalytic reaction conditions with the preservation of its fluorite structure[1,2]. As mentioned in the introduction previously, chapter 1, significant efforts have been made by industry on finding ways to improve the thermal stability of ceria both by modification of the synthesis of CeO_2 and by looking at different types of possible stabilizers[3]. A large number of studies have been reported in the literature for the synthesis and modification of ceria-based materials with different stabilizers[4]. Other methods have been also reported for the preparation of pure ceria with improved textural and thermal stability. However, the sol-gel technique based on the hydrolysis of alkoxides, a technique which has been successfully employed for the preparation of a large number of metal oxides[5,6], and metal oxides with good thermal stability[7,8], has seldom been reported for the preparation of pure ceria material, probably due to its limited solubility in an alcoholic medium.

The aim of this part (chapter 3) of the work is to report a two step sol-gel process in which cerium (IV) isopropoxide was dispersed in isopropanol by the aid of ultrasonic radiation to overcome the solubility problem. The hydrolysis reaction took place in neutral or in basic isopropanol media, followed by subsequent aging, drying and calcination for 3 h at 933 K. Textural characteristics of ceria powders produced through this method were characterized via thermogravimetric analysis (TGA), X-ray diffraction (XRD), Fourier Transfer (FTIR) spectroscopy, nitrogen physisorption and scanning electron microscopy, (SEM).

3.1. Thermogravimetric Analysis (TGA):-

TGA, of the dried hydrolysis product, Ceria-N120, in a flow of nitrogen gas and air is shown in Figure 3.1. Weight loss amounts of 12.43 and 12.27% respectively were recorded upon heating from room temperature (rt) to 900°C. The TGA thermogram carried out in a flow of nitrogen gas, Figure 3.1, exhibits three general TGA peaks in the indicated heating range, corresponding to the presence of three main weight loss regions. The first region, rt–190°C has a maximum at 72°C; the second region, 190–660°C shows a broad peak which has a maximum at 245 and 371°C. The third weight loss region appears above 600°C and maximizes at 694°C. Table 3.1 gives values of percentage weight loss corresponding to each step in each region. In the air flow, three TGA peaks were also observed. However, the region limits were shifted toward lower temperatures, as shown in Table 3.1. However, the peaks are more resolved for this analysis with maxima at 73, 221 and 755°C respectively.

Inspection of the two curves with different gradients obtained for the Ceria-N120 material in a flow of nitrogen gas and air shows that in spite of the continuous weight loss observed over all over the entire heating range, a stable weight loss region within the temperature range 600–700°C was observed. The main difference produced by the atmosphere appears in the second weight loss region, >150- ~ 600°C, where a faster weight loss in the flow of air than in flow of nitrogen gas was observed. However, the two curves are superimposed near 700°C.

TGA curves for the dried hydrolysis product, Ceria-B120, in a flow of nitrogen gas and air are shown in Figure 3.2. Weight losses of 12.80% and 12.24% respectively in nitrogen and air were observed. Three DTG peaks at 71, 239 and 722°C in nitrogen, and at 72, 221 and 733°C were observed (see Table 3.1 for further details). Comparison between the two curves obtained for the Ceria-B120 material in flows of nitrogen and air

generally showed similar features to the case of Ceria-N120. However, the profile of the second TGA peak in nitrogen and in the air flow are much more analogous indicating a lesser dependence on the flow in air in the case of Ceria-B120.

Therefore, the TGA results for Ceria-N120 and Ceria-B120 can be discussed as follows. Through the first weight loss region, desorption of physically adsorbed water and/or organic solvent occurs. The second weight loss region may be assigned to the decomposition and/or combustion of residual organic species (see FTIR results below), which is more pronounced for Ceria-N120 than for Ceria-B120. The small percent weight loss observed in the third weight loss region, (1.01 or 0.54%) for Ceria-N120 and (0.54 or 0.74%) for Ceria-B120 respectively, may be due to decomposition of some residual adsorbed species and/or oxygen loss at high temperature.

3.2. X-ray powder diffraction:-

XRD patterns for the dried hydrolysis products are shown in Figure 3.3. The peaks are very broad with low intensity and have a low signal/noise ratio. However, the main peak positions closely match those reported for ceria [JCPDS card No. 43-1002]. Figure 3.4 shows X-ray diffraction patterns for the 650°C calcined materials. In this case well-defined peaks of better signal/noise ratio are observed with very accurate matching. It should also be stated here that no other phases were detected in any of the examined materials.

3.3. Fourier Transform infrared (FTIR) spectroscopy:-

Figure 3.5 shows the FTIR spectra of Ceria-N120 (uncalcined) and Ceria-N650 (calcined), respectively. The spectrum for Ceria-N120 shows a group of strong intense bands at 3423 cm^{-1}, 1546 cm^{-1} and in the region, 1354-1382 cm^{-1}. The spectrum also

shows two other groups of peaks of lower intensity; one group at 2974, 2921 and 2863 cm^{-1} and the other group with peaks at 1054, 944 and 851 cm^{-1}. In light of the proposed assignments of such peaks in other similar systems[9,10,11] the observed bands can be assigned as follows: the band at 3423 cm^{-1} corresponds to the ν(O–H) mode of (H-bonded) water molecules. The group of weaker peaks at 2974, 2921 and 2863 cm^{-1} are assigned to the ν(C–H) mode of organic moieties. The low intensity of this group of peaks indicates the low content of organic material in Ceria-N120. The strong broad peak centred at 1546 cm^{-1} may be due to the $\nu_{as}(COO^-)$ and $\nu_a(COO^-)$ modes, which normally appear at 1546 and 1450 cm^{-1}. However, the unresolved nature of these two peaks suggests that they are not the only components of the broad peak, centred at 1546 cm^{-1}, as explained later. The strong broad peak, centred between 1354 and 1382 cm^{-1} may be partially assigned to the $\delta(CH_3)$ mode of the residual organic moieties. But, since the peak intensities observed for the stretching mode of CH_3 groups are very weak, as indicated above, another component must be contributing to this strong peak, as mentioned below. The weak peak at 1054 cm^{-1} may be assigned to the stretching mode, ν(C–O) of the OPr^i group. A similar assignment was made previously by Maggio *et al.*, [11] for C-O of OBu^n in a Ce-Zr dried gel. The broad band below 700 cm^{-1} is due to the envelope of the phonon band of the metal oxide network.

The spectrum for Ceria-N650, Figure 3.5, shows a group of peaks closely related to those observed for its parent material. As reported previously by Lyons *et al.* [12], on calcination, there is a dramatic decrease in the intensity of the typical broad features of the uncalcined species. The 3427 and 1632 cm^{-1} peaks are assigned to the ν(O–H) mode of (H-bonded) water molecules, and δ(OH), respectively. The latter band is not resolved in the spectrum of Ceria-N120, probably due to its overlap with the other bands that gives

rise to the broad nature of the 1546 cm^{-1} peak. Two other well-resolved peaks are observed however for the Ceria-N650 spectrum at 1440 and 877 cm^{-1}.

However, in the presence of the 877 cm^{-1} peak along with the suggested additional components of the 1546 and 1382-1354 peaks assigned for Ceria-N120; or the sharp peaks at 1440 and 877 for Ceria-N650, there is clear evidence of the presence of carbonate in the spectrum. In previous work[13] *Binet et al.* have reported the presence of adsorbed species from CO_2 adsorption on unreduced ceria at room temperature, including hydrogen carbonates and carbonates. In general, bidentate carbonates are the most well characterised species, with $\nu(CO_3)$ having been previously reported at 1567, 1289 and 1014 cm^{-1} respectively and $\pi(CO_3)$ at 856 cm^{-1}. Other modes of coordination of carbonate are also possible on the surface of ceria, including a bridging carbonate, a monodentate carbonate and a polydentate carbonate (all C_{2v} symmetry). The bands due to bridging carbonates are usually very weak in intensity ($\nu(CO_3)$ = 1736 and 1135 cm^{-1}), with no peak observed due to $\pi(CO_3)$. In contrast, the IR spectra of monodentate carbonates on the surface of ceria usually only show clear evidence of the high wavenumber band, $\nu(CO_3)$ at 1504 cm^{-1} (the other peak at 1351 cm^{-1} is of low intensity), and no peak due to $\pi(CO_3)$, similar to the case of the bridging carbonate species. The other coordination mode of carbonate on ceria is the polydentate carbonate. In such a species, the wavenumbers are very close to those reported for bands due to anhydrous cerium carbonate[14]. In addition, when only small amounts of polydentate carbonates remain on the surface of ceria, several bands centred between 1395 and 1350 cm^{-1} may be found on the spectrum. The IR spectra of Figure 3.6 therefore suggest the presence of a bidentate carbonate at peaks 1547 and 1382 cm^{-1} in Ceria-B120 and 1632 and 1440 cm^{-1} in Ceria-B650. Lyons *et al.* [12] have also reported the infrared spectra of uncalcined ceria and calcined ceria in air at 573 K, and have reported similar peaks at 1550 and 1406 cm^{-1}

(uncalcined) and 1501 and 1384 cm^{-1} (calcined). The spectral features (both in terms of intensity and approximate wavenumber) shown in Figure 3.6 are very similar to those reported [12] in relation to the adsorbed bidentate carbonate.

Figure 3.6 shows the FTIR spectra of Ceria-B120 (uncalcined) and Ceria-B650 (calcined) respectively. In these spectra, the presence of bidentate carbonate is again suggested, with peaks at 1547 and 1354 cm^{-1} in the uncalcined species and 1632 and 1440 cm^{-1} in the calcined species. Similar to Figure 3.5, there is a noticeable decrease in the intensities upon calcination. However, once more, the relative intensities in relation to the carbonate peaks are similar to those shown in Figure 3.1, suggesting a similar mode of coordination of the carbonate on the surface. However, the 1440 cm^{-1} peak due to carbonate is much more pronounced for the Ceria-B650 than for Ceria-N650. It appears that the presence of carbonate has a direct impact on the surface area of the material, as described in the surface area analysis section below.

However, Figure 3.7 shows the FTIR spectra of the TGA analysis residue for Ceria-N120 after heating at a rate of 10°C min^{-1} from rt to 900°C (in flow of air and in flow of nitrogen at 40 ml min^{-1}). Figure 3.7 shows that the intensity is severely reduced, although the adsorbed carbonate species is still present, suggesting the origin of atmospheric carbon dioxide. However, it has been suggested previously that carbon dioxide is an inevitable adsorbent on ceria surfaces at rt and is indicative of high surface basicity of surface O^{2-} ions for ceria[13].

3.4. Nitrogen adsorption:-

The isotherms for nitrogen adsorption/desorption for the two calcined materials are shown in Figure 3.8. According to the original IUPAC classification[15], the isotherms are similar in behaviour to type II type isotherms with some contribution from type IV type

isotherms. The loops are relatively narrow especially for the Ceria-N120 material; the adsorption and desorption branches are almost vertical and parallel. The loops can therefore be classified as Type H1 hysteresis. Additionally, according to the recent classification for the adsorption isotherms [16], the isotherms are of mixed Type IIa and Type IVb isotherms.

The assigned classifications indicate monolayer-multilayer adsorption on an open and stable external surface of powder. The isotherms show delayed location for the adsorption branch, which is governed by the delayed nitrogen condensation process due to wide porosity. However, as the nitrogen condensation process occurs at relatively higher p/p_o for the Ceria-N650 material than that for the Ceria-B650 material, a wider pore size can be expected for the former.

Textural characteristics including surface area, S_{BET}, external surface area, S_t, micro pore area, S_{mic}, along with the average particle size for the test materials are cited in Table 3.2. The table indicates that the Ceria-B650 material has a higher surface area, S_{BET}, of 41.2 m^2/g compared to 33.1 m^2/g for the corresponding Ceria-N650 material. Moreover, a lower contribution of microporosity was found for Ceria-B650 (1.0 m^2/g out of 41.2 m^2/g total surface area) than for Ceria-N650 (5.5 m^2/g out of 33.1 m^2/g total surface area). Table 3.2 also compares the present results with some other reported ceria materials from the literature.

Figure 3.9 shows BET plots for the Ceria-N650 and Ceria-B650 Materials.

3.5. Scan Electron Microscopy:-

SEM micrographs for the Ceria-N120 and Ceria-B120 precursor materials are shown in Figure 3.10 a and b respectively. The general morphology of the precursor obtained in neutral media, Ceria-N120, showed a case of porous aggregates of submicron to micron

size. The aggregates are not uniform but they are composed of relatively equiaxed finer primary particles and show clear signs of porosity. However, the morphology of the precursor obtained in basic media, Ceria-B120, showed aggregates of smaller size, composed of highly cross-linked primary particles. Large fractions of the sample are present as free small clusters/and or primary particles.

SEM micrographs for the Ceria-N650 and Ceria-B650 precursor materials are shown in Figure 3.11 a and b respectively. Figure 3.11 a shows that Ceria-N650 is composed of many isolated desecrate particles and small size aggregates. This indicates a dramatic change in the material morphology (in comparison to its precursor, Ceria-N120). Such isolated desecrate particles and small size aggregates morphology reduces mesoporosity upon packing resulting in a lower total surface area.

However, for Ceria-B650, a larger number of primary aggregates consolidate with each other. Generally, the initial aggregates consolidate together at low coordination numbers giving rise to a more porous texture of higher surface area.

3.6. Conclusion:-

The above results show that the surface area and porosity of the sol-gel derived ceria materials are very satisfactory and suggest good thermal stability in terms of the preservation of surface area and porosity after calcinations for 3 h at 650 °C. In general, the sol-gel method has always been criticized on two aspects. First, the contamination with organics through processing has been a negating factor in this method. In addition, the easy sintering at high temperature in spite of the good surface area, which might have been obtained at low calcinations temperatures, has also been seen to be a disadvantage in the application of the method in this area. The present results (TGA and FTIR) have shown however that most of the organic impurities have been removed (and/or oxidized) relatively easily from the ceria surface probably due to the oxidizing nature of the ceria surface. Furthermore, the material processed in the neutral medium yields a good surface area of 33.1 m^2g^{-1} and a higher surface area of 41.2 $m^2g^{-1}$was obtained for the material processed in the basic media. This indicates that good textural properties can be obtained in neutral media, and this can be further improved by conducting the hydrolysis in the presence of high ammonium hydroxide concentration (ammonium hydroxide: alkoxy ratio, 20 : 1). It should be noted that the ammonium hydroxide ratio implemented in the present study is similar to that used by Stöber *et al.*[17] to produce spherical silica particles *via* hydrolysis of TEOS (this is not the case for ceria due to many reasons). Nevertheless, similar to the case of TEOS, it can be argued that high ammonium hydroxide concentration helps in the removal of the terminal alkoxy groups, increase surface hydroxylation, and protect the particle against fast sedimentation during the settling processes. The effect of ammonium hydroxide can be seen by comparing the micrographs of Ceria-N120 and Ceria-B120, Figure 3.9 a and b respectively, where isolated particles

and small aggregates are formed in the case of ammonium hydroxide. The presence of very many small particles for the material processed in the presence of ammonium hydroxide indicates that the nucleation and growth processes were largely affected. However, no trace of ammonia was observed from the FTIR spectra of the dried material Ceria-N120. It can be suggested that the ammonia probably oxidized on the surface of ceria and was removed in the early stages of the drying process. SEM micrographs indicated that both of the calcined materials are composed of porous aggregates, but to different degrees however. The virtue of this aggregated porous morphology can be helpful too in limiting particle growth within the initial aggregate border upon calcinations at high temperature. Finally, it can be argued that increasing surface hydroxylation of the particles (in the presence of ammonium hydroxide) can help them condensate together and stabilize particles against sintering at a lower temperature. For this reason, better stability was obtained for the material processed in basic than in neutral medium.

Table 3.1 TGA results of weight loss (WL %) recorded in each weight loss region and the position of the maxima for each precursor as measured in flow of nitrogen gas and air.

Precursor	Atmosphere	Region /°C	WL max/°C	WL %
Ceria-N120	N_2	rt – 190	72	95.7
		190 – 660	245, 371	88.6
		660 – 890	694	87.6
Ceria-N120	Air	rt – 150	73	96.5
		150 – 625	221	88.4
		665 – 890	755	87.7
Ceria-B120	N_2	rt – 165	71	95.8
		165 – 645	239	88.3
		645 – 890	722	87.2
Ceria-B120	Air	rt - 150	72	96.1
		150 – 640	222	88.5
		640 - 890	733	87.7

Table 3.2 Textural characteristics: surface area, S_{BET}, external surface area, S_t, and micropore area S_{mic}, pore diameters and particle size for the test materials calcined at 650°°C in air for 3 h.

Material	S_{BET} (m^2/g)	c_{BET}	S_t (m^2/g)	S_{mic} (m^2/g)	Pore diameter (nm)		particle size (nm)
					Average	BJH	
Ceria-N650	33.1	38.0	27.6	5.5	12.0	16.0	41
Ceria-B650	41.2	45.5	40.2	1.0	17.0	21.5	34
Ceria-700°C[a]	32.9	-	-	-	-	-	20.9
Ceria-650°C[b]	16.9	68.1	-	-	-	-	-

[a] *data from reference Lundberg et al*[7].

[b] *data from a sample made by calcinations of cerium oxalate for* 3 h *at* 650°C.

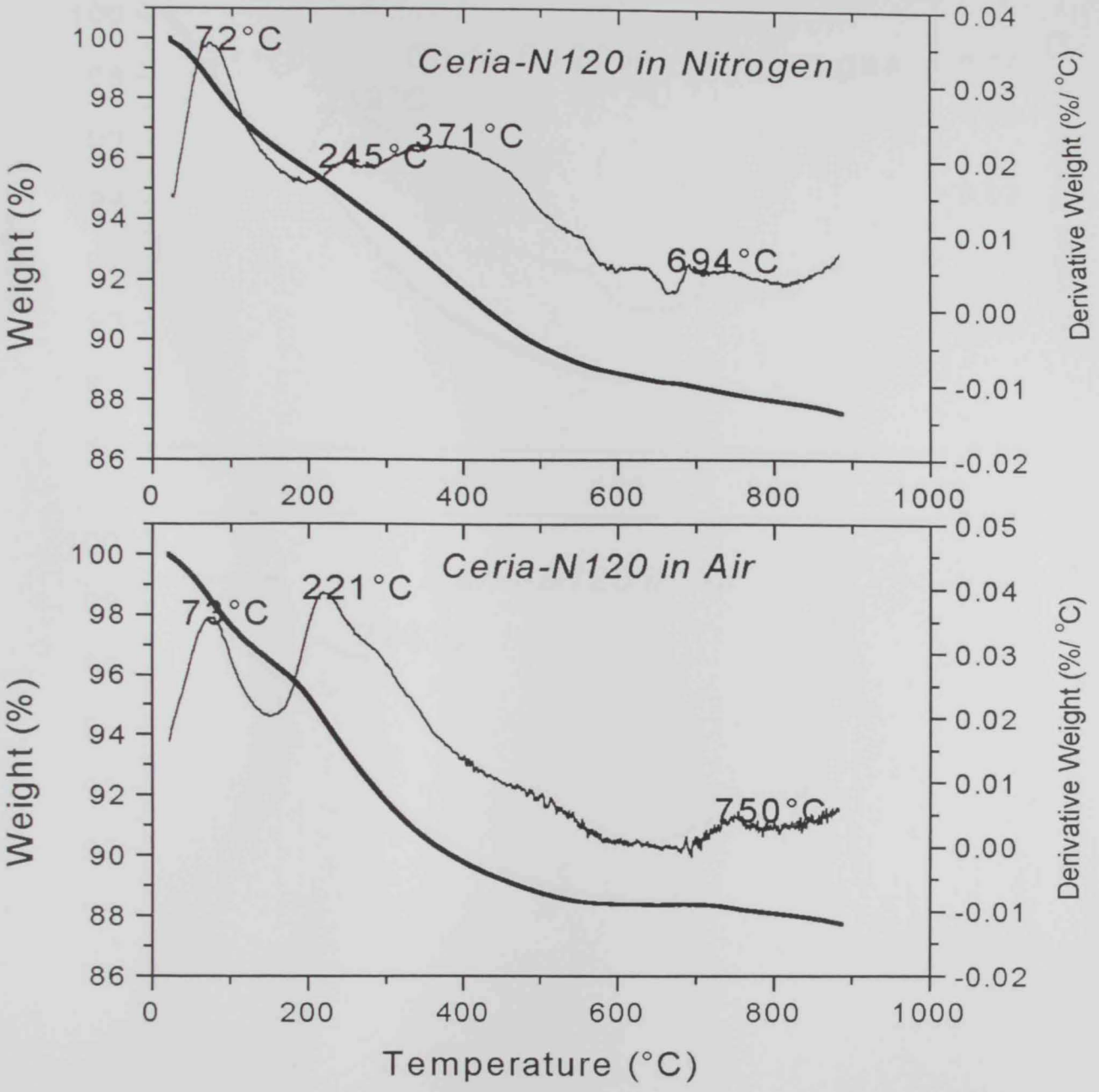

Figure 3.1 TGA and DTG curves of the CeriaN-120 material carried out in: (a) flow of nitrogen gas (top), and (b) flow of air (bottom).

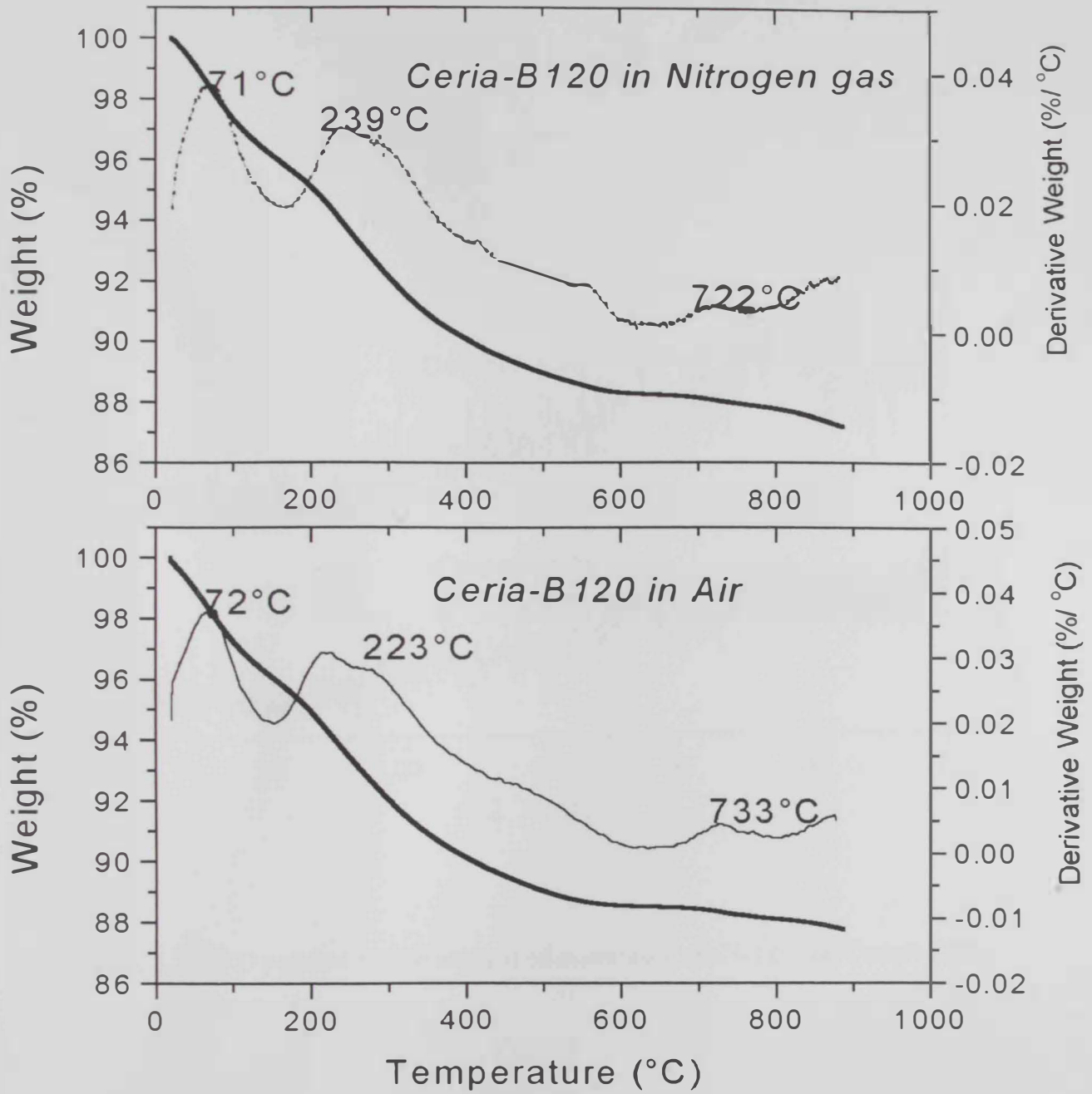

Figure 3.2 TGA and DTG curves of the CeriaB-120 material carried out in (a) flow of nitrogen gas (top), and (b) flow of air (bottom).

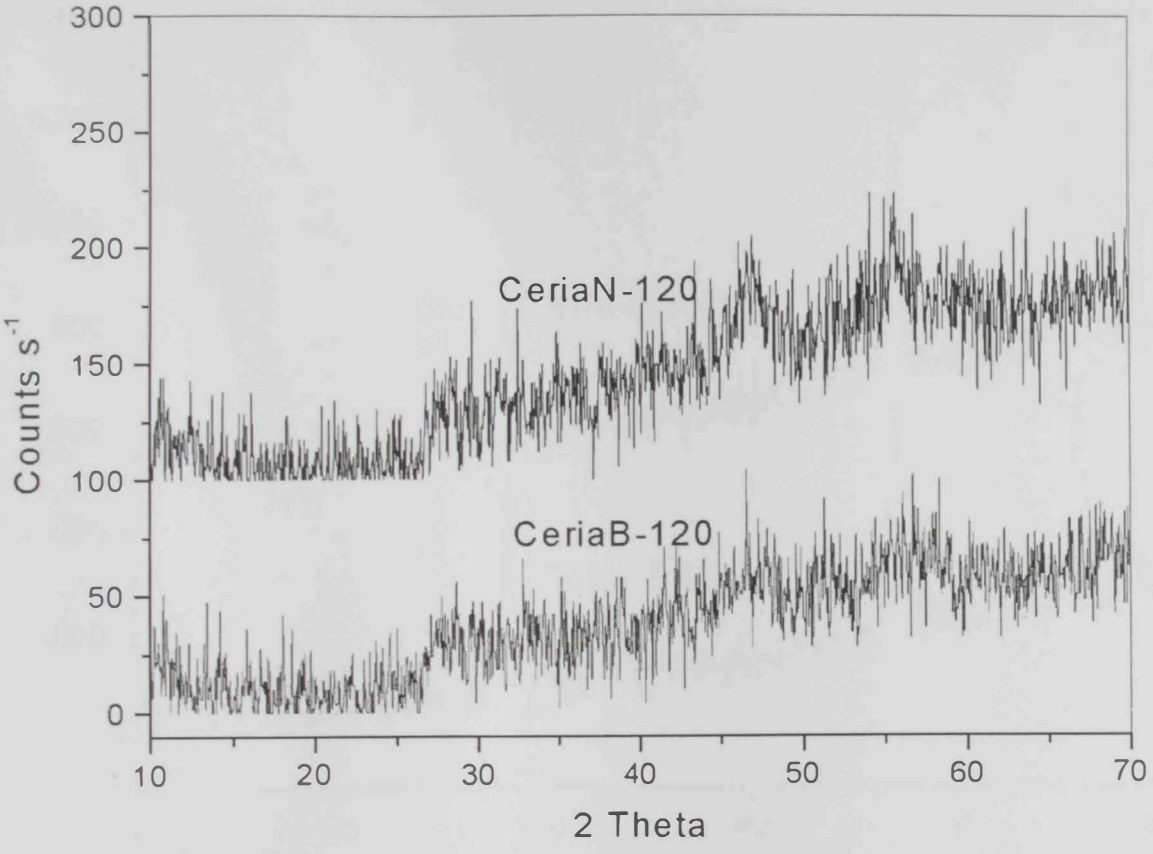

Figure 3.3 XRD patterns for the uncalcined materials CeriaN-120 and CeriaB-120.

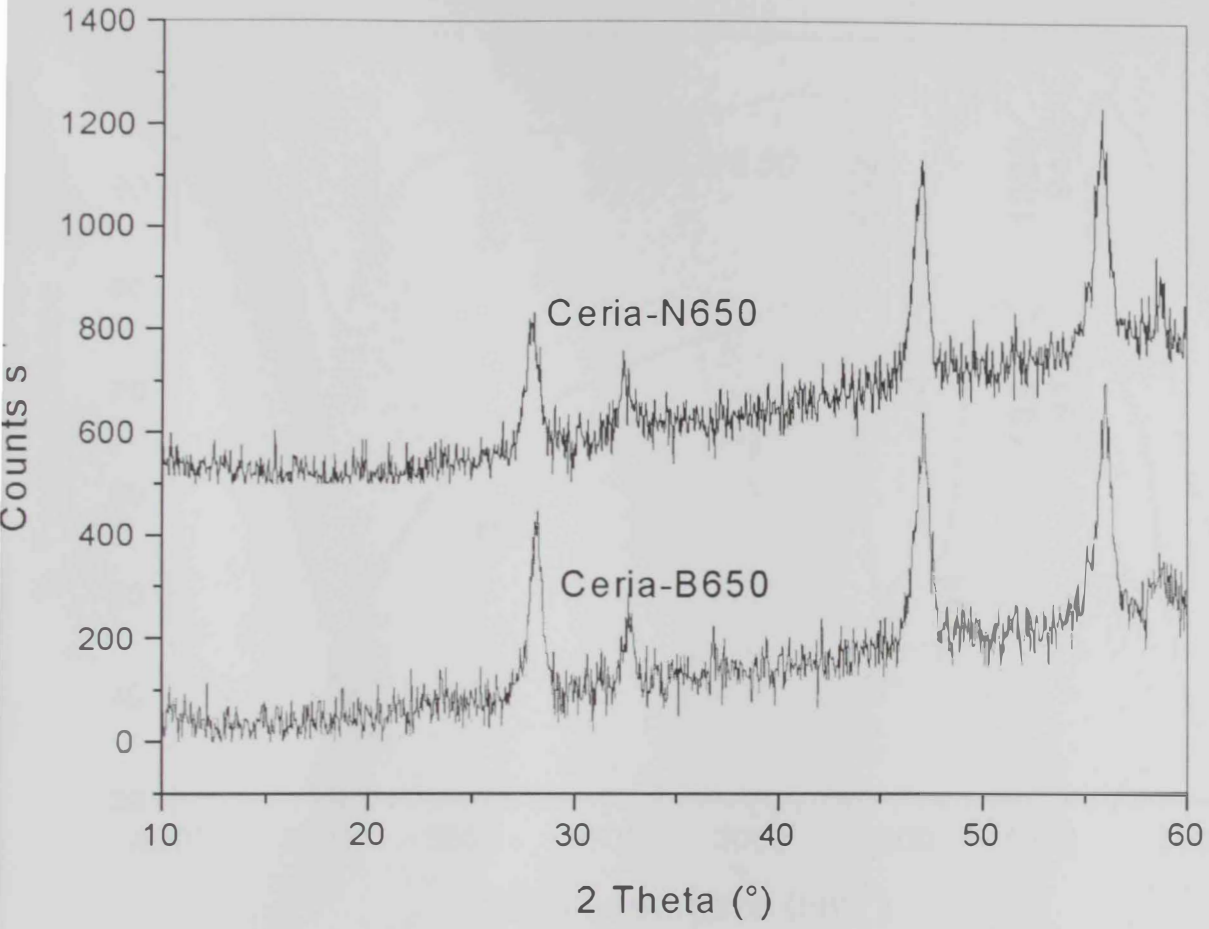

Figure 3.4 XRD patterns for the calcined CeriaN-650 and CeriaB-650 materials.

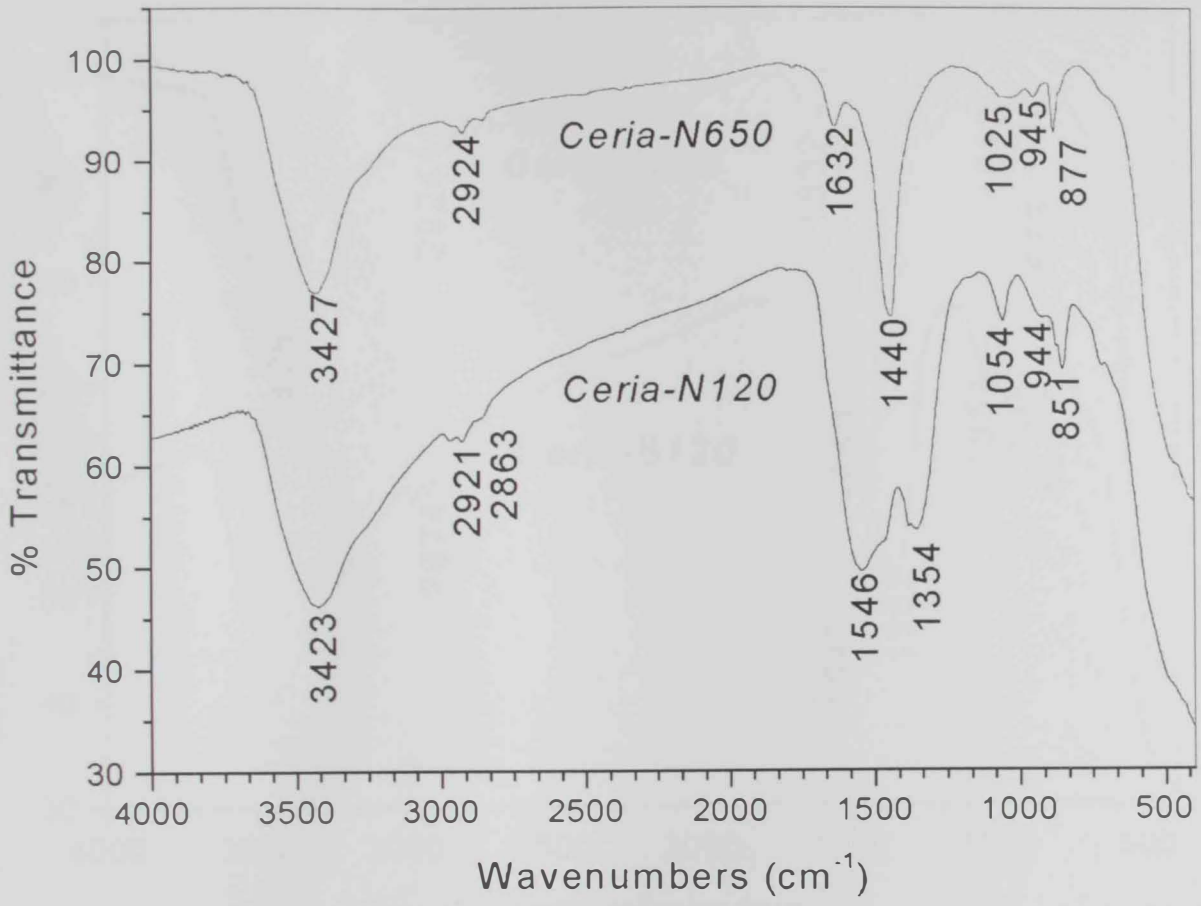

Figure 3.5 FTIR spectra for the CeriaN-120 and its calcination product CeriaN-650.

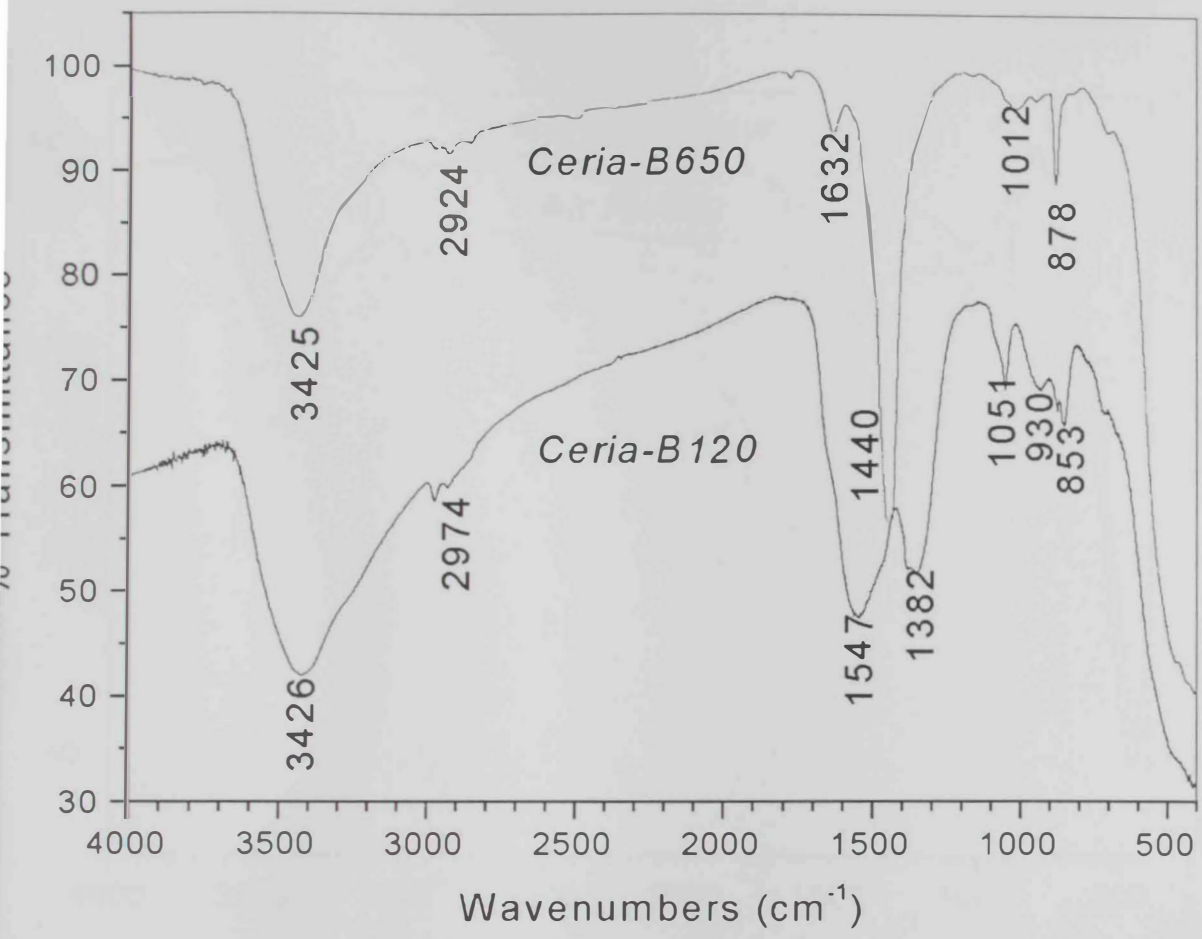

Figure 3.6 FTIR spectra for the CeriaB-120 and its calcination product CeriaB-650.

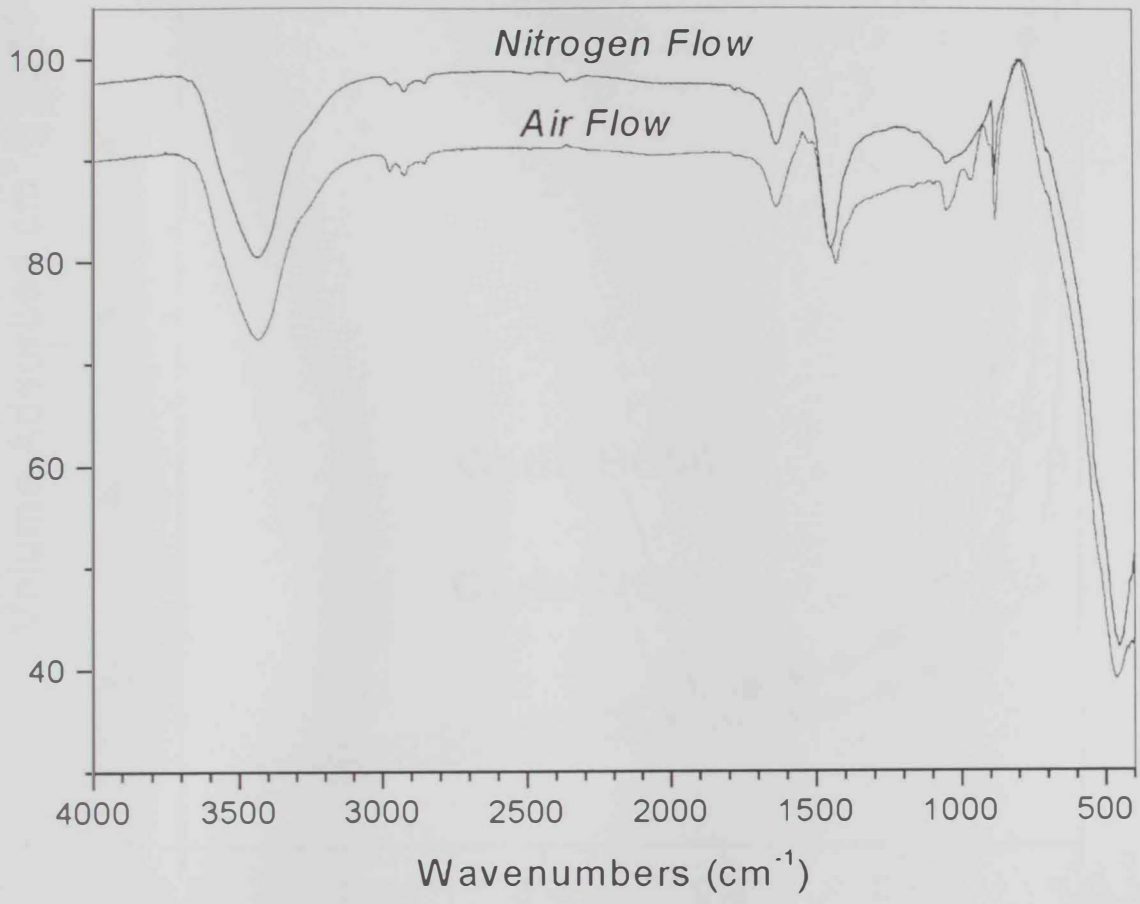

Figure 3.7 FTIR spectra for the residue left over from the Ceria-B120 material after TGA experiments in the range rt-900 °C in flow of nitrogen gas or air.

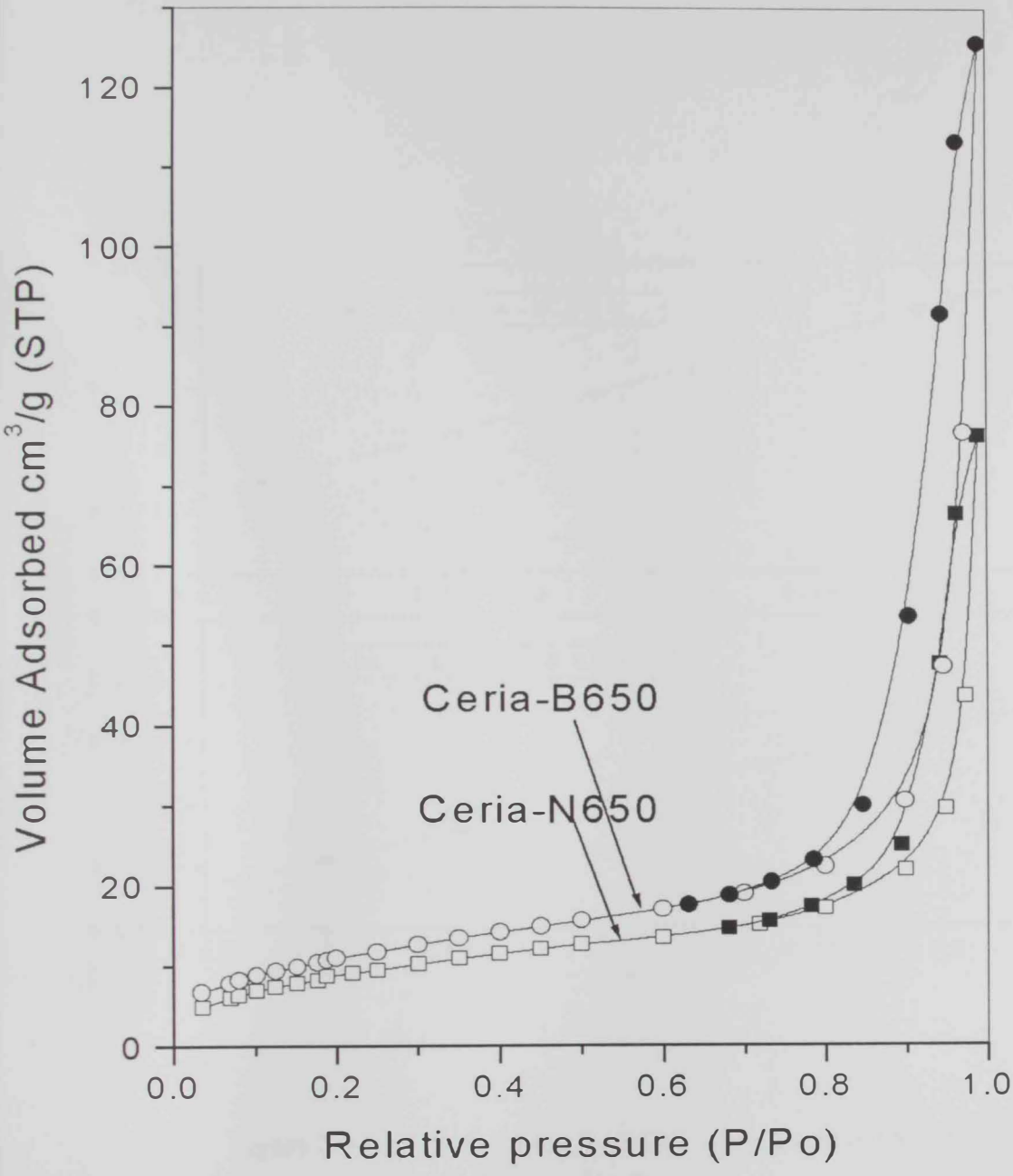

Figure 3.8 N_2 adsorption/desorption isotherms for the CeriaN-650 and CeriaB-650 materials.

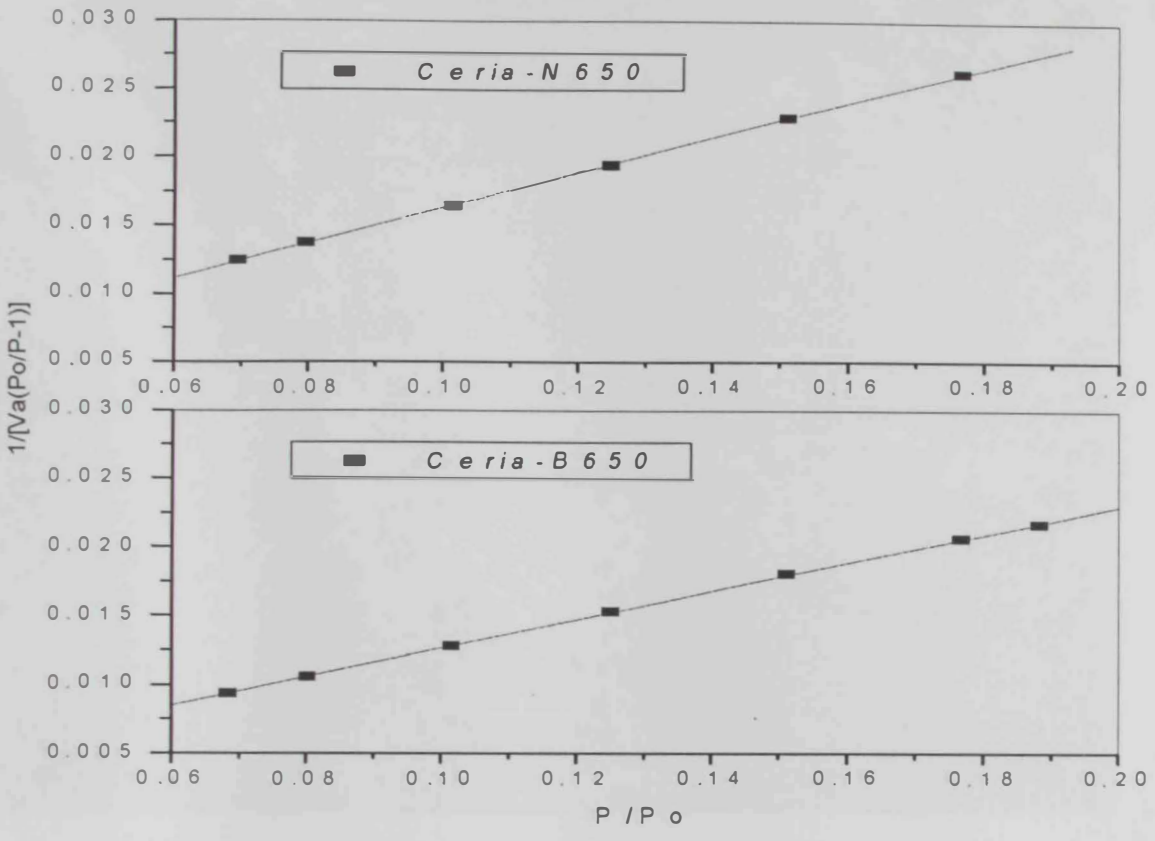

Figure 3.9 BET plots for the Ceria-N650 and Ceria B-650 Materials.

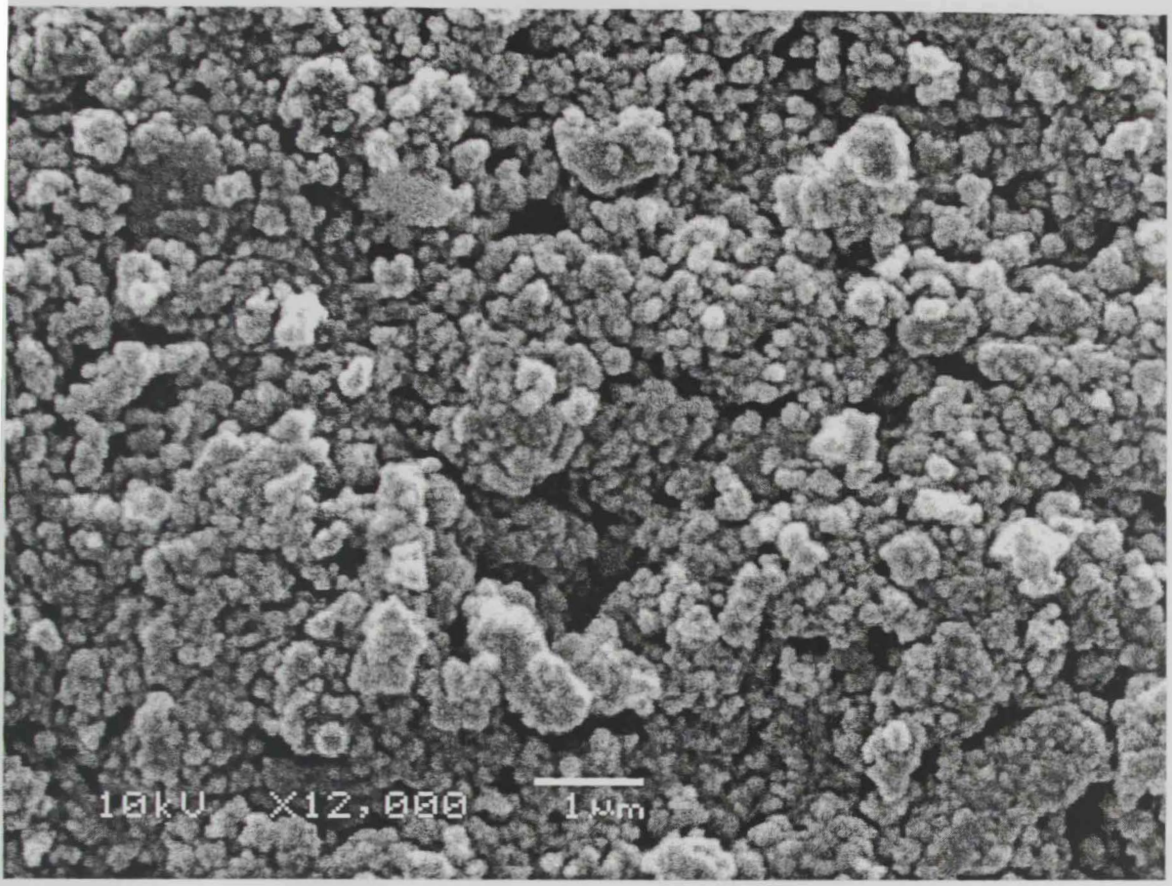

Figure 3.10(a) SEM micrograph for the uncalcined materials Ceria-N120.

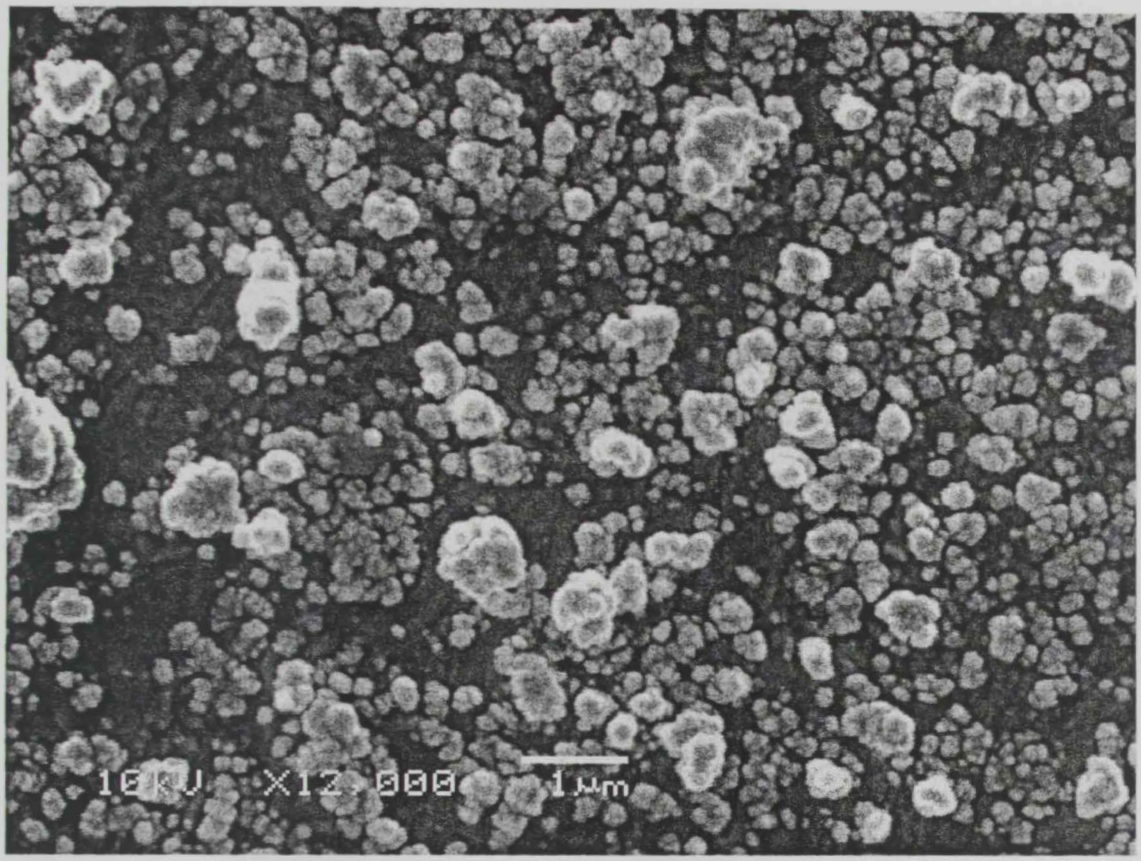

Figure 3.10(b) SEM micrograph for the uncalcined materials Ceria-B120.

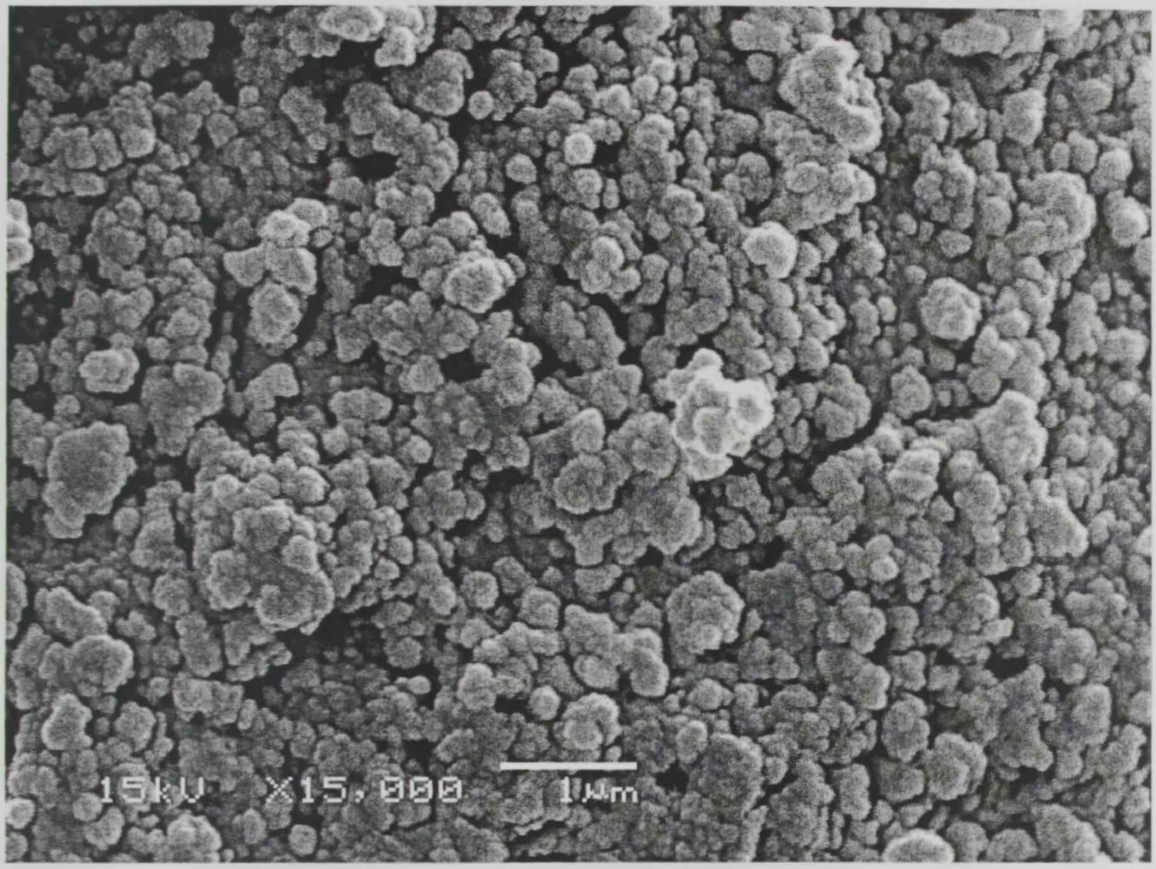

Figure 3.11 (a) SEM micrograph for the calcined materials Ceria-N650.

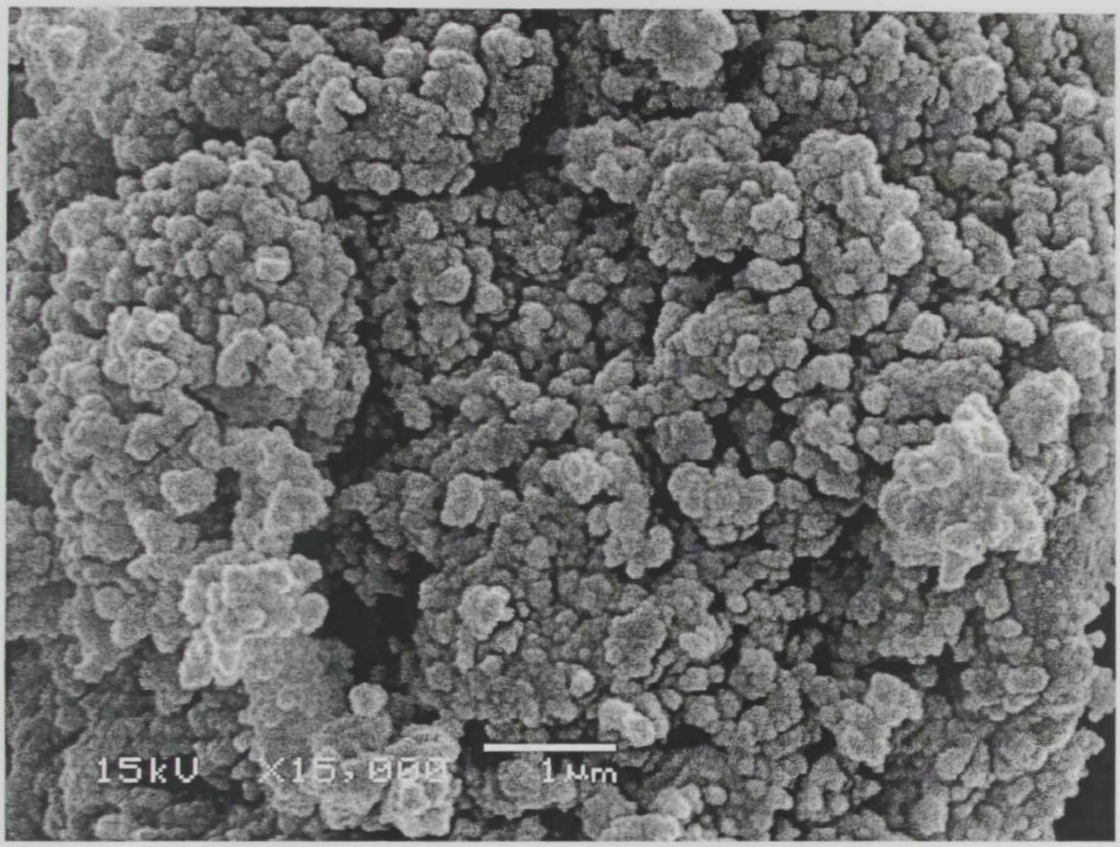

Figure 3.11(b) SEM micrograph for the calcined materials Ceria-B650.

Chapter 4

Textural morphology and thermal stability of ceria/silica composite materials formed via the interaction of silica sol with different ceria precursors

Chapter 4: Textural morphology and thermal stability of ceria/silica composite materials formed via the interaction of silica sol with different ceria precursors

The effect of the structural and textural aspects of ceria has been reported for many catalytic ceria systems[1,2] as explored in the introduction chapter. It has been found[3], that doping of ceria with silica or zirconia[3,4,5] induces important structural transformations which depend on the amount of dopant and on the thermal history of the samples. In addition, there is much evidence reported in the literature where the mixing of ceria with silica, or using silica as a support was found to improve the overall function of the catalyst *e.g.* SiO_2 is an effective surface-area-stabilizing agent for ceria[6,7]. However, despite the advantageous textural and morphological nature of ceria/silica composite materials their methods of preparation have not been fully explored as discussed in section 1.4.

The present work reports the preparation of ceria/silica materials by the mixing of a prehydrolyzed Ce(IV)-tetraisopropoxide (gel), or Ce(IV)-ammonium nitrate aqueous solution with freshly prepared Stöber silica sols. The aim of this work is to take the advantage of the highly dense phase (Stöber silica particles) as a matrix for ceria particles in order to produce thermally stabilized textural ceria/silica materials. The structural and textural characteristics of the dried materials (uncalcined), as well as the materials produced by calcinations for 3 h at 650°C (calcined), were explored by TGA, FTIR, XRD, SEM and N_2 adsorption techniques.

4.1. Thermogravimetric Analysis (TGA):-

TGA and DTG curves for the uncalcined hydrolysis product of pure SiO_2, in flow of an atmosphere of nitrogen are shown in Figure 4.1. Weight loss amounts of 10.61% was recorded upon heating the precursor from room temperature (rt) to 700°C. The DTG curve, Figure 4.1, exhibits four peaks indicating four weight loss steps. The first, which maximizes at 54°C with a shoulder at 137°C corresponds to a weight loss of 5.92%, and most probably involves the desorption of the adsorbed organic solvents and water molecules. The other DTG peaks are observed at 200, 310 and 452°C respectively, which may be attributed to the dehydroxylation of the silica surfaces. TGA for the dried basic hydrolysis product of TEOS in a flow of nitrogen gas has been previously investigated[8]. Accordingly, the weight loss in the atmosphere of nitrogen originates mainly from the desorption of physically adsorbed water (and/ or solvents) and surface dehydroxylation of the silica surfaces[8,9].

Figures 4.2 and 4.3 show the TGA and DTG curves for the uncalcined 10%Alk and 20%Alk CeO_2/SiO_2 materials. Weight losses amounts of 12.29% and 11.95% were recorded upon heating from room temperature (rt) to 700°C, respectively. The figures show that the weight loss is continuous with a general decreasing rate all over the entire heating range rt - 700°C for the two uncalcined materials. Therefore, no clear peaks are observed for the DTG curve; nevertheless a very weak maximum around 280°C can be observed in both cases. Comparing the curves obtained for the uncalcined materials 10%Alk and 20%Alk CeO_2/SiO_2 with those obtained for the uncalcined SiO_2 materials indicates that addition of CeO_2 from a prehydrolyzed gel (alkoxide precursor) to a SiO_2 sol leads to a small increase in the weight loss upon heating in the range rt – 700°C. This slight increase is most probably due to the inclusion or trapping of some more water and solvent molecules in the CeO_2 gel containing precursors. However, the DTG peaks

assigned for the evaporation (of water and/or solvent) and surface dehydroxylation processes for the pure uncalcined SiO_2 material were not observed for the CeO_2 gel containing precursors. This suggests that CeO_2 gel plays an important role in these processes.

Figures 4.4 and 4.5 show TGA and DTG curves for the uncalcined 10%Ing and 20%Ing CeO_2/SiO_2 materials. Weight loss amounts of 13.80% and 14.55% were recorded upon heating from room temperature (rt) to 700°C, respectively for the uncalcined 10%Ing and 20%Ing CeO_2/SiO_2 materials. The figures show that the weight loss for the 10%Ing and 20%Ing CeO_2/SiO_2 uncalcined materials is continuous and the general profile is largely similar to the profile observed for the pure uncalcined SiO_2. DTG curves, Figure 4.4 and 4.5, show that a DTG broad peak appears around 298°C for the uncalcined 10%Ing material. However, for the 20%Ing uncalcined material, two peaks appear at 199 and 268°C. These peaks may be due to the decomposition of the some species related to the inorganic precursor.

4.2. X-ray powder diffractometry:-

XRD patterns for the uncalcined CeO_2/SiO_2 materials are shown in Figure 4.6, along with the uncalcined silica precursor. The profiles are similar to that for silica. However, for 10%Alk and 20%Alk uncalined materials only a few broad peaks of high signal/noise ratio are observed at positions close to the characteristic strong lines for ceria (see below), which indicate a case of partial crystallization of the dispersed ceria. No similar peaks were observed for the uncalcined 10%Ing or 20%Ing materials, which is indicative of their amorphous nature.

XRD patterns for the calcined CeO_2/SiO_2 materials, along with the patterns for the pure SiO_2 material are shown in Figure 4.7. The XRD patterns for the calcined silica

material shows a typical pattern for amorphous silica. XRD patterns for the calcined 10%Alk and 20%Alk CeO_2/SiO_2 materials, Figure 4.7, are still dictated by the amorphous like profile of silica; however, few broad peaks of high noise/signal ratio are observed at positions very close to the characteristic strong lines for ceria at 28.55°, 47.47° and 56.33° respectively, corresponding to the *d-spacing* of 3.12 Å, 1.91 Å and 1.63 Å characteristic for the (111), (220) and (311) planes of the cerianite (ceria) structure *Fm3m* (225). In contrast, XRD patterns for the calcined 10%Ing and 20%Ing CeO_2/SiO_2 materials, Figure 4.7, reflect the amorphous nature of both materials. However, for the 20%Ing calcined material, very weak peaks with high noise/signal ratio scarcely can be detected at the characteristic positions for ceria *i.e.* close to 28.55°, 47.47° and 56.33° as indicated above. This result indicates that ceria is present in the case of very finally divided nano-sized particles.

4.3. Fourier transform infrared (FTIR) spectroscopy:-

Figure 4.8 shows the FTIR spectra for the uncalcined pure SiO_2 material, along with the other uncalcined Alk and Ing CeO_2/SiO_2 materials. The spectra for the uncalcined pure SiO_2 material, Figure 4.6, spectrum a, shows a group of bands which agree with band positions reported for SiO_2 prepared by complete hydrolysis of TEOS, *i.e.* silica gel[8,10]. Accordingly, the band at 3440 cm^{-1} corresponds to the ν(O–H) mode of (H-bonded) water molecules, the band at 1632 cm^{-1} corresponds to the δ(OH) groups, and the band at 951 cm^{-1} corresponds to ν(Si–OH). The bands at 1100 and 800 cm^{-1} correspond to ν_{as}(Si–O–Si) and ν_s(Si–O–Si) modes respectively, whereas the band observed at 470 cm^{-1} corresponds to the δ(Si–O–Si) mode. In addition, the weakly intense band at 1384 cm^{-1} may correspond to adsorbed ammonia species.

FTIR spectra for the 10%Alk and 20%Alk CeO_2/SiO_2 uncalcined materials are shown in Figure 4.6, spectra b and c. The spectra are similar to the spectrum obtained for pure SiO_2. No additional bands are observed. However, the very weak band observed at 1384 cm^{-1} for the uncalcined pure SiO_2 spectra is not observed for the 10%Alk and 20%Alk CeO_2/SiO_2 uncalcined materials. FTIR spectra for the 10%Ing and 20%Ing CeO_2/SiO_2 uncalcined materials are shown in Figure 4.8, spectra d and e. Again, the spectra resemble the spectrum of pure SiO_2 spectra. However, a strong band is observed at 1384 cm^{-1} for the 10%Ing and 20%Ing CeO_2/SiO_2 uncalcined materials, which was observed for the uncalcined pure SiO_2 spectra.

FTIR spectra for the calcined pure SiO_2, along with the other calcined CeO_2/SiO_2 composite materials are shown in Figure 4.9. Spectra show that after calcination at 650°C for 3 h, all of the previously observed peaks for the uncalcined parent materials appear at the same position but of weaker intensity. The weakly intense band observed at 1384 cm^{-1} disappeared. This suggests that calcinations produced surface dehydration and/or dehydroxylation as well as desorption of any other adsorbed species.

4.4. Nitrogen adsorption:-

Nitrogen adsorption/desorption isotherms for the 10%Alk and 20%Alk CeO_2/SiO_2 calcined materials along with the calcined pure SiO_2 are shown in Figure 4.10. According to the original IUPAC classification[11], the isotherm for the pure calcined silica material is rather similar in shape to type II type isotherms with a scarcely obvious narrow loop. The isotherms for the 10%Alk and 20%Alk materials show similar behavior to that observed for the pure silica materials. Nevertheless, the isotherms show an increase in the total pore volume adsorbed near $p/p_o = 1$, and the hysteresis loops are wider. The loops can be classified as H3 type hysteresis loops.

Corresponding isotherms for the 10%Ing and 20%Ing CeO_2/SiO_2 calcined materials are shown in Figure 4.11, along with the calcined pure SiO_2 material, which are plotted here again for comparative purposes. The isotherms for the 10%Ing and 20%Ing materials show a large increase in the total pore volume adsorbed near $p/p_o = 1$, and the hysteresis loops are much wider than the 10%Alk and 20%Alk materials. The isotherm can be classified as type II and with a clear contribution from a type IV type isotherm. The hysteresis loops can be classified as H3 type, with some properties of H1 type hysteresis loops. Additionally, according to the recent classification for the adsorption isotherms[12], the isotherms obtained with the pure silica, and with the 10%Alk and 20%Alk calcined materials are classified as type IIb isotherms, whereas, the isotherms obtained with the 10%Ing and 20%Ing calcined materials are classified as mixed Type IIb and Type IVa type isotherms.

Textural characteristics including surface area, S_{BET}, external surface area, S_t, micro pore area, S_{mic}, and pore width for the test materials are cited in Table 4.1. The results indicate that the 10%Alk and 20%Alk calcined materials scarcely show higher S_{BET} values of 11.3 and 12.7 m^2g^{-1}, respectively, compared to 10.0 m^2g^{-1} for the pure SiO_2 calcined material. In addition, lower contributions for microporosity are obtained for the 10%Alk and 20%Alk calcined materials (3.8, and 3.8 m^2g^{-1}, respectively) than for the pure calcined SiO_2 material (6.2 m^2g^{-1}). Consequently, this gives rise to a higher contribution for the external surface area, S_t, for the indicated materials than for the calcined SiO_2, see Table 4.1.

However, results for the 10%Ing and 20%Ing CeO_2/SiO_2 calcined materials clearly show higher surface areas, S_{BET}, of 38.3 and 50.4 m^2/g, respectively, compared to 10.0 m^2/g for the calcined SiO_2 material. Moreover, in spite of this large increase in the S_{BET}, lower S_{mic} values are obtained for the 10%Ing and 20%Ing materials (4.4, and 4.3 m^2g^{-1},

respectively) than for the calcined SiO_2 (6.2 m^2g^{-1}). This gives rise to a higher external surface area, S_t, values of 34.0 and 46.3 m^2g^{-1}, respectively for the 10%Ing and 20%Ing materials compared to 3.8 m^2g^{-1} for the calcined SiO_2 materials, see Table 4.1.

Figures 4.12 and 4.13 show the BET plots for the (10 and 20%) Alk and (10 and 20%) Ing ceria materials.

4.5. Scanning Electron Microscopy:-

SEM micrographs for the uncalcined materials are shown in Figure 4.14 a-d. The micrographs show the spherical silica particles matrix and the ceria dispersed phase, which appears as smaller irregular particles. The composite produced from the Alk precursor, specifically the 20%Alk uncalcined materials, show the ceria phase in the case of aggregation into a variable size aggregates and overall non-uniform dispersion within the silica matrix, see Figure 4.14 a and b. However, better dispersion in terms of smaller ceria particles within the matrix is observed for the materials produced from Ing precursor, see Figure 4.14. Once more, a better dispersion was found on the 10%Ing than the 20%Ing uncalcined material.

SEM micrographs for the calcined ceria/silica materials are shown in Figure 4.15 a-d. Large morphological differences are observed between the two groups of calcined materials. The Alk group of materials shows a case of sintering or glass like phase formation in a large domain, whereas the Ing group of materials shows a case of open aggregating morphology of less sintering and better porosity. Ceria particles of nano size dimensions are observable in micrographs of the latter group Figure 4.15 c and d. These observations are in agreement with the S_{BET} and porosity measurements, which indicates a low surface area of 11.30 and 12.78 m^2g^{-1} respectively for the 10% and 20%Alk materials and a high surface area of 38.3 and 50.5 m^2g^{-1} respectively for the 10% and 20%Ing

materials. Moreover, the SEM results show the exact morphology difference between the two groups of materials.

4.6.Conclusion:-

It can be concluded that addition of either type of ceria precursors to silica particles leads to the formation of composite materials of modified texture and microstructural details of lower microporosity and higher external surface area. However, the effect is much more pronounced for the 10%Ing and 20%Ing materials than for the 10%Alk and 20%Alk materials. This suggests that there are essential differences between the two cases that can be attributed to the interaction of Alk and the Ing precursors with silica sol during the method of preparation. For the Alk precursor, CeO_2 species were in gel form when it was added to the respective silica particles sol, since they had prehydrolysed by traces of water present in the isopropanol medium during the ultrasonic treatment step. In fact, gelling of the hydrolyzed $Ce(IV)(OPr^i)_4.(OPr^i)$ during the ultrasonic dispersion stage was influenced by the limited amount of water and the high electro-positivity of the Ce^{4+} ion. Therefore, there was little opportunity for the gel to re-disperse due to the highly basic conditions present in the mother liquor of the silica sol. The latter factor may lead to further condensation of the surface gel layers making them much more cross linked and consequently less available for dispersion. The SEM micrograph for the 10%Alk and 20%Alk CeO_2/SiO_2 uncalcined materials supports this argument. This explains the presence of the CeO_2 domain within the SiO_2 particles for the calcined materials, the formation of the crystalline ceria phase and why no significant increase in the surface area was observed.

In comparison, when cerium(IV) ammonium nitrate was used as the source for the CeO_2 phase, soluble Ce(IV) ions went through the process of hydrolysis, nucleation and growth in the mother liquor of the silica sol. Therefore, under highly basic conditions, the rate of nucleation is very rapid whereas, the growth is slow, in particular if the amount of CeO_2 is limited. Apparently, as indicated by the results obtained, the 10% or 20% (w/w)

CeO_2/SiO_2 satisfied the required conditions for a fast rate of nucleation and a corresponding slow growth rate. This correlates with the observation of finely dispersed ceria particles on the surface of the supporting silica particles as seen by the SEM micrographs. Consequently, the presence of such fine particles on the surface of silica particles increases their roughness and allows textural modification as reflected by a highly improved surface area and porosity. Furthermore, the presence of such ceria particles between silica particles prevents them from coalescence and helps producing thermally stabilized CeO_2/SiO_2 composite materials. These results show that ceria from an inorganic precursor may be dispersed very finely compared to that obtained from the corresponding prehydrolyzed alkoxide ceria precursor.

Table 4.1 Textural characteristics: surface area, S_{BET}, external surface area, S_t, and micropore area S_{mic}, pore diameters and particle size for the test materials calcined at 650 °C in air for 3h.

Material	S_{BET} (m^2g^{-1})	c_{BET}	S_t (m^2g^{-1})	S_{mic} (m^2g^{-1})	Pore diameter (nm)	
					Average	BJH
Pure Silica	10.01	74.74	3.84	6.17	5.83	11.49
10% Alk Ceria/Silica	11.3	52.08	7.53	3.79	9.5	12.85
20% Alk Ceria/Silica	12.72	28.78	8.96	3.76	11.8	14.03
10% CAN Ceria/Silica	38.34	88.67	33.97	4.36	12.76	15.16
20% CAN Ceria/Silica	50.54	78.44	46.28	4.25	14.64	16.60

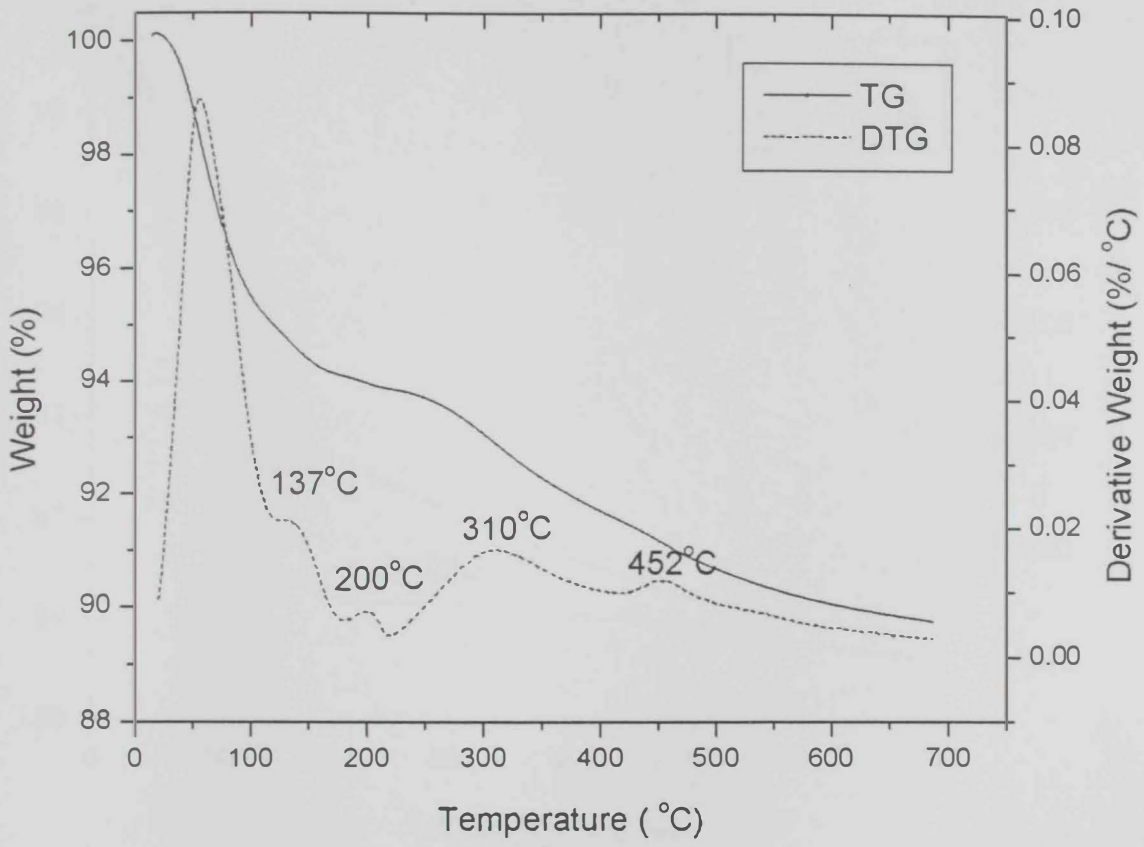

Figure 4.1 TGA and DTG curves for the uncalcined hydrolysis product of TEOS, pure SiO_2, in flow of an atmosphere of nitrogen.

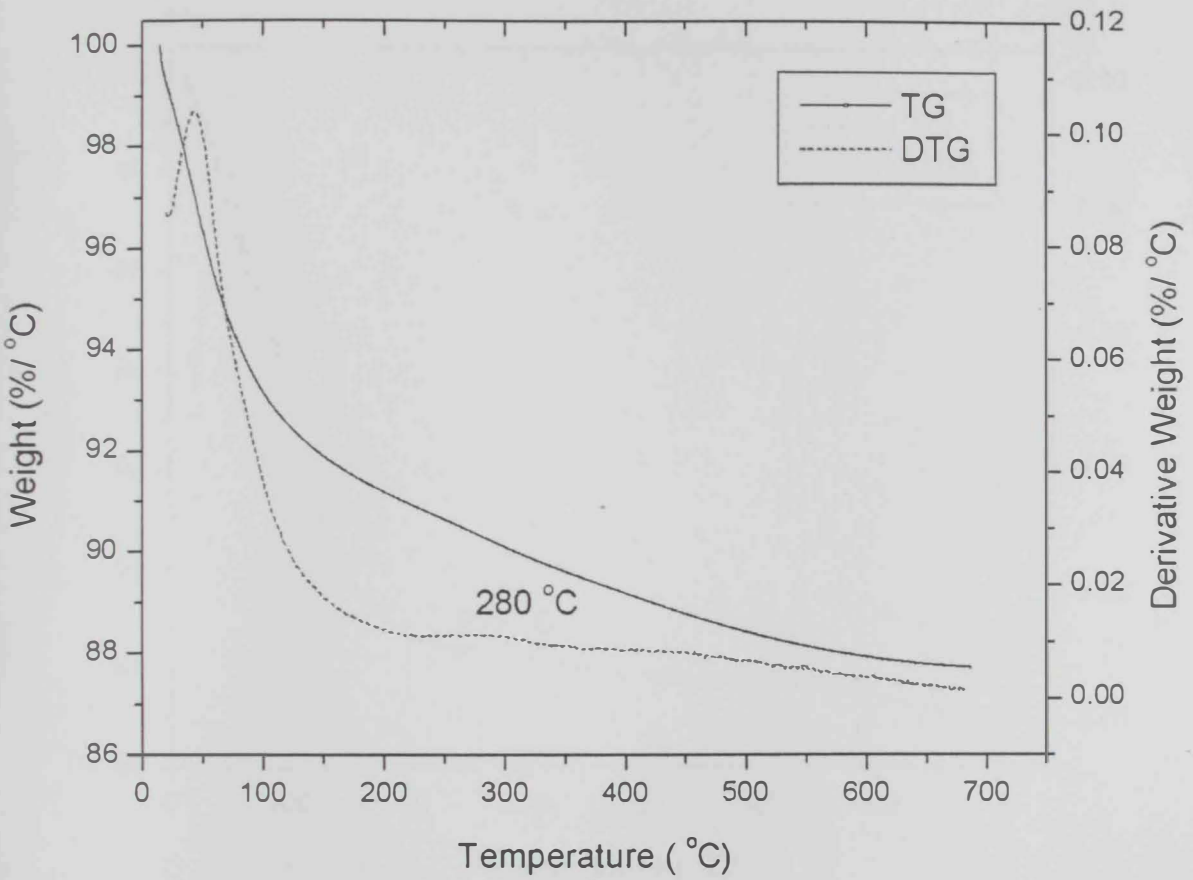

Figure 4.2 TGA and DTG curves for the uncalcined 10%Alk CeO_2/SiO_2 materials, in flow of an atmosphere of nitrogen.

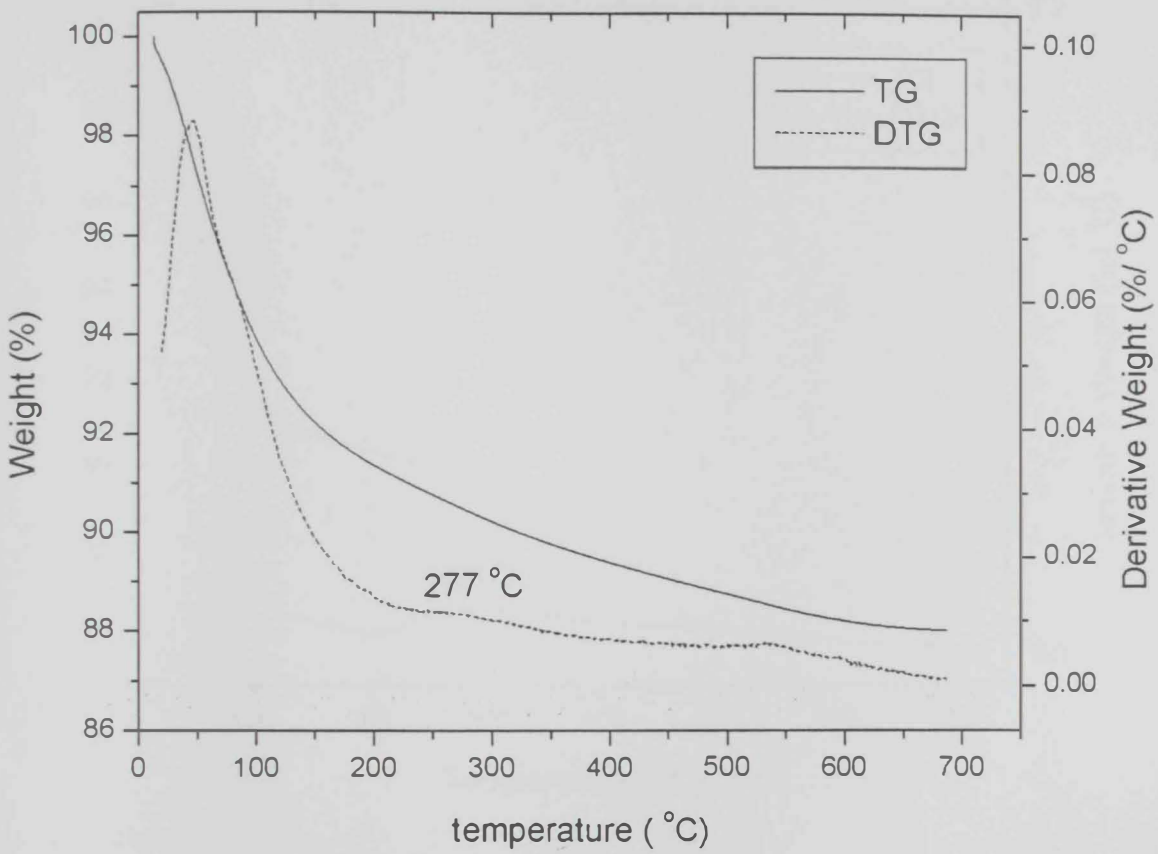

Figure 4.3 TGA and DTG for the uncalcined 20%Alk CeO_2/SiO_2 materials, in flow of an atmosphere of nitrogen.

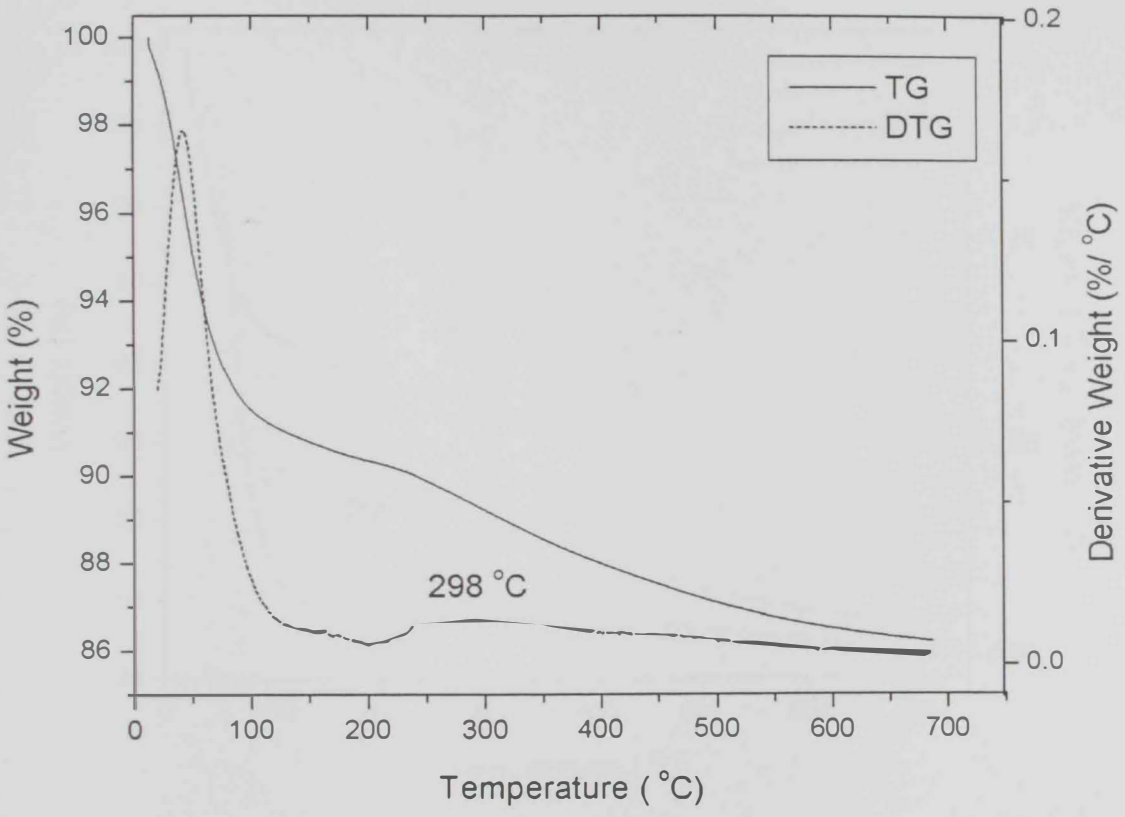

Figure 4.4 TGA and DTG curves for the uncalcined 10%Ing CeO_2/SiO_2 materials, in flow of an atmosphere of nitrogen.

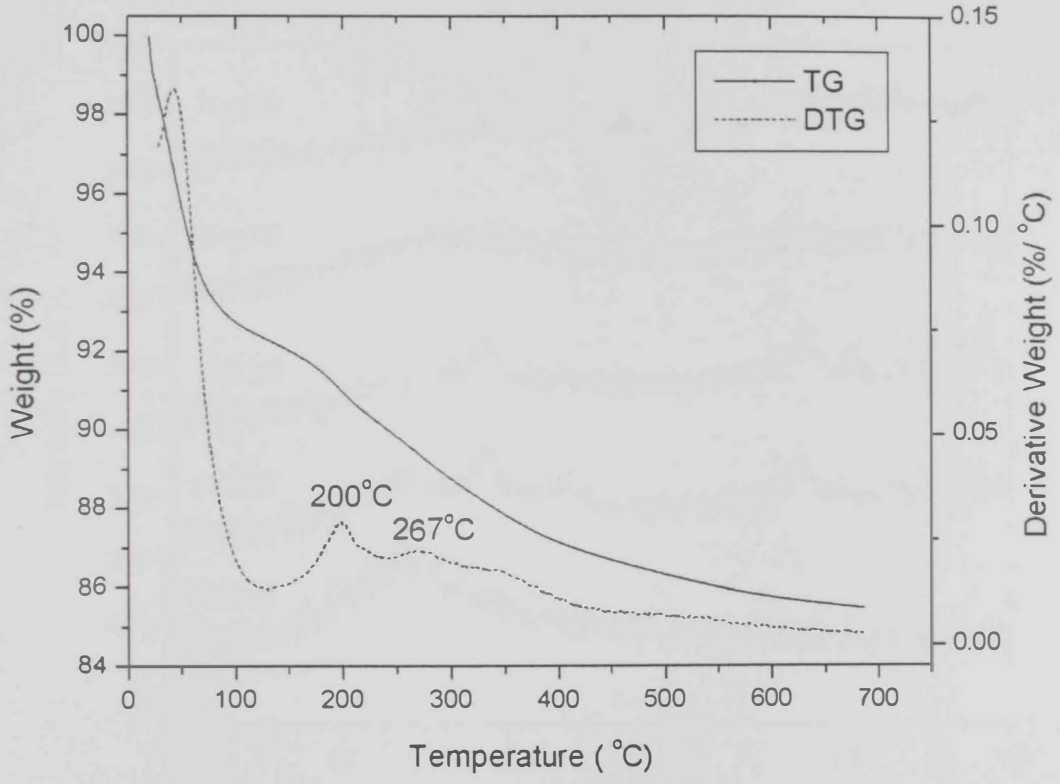

Figure 4.5 TGA and DTG for the uncalcined 20%Ing CeO_2/SiO_2 materials, in flow of an atmosphere of nitrogen.

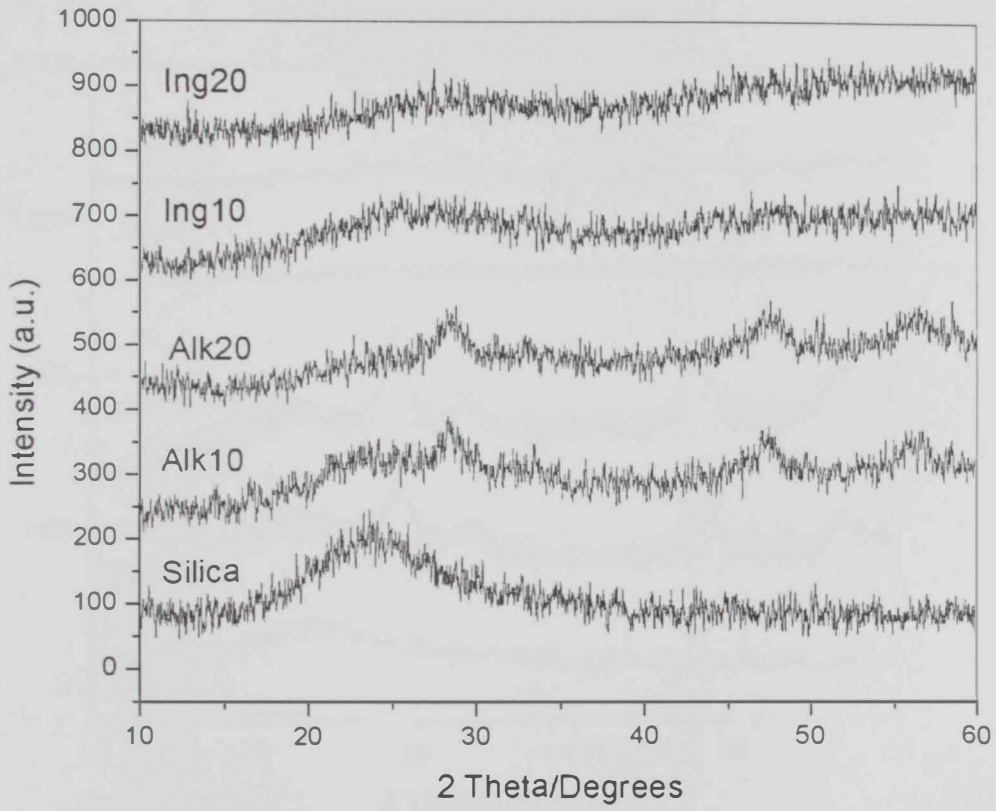

Figure 4.6 XRD patterns for the different uncalcined CeO_2/SiO_2 materials as indicated

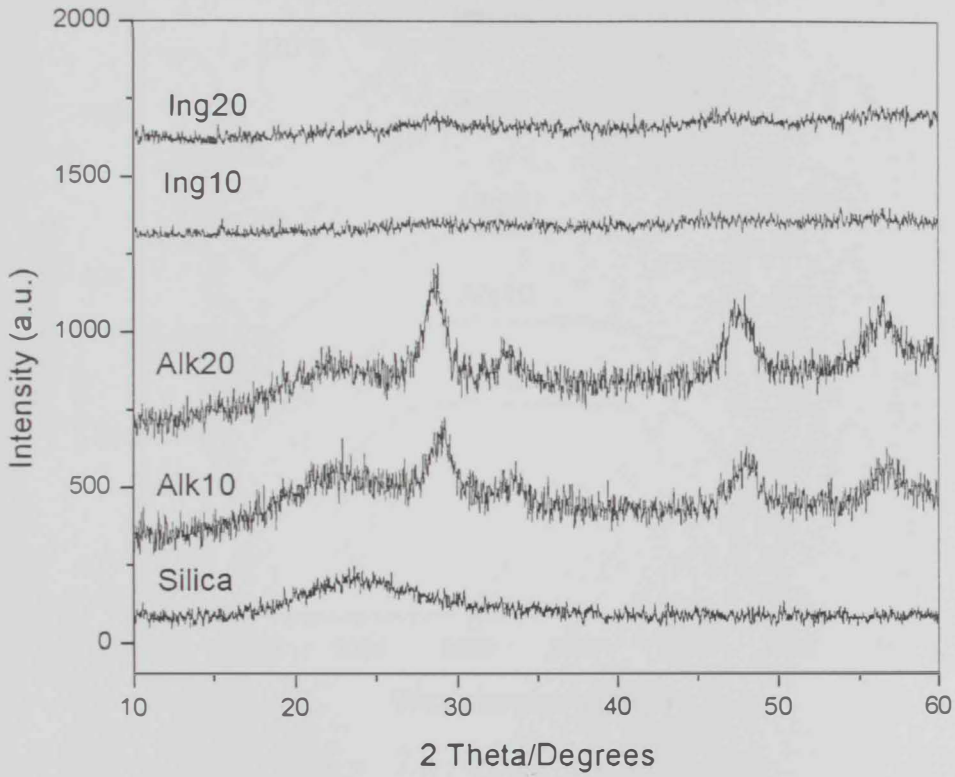

Figure 4.7 XRD patterns for the different calcined CeO_2/SiO_2 materials as indicated.

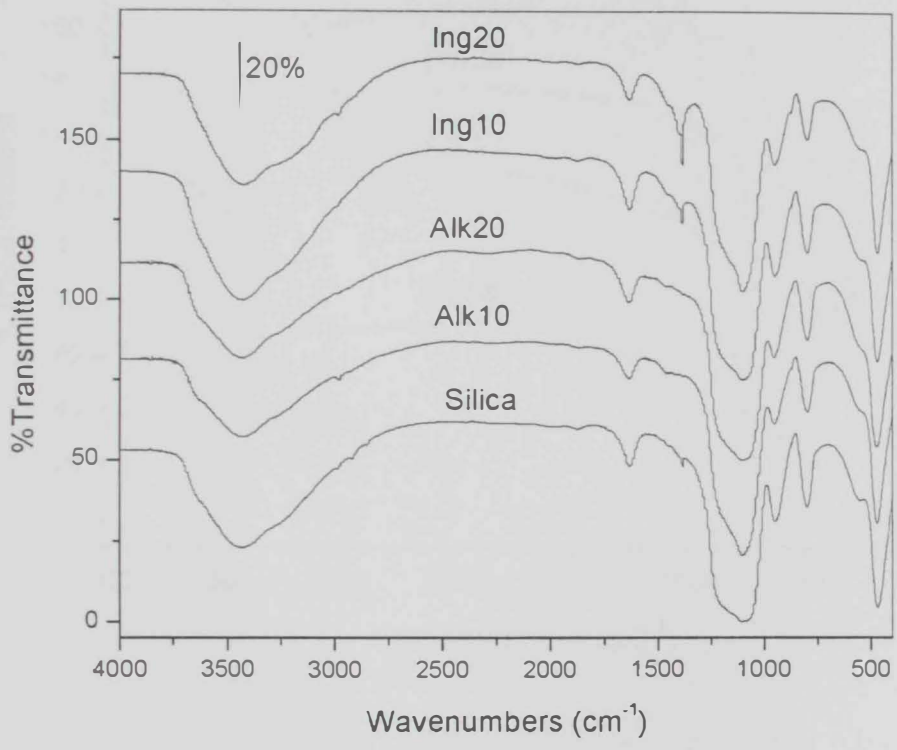

Figure 4.8 FTIR spectra for FTIR spectra for the uncalcined pure SiO_2 material, along with the other uncalcined 10%Alk, 20%Alk, 10%Ing, and 20%Ing CeO_2/SiO_2 materials as indicated.

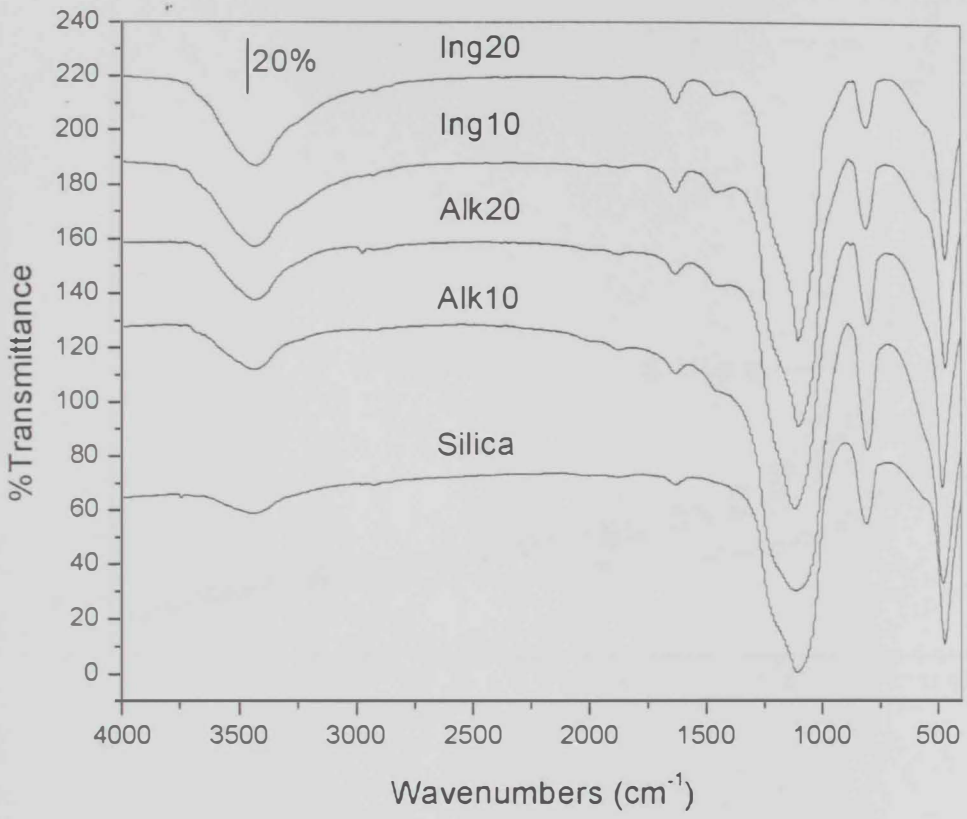

Figure 4.9 FTIR spectra for FTIR spectra for the calcined pure SiO_2 material, along with the other calcined 10%Alk, 20%Alk, 10%Ing, and 20%Ing CeO_2/SiO_2 materials as indicated.

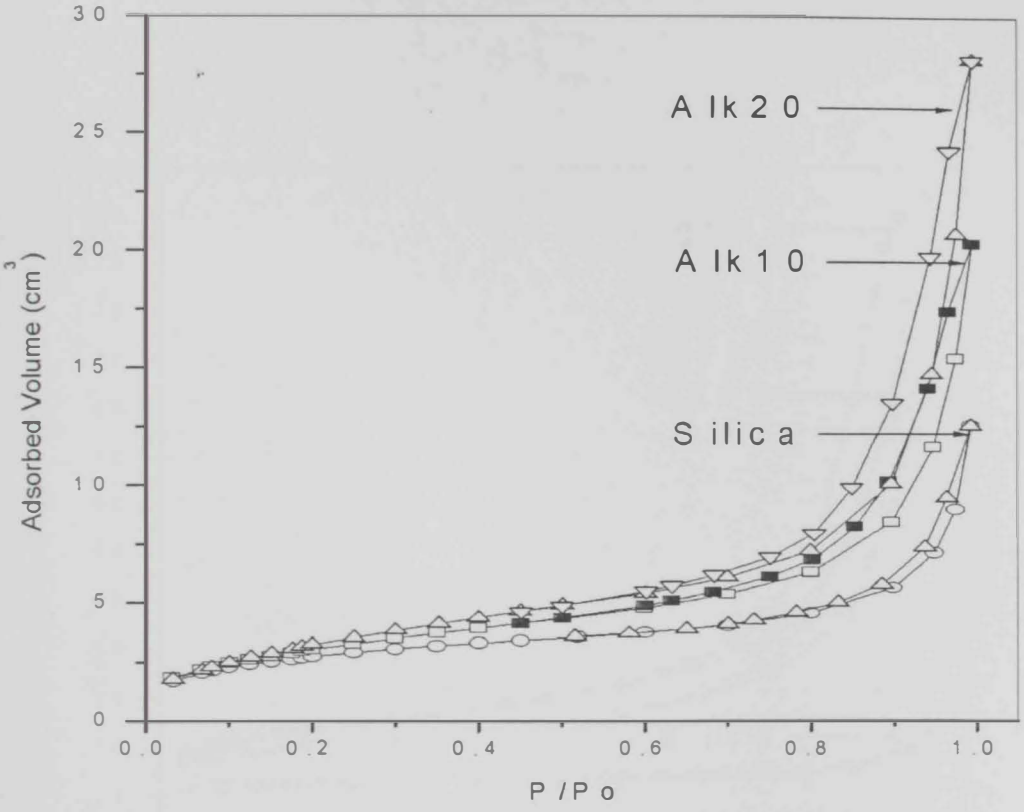

Figure 4.10 N_2 adsorption/desorption isotherms for the 10%Alk and 20%Alk CeO_2/SiO_2 calcined materials along with the calcined pure SiO_2.

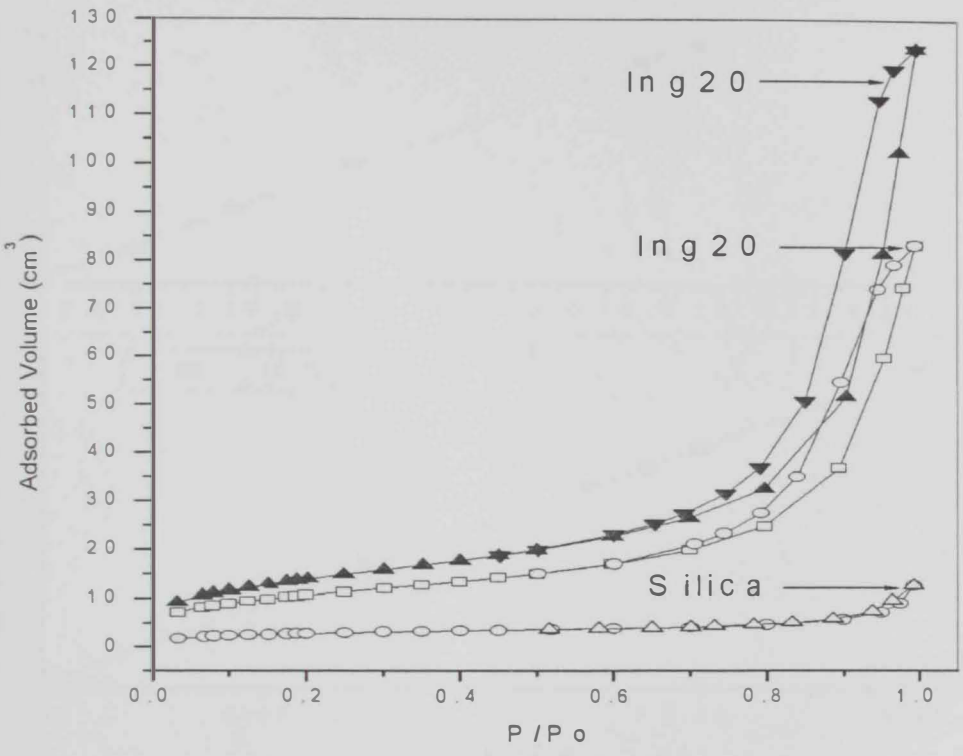

Figure 4.11 N_2 adsorption/desorption isotherms for the 10%Ing and 20%Ing CeO_2/SiO_2 calcined materials along with the calcined pure SiO_2.

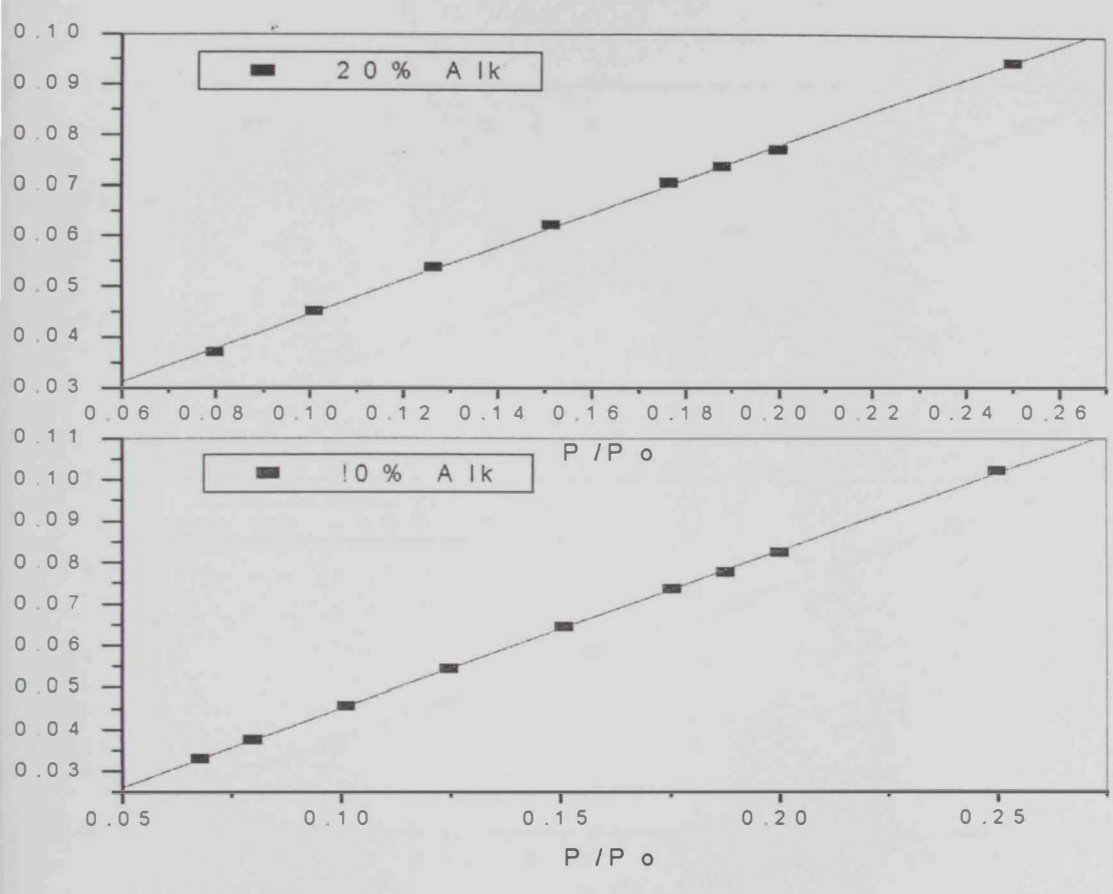

Figure 4.12: BET plots for the 10% Alk and 20% Alk Ceria Materials.

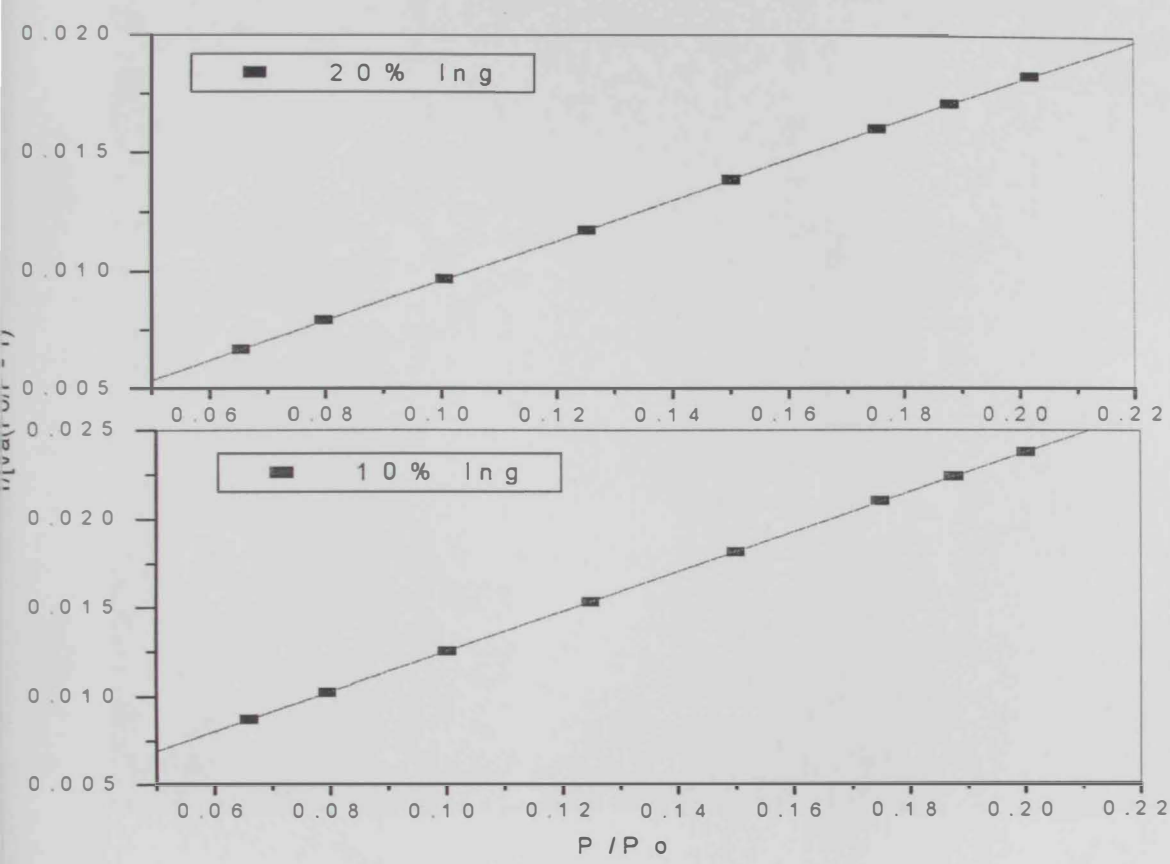

Figure 4.13: BET plots for the 10% Ing and 20% Ing Ceria Materials.

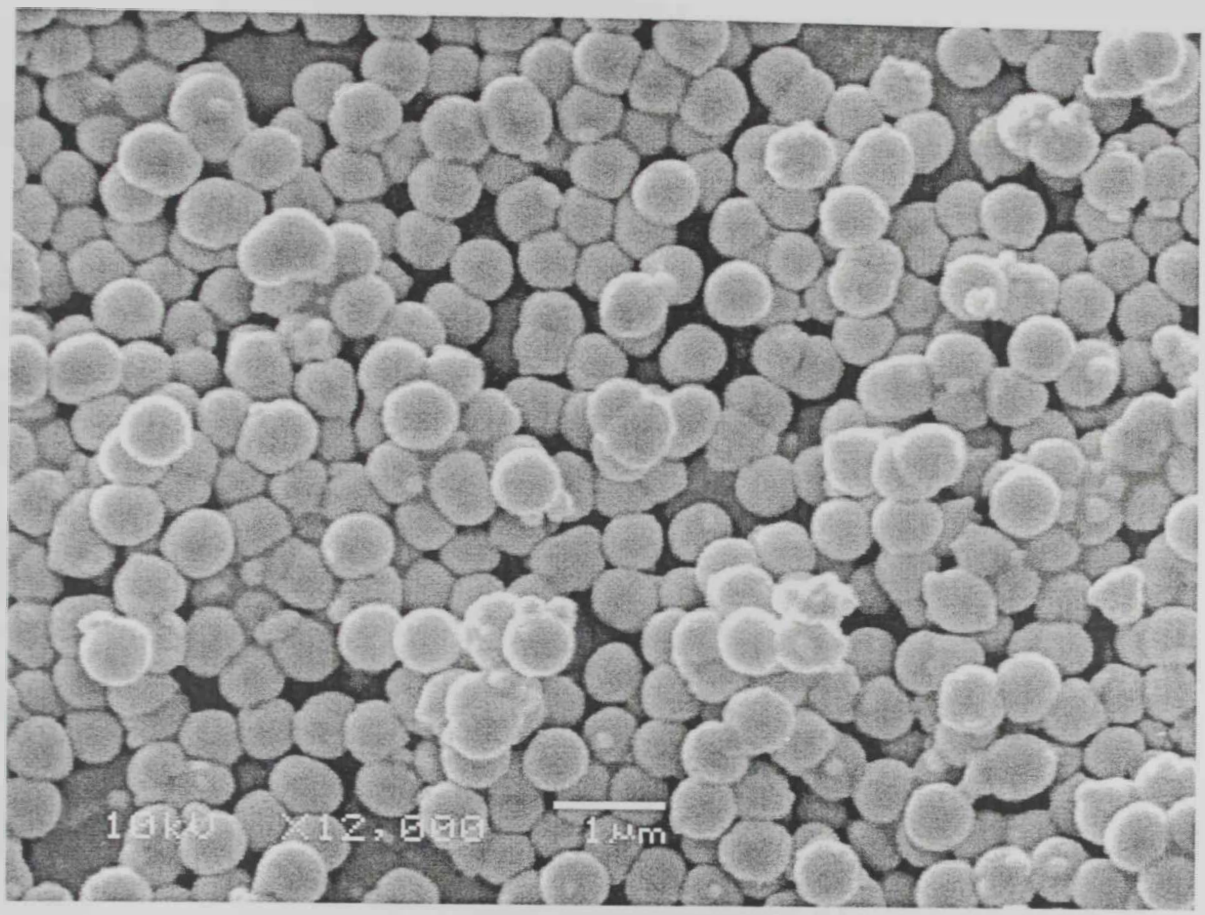

Figure 4.14 (a) Scanning electron micrographs of the uncalcined materials (a) 10%Alk, (b) 20%Alk (c) 10%Ing, and (d) 20%Ing.

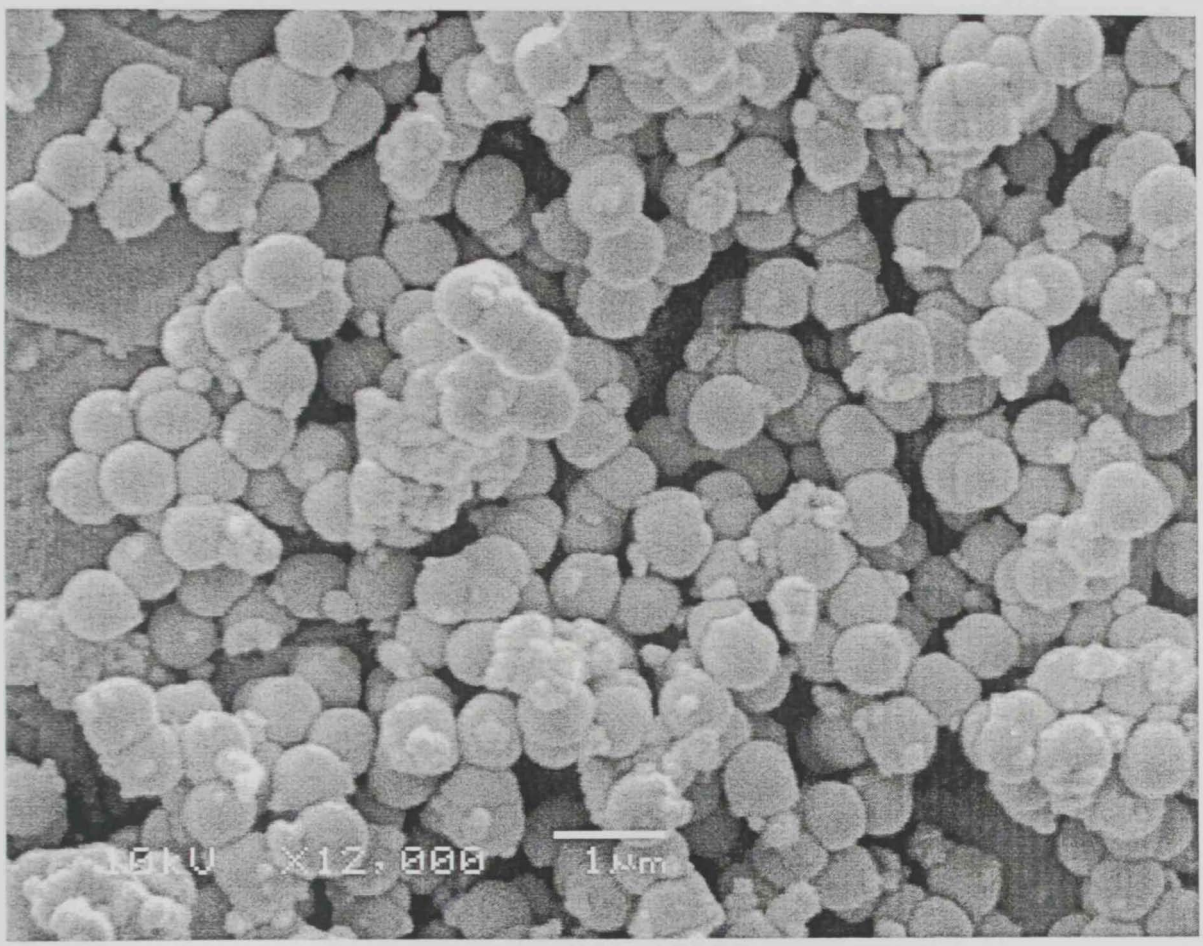

Figure 4.14 (b) Continued.

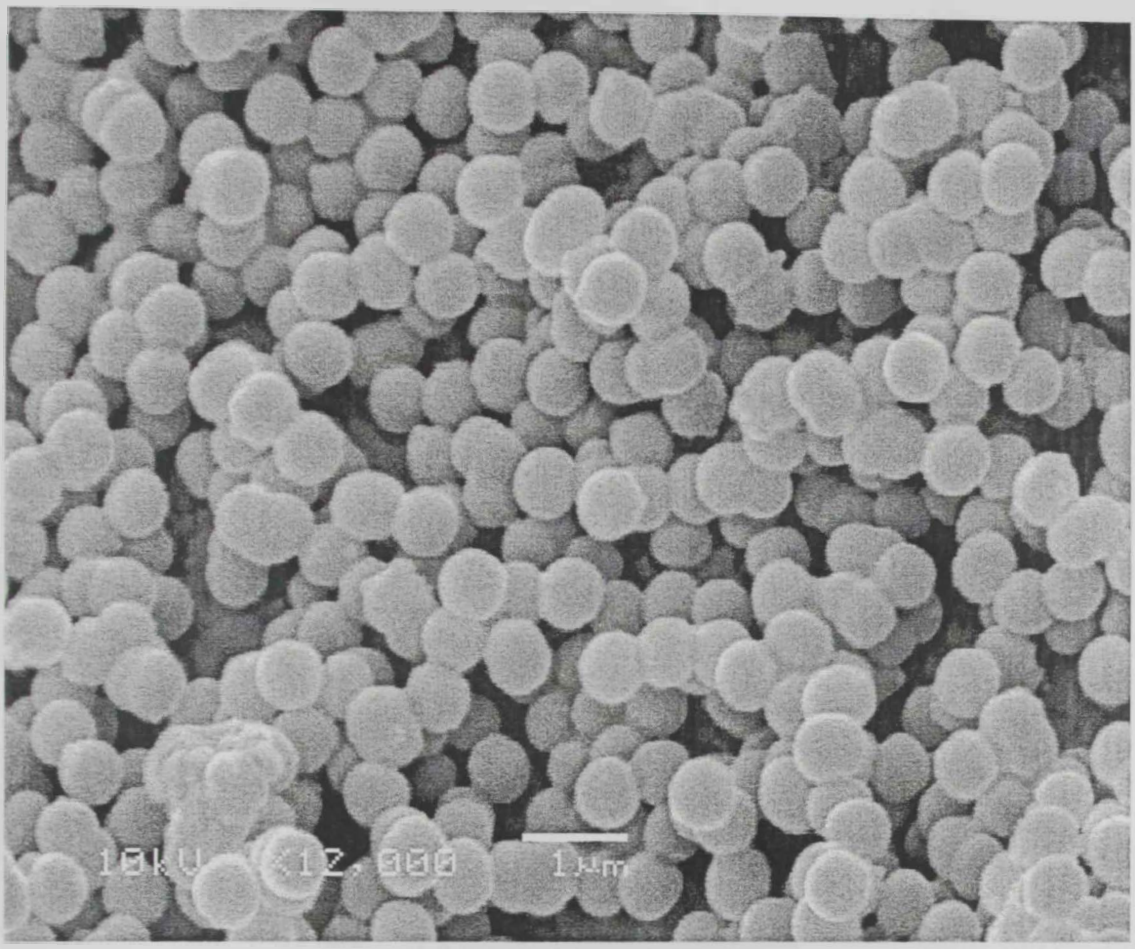

Figure 4.14 (c) Continued.

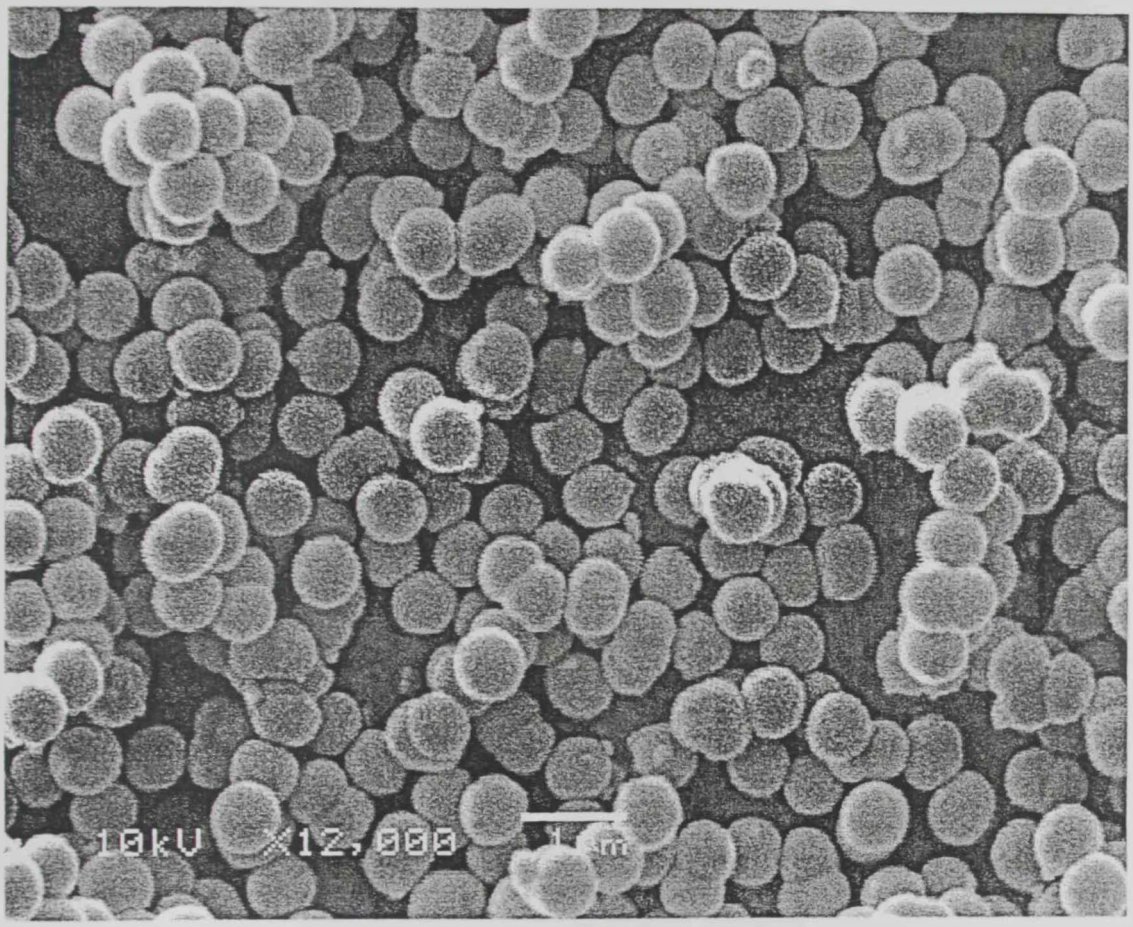

Figure 4.14 (d) Continued.

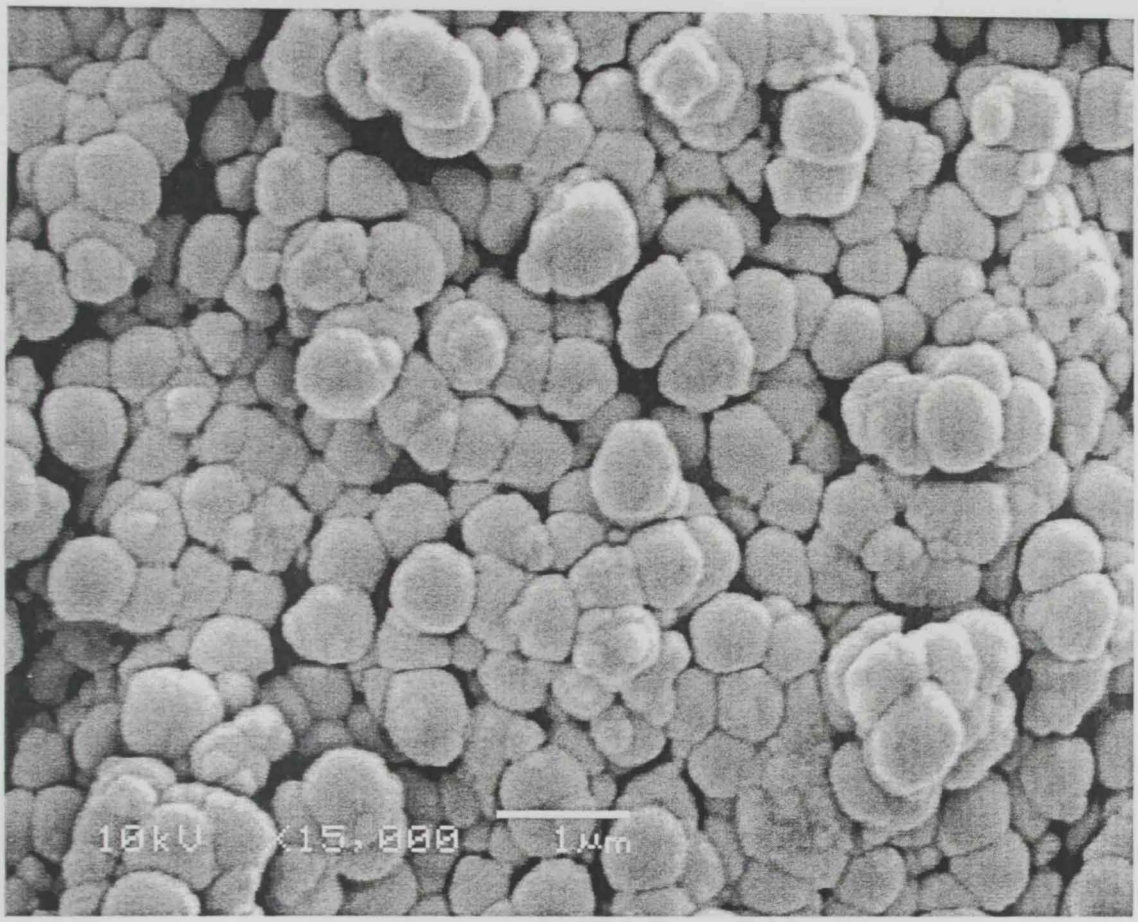

Figure 4.15 (a) Scanning electron micrographs of the calcined materials (a) 10%Alk, (b) 20%Alk (c) 10%Ing, and (d) 20%Ing.

Figure 4.15 (b) Continued.

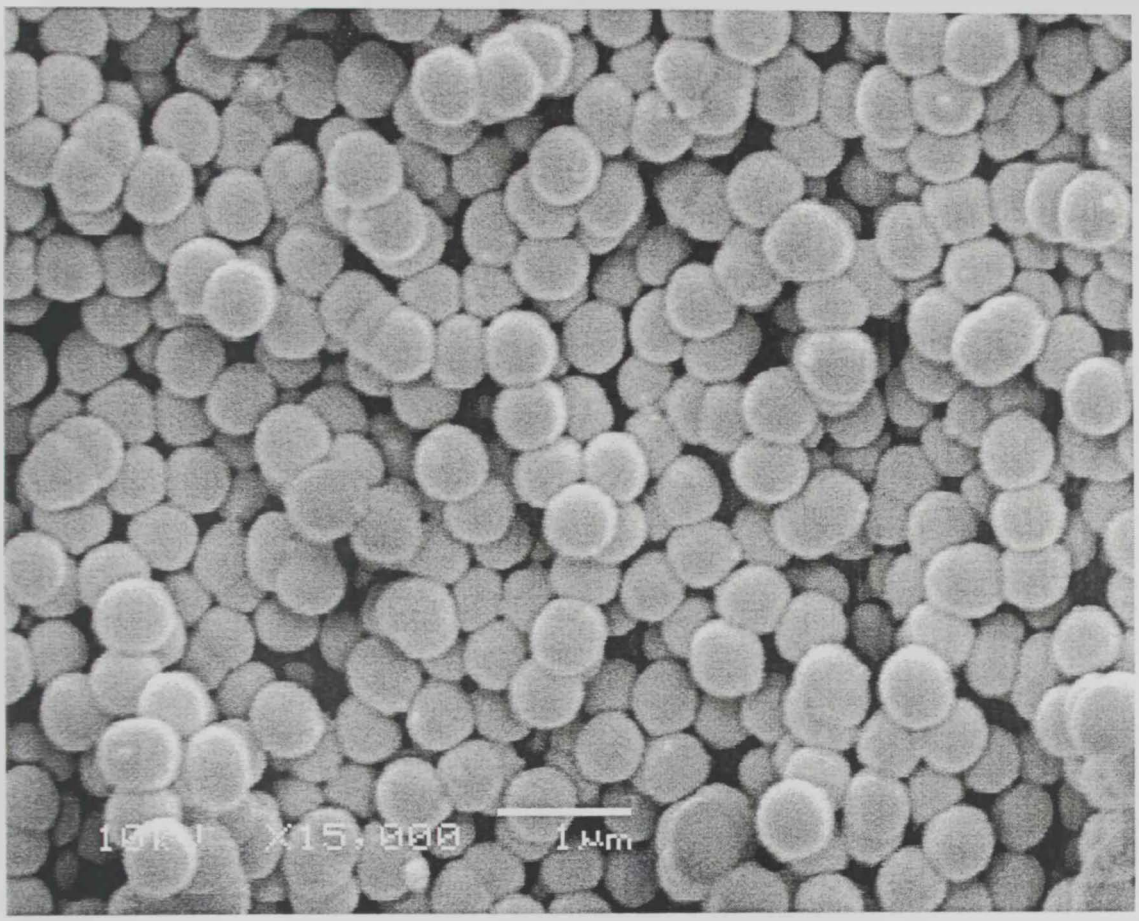

Figure 4.15 (c) Continued.

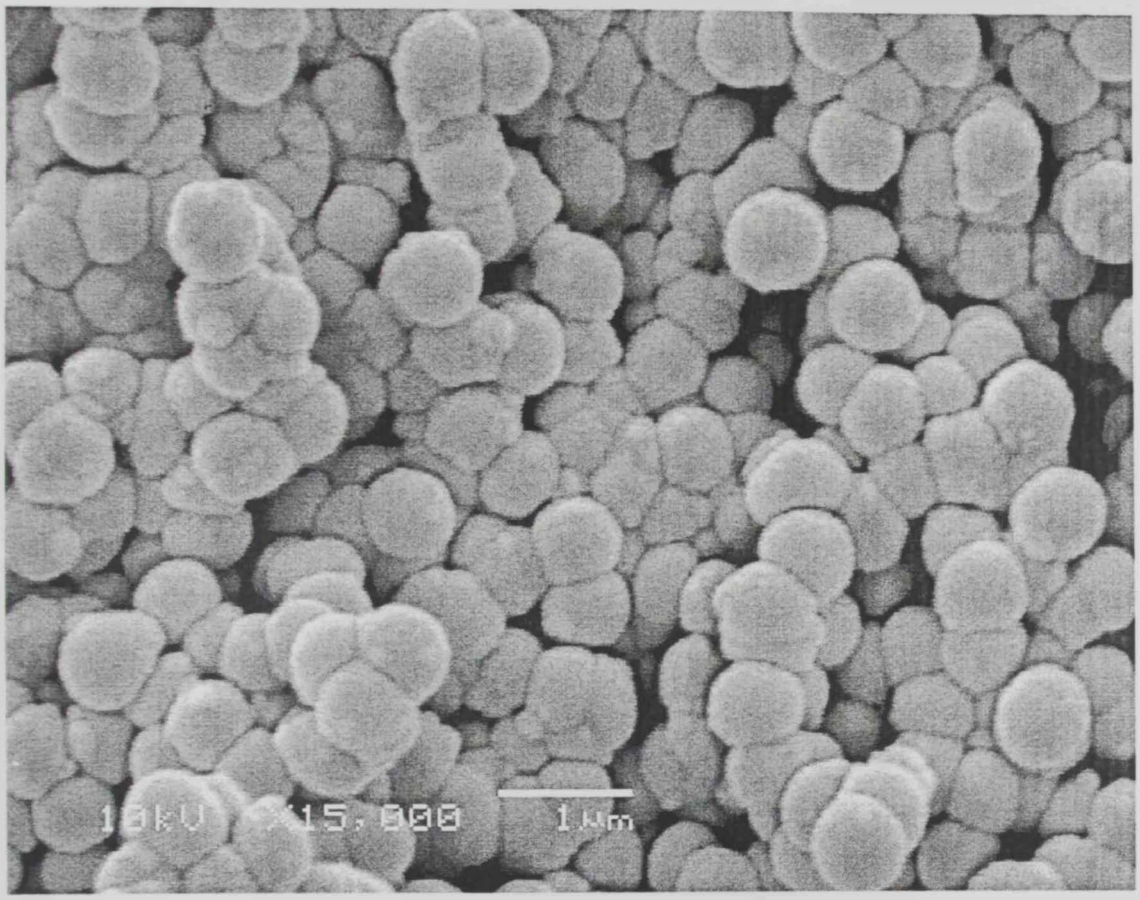

Figure 4.15 (d) Continued.

References

References:-

References of Chapter 1:-

1- L. R. Morss. *Handbook on the Physics and Chemistry of Rare Earths Elsevier Science: New York*, Vol. 18 (1994) 239-291.

2- G. Adachi and N. Imanaka, *Chem. Rev* 98 (1998) 1479-1514.

3- R. E. Kiork and D. F. Othmer, "*Cerium Cerous Compounds*" , in Encyclopedia of a Chemical Technology, 3 rd ed., Vol . 5 pp.315-337 ,Wiley, New York, 1979.

4- A. A. Bhattacharyya, G. M. Woltermann, J. S. Yoo, J. A. Karch, and W. E. Cormier, *Ind. Eng. Chem.Res* 27 (1988) 1356.

5- J. S. Yoo and J. A. Jaecker, *U. S. Patent*, 4 (1984) 469, 589.

6- R. J. Bertolacini, E. H. Hirschberg, and F. S. Modica, *U. S. Patent* 4 (1985) 497, 902.

7- D. J. Bevan, J. Kordis, *J. Inorg. Nucl. Chem* 26 (1964) 1509-1523.

8- B. Iwasaki, T. Katsura , T. *Bull, Chem . Chem . Soc* . Jpn 44 (1971) 1297.

9- O. T. Sorensen, *J. Solid State Chem* 18 (1976) 217-233.

10- M. Breysse, M. Guenin, B. Glaudel, H. Latreille, J. Veron, *J . Catal* 27 (1972) 275.

11- M. Breysse, M. Guenin, B. Glaudel , J. Veron, *J . Catal* 28 (1973) 54.

12- W. Liu, M. Flytzani-Stephanopoulos, *J . Catal* 153 (1995) 304.

13- A. Tschope , W. Liu , M. Flytzani-Stephanopoulos, J. Y. Ying, *J . Catal* 157 (1995) 42-50.

14- W. Liu, M. Flytzani-Stephanopoulos. In Enviromental Catalysis, Armor, J.N., Ed , ASC Symposium Series 552, American Chemical Society: Washington, DC, 1994, p 375.

15- A. Tschope, J. Y. Ying. In Nanophase Materials: *Synthesis- Properties-Applications*, Hadjipanayis, G. C., Siegel, R. W., Eds.; Kluwer: Dordrecht, The Netherlands, 1994 , p 781.

16- W. Liu, A. F. Sarofim, M. Flytzani-Stephanopoulos, *Appl. Catal. B*: 4 (1994) 167.

17- A. Tschope, J. Y. Ying, W. Liu, M. Flytzani-Stephanopoulos. In Materials and Processes for Environmental protection ; Voss, K.E., Quick, L. M., Gadgil, P.N. , Adkins, C. L.J. , Eds .; MRS Symposium Prceedings 344; *Materials Research Society* : Pittsburgh, 1994, p 133.

18- A. Tschope,, D. Schaadt, R. Birringer, J. Y. Ying , *Nanostr. Mater* 9 (1997) 423.

19- H. C. Yao, Y. F. Yu Yao, *J . Catal.* 86 (1984) 254.

20- A. Trovarelli, *Catal. Rev. Sci. Eng* 38 (1996) 439-520.

21- J. Campserveux and P. Gerdanian, *J. Solid State Chem* 23 (1978) 73-92.

22- R. J. Panmlener, R. N. Blumenthal and J. E. Garnier, *J. Phys. Chem. Solids* 36 (1975) 1213-1222.

23-G. Brauer and K. A. Gingerich, *J. Inorg. Nucl. Chem* 16 (1960) 87-99.

24- H. W. Chiang, R. N. Blumenthal and R. A. Fournelle, *Solid State Ionics* 66 (1993) 85-95.

25- S. P. Ray, A. S. Nowick and D. E. Cox , *J. Solid State Chem* 15 (1975) 344-351.

26- E. A. Kummerle and G. Heger, *J. Solid State Chem*. 147 (1999) 485-500.

27- D. J. M. Bevan, *J. Inorg. Nucl. Chem* 1 (1955) 49-59.

28- S. P. Ray and D. E. Cox, *J. Solid State Chem* 15(1975) 333-343.

29- M. Ricken , J. Nolting and I. Riess, *J. Solid StateChem* 54 (1984) 89-99.

30- R. B. Von Dreele , L. Eyring, A. L. Bowman and J. L. Yarnell, *Acta. Cryst. B*: (1975) 971- 974.

31- Z. C. Kang and L. Eyring, L. Aust, *J. Chem* 49 (1997) 981-996.

32- O. T. Sorensen, *In Nonstoichiometric Oxide*, Ed.., Academic Press: New York, (1981) 1-59.

33- R. G. Haire and L. Eyring. *Handbook on the Physics and Chemistry of Rare Earths Elsevier Science*: New York, Vol. 18 (1994) 413-505.

34- P. Knappe and L. Eyring, *J. Solid State Chem* 58 (1985) 312-32

35- R. L. J. Martin, *J. Chem. Soc.* Dalton (1974) 1335-1350.

36- L. Minervin, M. O. Zacate and R. W. Grime, *Solid State Ionics* 116 (1999) 339-349.

37- H. L. Tuller and A. S. Nowich, *J. Electrochem. Soc* 126 (1979) 209-217.

38- R. N. Blumenthal, P. W. Lee and R. J. Panlener, *J. Electrochem. Soc* 118 (1971) 123-129.

39- A. Trovarelli, M. Boaro, E. Rocchini, C. de Leitenburg, G. Dolcetti, *J. Alloy and Compounds* 584 (2001) 323-324.

40- E. Rocchini, M. Vicario, J. Llorca,C.deLeitenburg, G. Dolcetti, A. Trovarelli, *J. Catal* 211 (2002) 407-421.

41- A. Laachir, V. Perrichon, A. Badri, J. Lamotte, E. Catherine, J. C. Lavalley, J. El Fallah, L. Hilaire, F.Lenormand, E. Quemere, G.N. Sauvion and O. Touret, *J. Chem. Soc., Faraday Trans* 1,87 (1991) 1601.

42- L. G. Fierro, J. Soria, J. Sanz and J.M. Rojo, *J. Solid State Chem* 66 (1987) 154.

43- H. C. Yao and Y. F. Yao, *J. Catal* 86 (1984) 254.

44- M. F. L. Johnson and J. Moot, *J. Catal* 103 (1987) 502.

45- V. Perrichon, A. Laachir, G. Bergeret, R. Frety, L. Tournayan and O. Touret, *J. Chem. Soc. Faraday Trans* 90 (1994) 773.

46- S. Bernal, J. J. Calvino, G. A. Cifredo, J. M. Gatica,J. A. Perez Omil and J.M. Pintado, *J. Chem. Soc. Faraday Trans* 89 (1993) 3499.

47- S. Bernal, J. J. Calvino, J. M. Gatica, C. Lopez Cartes, and J. M. Pintadoarelli, in "Catalysis by Ceria and Related Materials" (A. Trovarelli, Ed.), *Catalysic Science Series*- Vol. 2, Chap. 4, pp. 85-168. Imperial College Press, London, 2002.

48- V. Perrichon, A. Laachir, S. Abouarnadasse, O. Touret, G.Blanchard, *Appl.Cata A: General* 129 (1995) 69-82.

49- S. Bernal, J. J. Calvino, G.A. Cifredo, J. M. Rodriguez-Izquierdo, V. Perrichon and A. Laachir, *J. Catal* 137(1992) 1.

50- S. Bernal, J. J. Calvino, G. A. Cifredo, J. M. Rodriguez-Izquierdo, A. Laachir, V. Perrichon and J. M. Herrmann, *Langmuir* 10 (1994) 717.

51- M. Pijolat, M. Prin , M. Soustelle and P. Nortier, *J. Chim. Phys* 91 (1994) 51.

52- T.B. Lindemer and X. V. Calphad, Pergamon Journals Ltd., 10 (1986) 129.

53- A. Badri, J. Lamotte, J. C. Lavalley, A. Laachir, V. Perrichon, O. Touret, G. N. Sauvion and E. Quemere, Eur, *J. Solid State Inorg, Chem* 28 (1991) 445.

54- R. S. Mikhail, R. M. Gabr and R. B. Fahim, *J. Appl. Chem* 20 (1970) 222.

55-T. Yamaguchi, N. Ikeda, H. Hattori and K. Tanabe, *J. Catal* 67 (1981).

56- J. E. Kubsh, J. S. Rieck and N. D. Spencer, *Stud. Surf. Sci. Catal* 71 (1991) 125.

57- M. Pijolat, M. Prin, M. Soustelle and O. Touret, *J. Chim. Phys* 91 (1994) 37.

58- P. D. L. Mercera, J.G. Van Ommen, E.B.M. Doesburg, A. J. Burggraaf and J. R. H. Ross, *Appl. Catal* 57(1990) 127.

59- E. K. Chang and R. N. Blumenthal, *J. Catal* 72 (1988) 330.

60- F. .M. Z. Zotin, L. Tournayan, j. Varloud, V. Perrichon and R. Frety, *Appl. Catal. A*: 98 (1993) 99.

61- K. Tarai, K. Maruya, K. Domen and T. Onishi, *J. Catal* 141 (1993) 533.

62- J. Kaspar, P. Fornasiero, in "*Catalysis by Ceria and Related Materials*" (A. Trovarelli, Ed.), Catalysic Science Series- Vol. 2, Chap. 6, pp. 217-241. Imperial College Press, London, 2002.

63- S. Matsumoto, N. Miyoshi, T. Kanazawa, M.Kimura, M. Ozawa, *Catal. Sci, Technol* 1 (1991) 335.

64- D. Terribile, A. Trovarelli, C. de Leitenburg, G. Dolcetti, *Chem. Mater* 9 (1997) 2676-2678

65- D. Terribile, J. Llorca, M. Boaro,A. Trovarelli, C. de Leitenburg, G. Dolcetti , *Chem. Commun* (1998) 1897.

66- D. Terribile, A. Trovarelli, J. Llorca, C. de Leitenburg, G. Dolcetti, *J. Catal.* 178 (1998) 299-308.

67- D. Terribile, A. Trovarelli, J. Llorca, C. de Leitenburg, G. Dolcetti, *J. Catal. Today* 43 (1998) 79.

68-T. Masui, T. Ozaki, K. Machida, G.Adachi, *J. of Alloys and Compounds* 303-304 (2000) 49-55.

69- G. N. Saavion. J. Caillod and C. Gourlaouen, *Rhone Poulenc. Eur. Pat*, 0207857, 1986; T Ohata, K. Tsuchitani and S. Kna-guchi, Nippon Shokubai Kagaku, Jpn. Pat., 8890311. 1988: N. E. Ashky and J. S. Rieck, Grace W R and Co-Conn. *US Pat.* 484727,1991.

70- R. Cracium. *Solid state Ionics* 110 (1998) 83-93.

71- R. Craciun, W.Daniell, H. Knozinger, *Applied Catalysis A:General* 230 (2002) 153-168.

72- J. Kaspar, P. Fornasiero, M. Graziani, *Catalysis Today* 50 (1999) 285-298.

73- T.Chojnaki, K. Krause, L. D. Schmidt, *J. Catal* 128 (1991) 161.

74- K. R.Krause, P. Schabes-Retchkiman, L. D. Schmidt, *J. Catal* 134 (1992) 204.

75- L. Kepinski, M. Wolcyrz, *Catal. Lett* 15 (1992) 329.

76- E. Rocchini, A. Trovarelli, J. Llorca, G. W. Graham, W .H. Weber, M .Maciejewski and A. Baiker, *J. Catal* 194 (2000) 461-478.

77- A. Trovaerlli, *J. Alloys and Comp* 584 (2001) 323-324.

78- A. Martinez-Arias, M. Fernandez-Garcia, L. N. Salamanca, R. X. Valenzuela, J.C. Conesa and J. Soia, *J. Phys. Chem. B*: 104 (2000) 4038.

79- G.Y Adachi, T. Masui, in "*Catalysis by Ceria and Related Materials*" (A. Trovarelli, Ed.), Catalysic Science series- Vol. 2, Chap. 3, pp. 51-83. Imperial College Press, London, 2002.

80- M. Lundberg, B. Skarman, F. Cesar, L. R. Wallenberg, *Microporous Mesoporous Mater* 54 (2002) 97-103.

81- Y. He, B. Yang, G. Cheng, *Mater. Letters* 57 (2003), p. 1880.

82- T. Masui, K. Fujiwara, K. Machida, G. Adachi, *Chem. Mater* 9 (1997) 2197.

83- L. A. Bruce, M. Hoang, A. E. Hughes, T. W. Turny, *Applied Catal A.* 134 (1996) 351.

84- J. G. Li, T. Ikegami, J. H. Lee, T. Mori, *Acta Mater.* 49 (2001) 419.

85- J. C. Yu, L. Zhang, J. Lin, *J. Colloid and Interface. Sci.* 260 (2003) 240.

86- D.Z.Jia, J-Q. Yu, and X-Q.Xin , " One Method for the Preparation of Nanocrystals by Solid State Reaction" *Chinese Pat. Appl. No.*, 98111231.5, 1998.

87- T. Masui, T. Ozaki, K. Machide, G. Adachi, *J. Am. Ceram* 83 (4) (2000) 964-966.

88- X. R. Ye, D. J. Jia, J. Q. Yu .X. Q. Xin, and Z. Xue, " One Step Solid- State Reaction at Ambiet Temperature-A Novel Approach to Nanocrystals'', *Adv. Mater.*, 11 (11) (1999) 941-942.

89- F. Bondioli, A. Bonamartini Corradi, C. Leonelli, and T. Manfredini, *Material Research Bulletinn* Vol. 34, Nos. 14/15 (1999) 2159-2166.

90- M. F. Wilkes, P. Hayden, and A.K. Bhattacharya, *J Catal* 219 (2003)295.

91- B. Zhu, X Liu, M. Sun, S. Ji, J. Sun, *Soild State Sci* 5 (2003) 1127.

92- R. C. Bozo, F. Gaillard, N. Guilhaume, *Appl. Catal. A Gen.* 220 (2001) 69.

93- J. Kaspar, P. Fornasiero, *J. Solid State Chem*171 (2003) 19–29.

94- C. J. Brinker, G. W. Scherer, "*Sol-Gel Science, The Physics and Chemistry of Sol-Gel Processing*". Academic Press, New York/London (1989).

95- A.C. Pierre, "*Introduction to Sol-Gel Processing*", Kluwer International Series in Sol-Gel Processing: Technology and Applications, (L.Klein, Ed.), Kluwer Academic Publishers, London (1998).

96- J. D. Wright, N. A. J. M. Sommerdijk, "*Sol-Gel Materials Chemistry and Applications*", Taylor & Francis Books Ltd, London (2001).

97- K. M. S. Khalil, *J. Catal* 178 (1998) 198.

98- K. M. S. Khalil, M. I. Zaki, *Powder Technol.* 120 (2001) 256.

99- D. Seyferth, G.H,in "*Ultrastructure Processing of Ceramics, Glass and Composites*", Edited by L.L. Hench, and D.R. Ulrich, Wiely, New-York, (1984) 265-271.

100- R. Takahashi, S. Takenaka, S. Sato, T. Sodesawa, K. Ogura and K. Nakanishi, *J. Chem. Soc. Faraday Trans* 94 (1998) 3161-3168.

101- D.Terribile, A. Trovarelli., C. de Leitenburg and G. Dolcetti, *Chem. Mater* 9 (1997) 2676-2678.

References of Chapter 2:-

1- W. Stöber, A. Fink, and E. Bohn, *J. Colloid Interface Sci* 26 (1968) 62.

2- JCPDS, International Centre for Diffraction Data, CD, 1996.

3- H. P. Klug, L.E. Alexander, X-ray Diffraction Procedure for Polycrystalline and Amorphous Materials, Wiley: New York. (1974).

4- S. Brunauer, P. Emmett and E. Teller, *J. Amer. Chem. Soc* 60 (1938) 309.

5- E. P. Barrett, L. G. Joyner, and P.P. Halenda, *J. Amer. Chem. Soc* 73 (1951) 373.

6- W. D. Harkins, G. Jura, *J. Amer. Chem. Soc* 66 (1944) 1366.

7- B. C. Lippens and J. H. de Boer, *J.Catal* 4 (1965) 319.

8- K. S. W. Sing, D. H. Everett, R. A. W. Haul, L. Moscou, R.A. Pierotti, J. Rouquerol, and T. Siemieniewska, International Union of Pure and Applied Chemistry, IUPAC, *Pure Appl.*

Chem 57 (1985) 603.

9- S. J. Gregg and K. S. W. Sing, Adsorption, Surface Area and Porosity, 2nd Ed., New York (1982).

10- P. A. Webb and C. Orr, "Analytical Method in Fine Particle Technology", micrometrics, Norcross, USA (1997).

11- F. Rouquerol, J. Rouquerol and K. Sing, Adsorption by Powders & Porous Solids, Academic Press, London (1999).

12- A. V. Kiselev and Y. A. Eltekov. World Congress on Surface Activity, Vol.II,p. 228, Butterworths, London (1957).

13- S. Lowell, J. Shields, G. Charalambous and J. Manzione, *J. Colloid Interface Sci* 86 (1982) 191.

14- S. Brunauer, L. S. Deming, W. S. Deming and E. Teller, *J. Amer. Chem. Soc* 62 (1940) 1723.

15- G. D. Halsey, *J. Chem. Phys* 16 (1948) 931.

References of Chapter 3:-

1- A. Trovarelli, *Catal Rev. Sci. Eng.* 38 (1996) 439.

2- A. Trovarelli, Ed., "*Catalysis by Ceria and Related Material*", Imperial College Press, London (2002).

3- J. Kaspar, P. Fornasiero, M. Graziani, *Catal. Today* 50 (1999) 285.

4- G. Adachi, T. Masui, in: "*Catalysis by Ceria and its Related Materials*", A. Trovarelli, Ed., Imperial College Press, London (2002), p. 51-83 and references therein.

5- J. D. Wright, N. A. J. M. Sommerdijk, *"Sol-Gel Materials Chemistry and Applications"*, Taylor & Francis Books Ltd, London (2001).

6- C. J. Brinker, G. W. Scherer, *"Sol-Gel Science, The Physics and Chemistry of Sol-Gel Processing"*. Academic Press, New York/London (1989).

7- K. M. S. Khalil, *J. Catal* 178 (1998) 198.

8- K. M. S. Khaḷil, M. I. Zaki, *Powder Technol* 120 (2001) 256.

9- R. Cracium, W. Daniell, H. Knozinger, *Appl. Catal. A: Gen* 230 (2002) 153.

10- D. Terribile, A. Trovarelli, J. Llorca, C. de Leittenburg, G. Dolcetti, *J. Catal* 178 (1998) 299.

11- R. D. Maggio, R. Campostrini, G. Guella, *Chem. Mater* 10 (1998) 3839.

12- D. M. Lyons, K. M. Ryan, M. A. Morris, *J. Mater. Chem* 12 (2002) 1207.

13- C. Binet, M. Daturi, J. C. Lavelly, *Catalysis Today* 50 (1999) 207

14- J. Goldsmith and S. Ross, *Spectrochim. Acta A* 23 (1967) 1909.

15- International Union of Pure and Applied Chemistry, IUPAC, *Pure Appl. Chem* 57 (1985) 603.

16- F. Rouquerol, J. Rouquerol, K. Sing, *"Adsorption by Powders and Porous Solids"*, Academic Press, London (1999) 440.

17- W. Stober, A. Fink, and E.Bohn, *J. Colloid Interface Sci* 26 (1968) 62.

References of Chapter 4:-

1- H. Vidal, J. Kašpar, M. Pijolat, G. Colon, S. Bernal, A. Cordón, V. Perrichon , F. Fally, *Appl Catal B: Environmental* 27 (2000) 49.

2- G. Sedmak, S. Hocevar, and J. Levec, *J Catal.* 222 (2004) 87.

3- A. Trovarelli, M. Boaro, E. Rocchini, C. de Leitenburg, G. Dolcetti, *J. Alloy and Compounds* 584 (2001) 323-324

4- J. Kaspar, P. Fornasiero, M. Graziani, *Catal. Today* 50 (1999) 285.

5- J. Kaspar, P. Fornasiero, in "*Catalysis by Ceria and Related Materials*" (A. Trovarelli, Ed.), Catalysic Science series- Vol. 2, Chap. 6, pp. 217-241. Imperial College Press, London, 2002.

6- G. N, Sauvion, J. Caillod, and C. Gourlaouen, *U.S. Patent* 4,940,685 (1990).

7- L. Bonneau, T. Chopin, O. Touret, *U.S. Patent* 5,529,969 (1996).

8- K. M. S. Khalil, A.A. Elsamahy, and M.S. Elanany, *J. Colloid Interface Sci* 249 (2002) 359.

9- D. C. M. Dutoit, , M. Schneider, and A. Baiker, *J. Catal* 153 (1995) 165.

10- C. J. Brinker, G. W. Scherer, "*Sol-Gel Science, The Physics and Chemistry of Sol-Gel Processing*". Academic Press, New York/London, 1989.

11- International Union of Pure and Applied Chemistry, IUPAC, *Pure Appl. Chem* 57 (1985) 603.

12- F. Rouquerol, J. Rouquerol, K. Sing, "*Adsorption by Powders and Porous Solids*", Academic Press, London, 1999, p. 440.

جامعة الامارات العربية المتحدة
عمادة الدراسات العليا
برنامج ماجستير علوم وهندسة المواد

تحضير وتوصيف مواد مثبتة حراريا من السيريا وأخرى تحتوي عليها

رسالة مقدمة من الطالبة
لينا علي راشد الكعبي

الى جامعة الامارات العربة المتحدة
استكمالا لمتطلبات الحصول على درجة الماجستير في علوم وهندسة المواد

مشرفي الرسالة

د.كمال خليل
الأستاذ المساعد
قسم الكيمياء
كلية العلوم
جامعة الامارات العربية المتحدة

د. براين ميرفي
الأستاذ المساعد
قسم الكيمياء
كلية العلوم
جامعة الامارات العربية المتحدة

2004

Shrieen
Digitally signed by Shrieen
DN: cn=Shrieen, o=UAE University, ou=UAEU Libraries Deanship, email=shrieen@uaeu.ac.ae, c=US
Date: 2016.09.08 09:44:46 +02'00'